Twin particles and their love-hate relationship

An experimental study on shape-dependent particle pair interactions in confined Stokes flow

by

C. R. Leliveld BSc

to obtain the degree of Master of Science
at the Delft University of Technology,
to be defended publicly on Thursday January 14, 2021 at 11:00 AM.

Student number:	4239792	
Project duration:	March 5, 2020 – January 14, 2021	
Thesis committee:	dr. ir. H. B. Eral	TU Delft, responsible supervisor
	N. Nagalingam MSc	TU Delft, daily supervisor
	R. N. Georgiev MSc	TU Delft, daily supervisor
	prof. dr. ir. J. T. Padding	TU Delft, 2nd examiner
	prof. dr. ir. C. R. Kleijn	TU Delft, 3rd examiner

This thesis is confidential and cannot be made public until January 14, 2021.

TU Delft

Abstract

This thesis describes a study into pairwise particle interactions within a Hele-Shaw geometry, using stop-flow lithography. By exposing a photoreactive mixture to a strong UV-pulse, a hydrogel is formed. The shape of this hydrogel is controlled by masking part of the light beam. This process takes place while the Hele-Shaw channel is placed on the stage of a microscope, which allows these hydrogel particles to be viewed and tracked.

Improvements were made to increase the accuracy and precision of the experimental set-up. Notably, the initially present mismatch of intra-pair particle thickness was greatly reduced by changing the method of particle pair production.

By tracking these pairs of particles, information is obtained regarding their motions and velocity relative to one another. Experiments were performed for a selection of particle shapes and compared to numerical simulations of identical geometries. Simulations predicted that attractive and repulsive velocities should be noticed depending on the separation distance and shape of the particles.

Qualitatively, the experiments agree to a certain extent with the simulations. It was demonstrated that the pairwise interactions are indeed dependent on their shape. Furthermore, the magnitude of these interactions qualitatively matched with the experimental data.

Quantitatively, the experimental data did not agree with the simulations, but strong evidence was presented to indicate that the UV-light hitting the sample was not uniformly distributed. This results in a discrepancy in particle thickness between the pair, which skews the experimental data.

Novel insights were gained on the applicability of the current literature model on hydrogel particle propagation. In contrast to the current model, it was experimentally demonstrated that the shape and (in-plane) size of the particle affects its thickness.

Acknowledgements

This MSc thesis is the product of eight months of work within the Process & Energy group at the faculty of maritime, mechanical and materials engineering. The appearance of the COVID-19 virus during this time resulted in a very irregular and uncertain working environment, and I'd like to thank all the TU Delft laboratory staff and safety personnel for allowing me to carry on my laboratory work despite these odd times.

I'd like to thank my responsible supervisor Burak Eral for giving me this very interesting project, and the necessary resources to complete it. Special thanks to Johan Padding, who always managed to ask the right questions during our two-weekly meetings. I'd also like to thank Nagaraj Nagalingam for training and educating me during this entire process. Rumen Georgiev, I'll miss our lively discussions and thank you for putting up with my incessant stream of questions.

Last but definitely not least, I'd like to thank Ilse den Dekker, for motivating me throughout this entire project, and being an inspiration to me on more than one occasion.

C. R. Leliveld
Delft, January 2021

Contents

List of Figures

List of Tables

1 Introduction

In 1898, Henry Selby Hele-Shaw published his findings on hydrodynamic interactions within thin sheets of water. He showed that under the right conditions, these sheets of water behave like an ideal ”frictionless fluid” [11]. The ”frictionless” fluid flow would later turn out to be the now well-known Stokes flow. Hele-Shaw, publishing his findings for the Institution of Naval Architects, expected his work to have an application in ship-bows and pipe-flow. Today, the term *Hele-Shaw flow* commemorates his findings by describing an adequately thin geometry for which Stokes flow holds. Apart from ship-bows and pipe-flow, Hele-Shaw flow has found many applications in modern research, amongst which is the relatively recent area of stop-flow lithography experiments (SFL).

Making use of stop-flow lithography, this thesis will report on an investigation into hydrodynamic interactions between a pair of particles within a suitable Hele-Shaw geometry. Uspal et al. [23, 24], Toscano [22] and Georgiev et al. [10] investigated the hydrodynamic interactions of single particles for such a geometry, and hinted towards interactions between a pair of particles. These interactions are supposed to be dependent on the shape and symmetry of the particles, as shown by simulations by R. N. Georgiev [9].

As such, this thesis aims to experimentally prove both the existence of these interactions, and their dependency on shape. We will produce pairs of particles on the micro-scale, within translucent silicone channels. The translucency of these channels allows us to observe and track these particles with a microscope. By capturing their trajectories, we can then observe any interactions between the pair.

Since the experiments are carried out on the micro-scale, even small inconsistencies or flaws have the potential to significantly impact experimental measurements. Therefore, prior to carrying out our experiments, a suitably precise and accurate set-up will have to be created. Identifying these small effects and providing a suitable solution or explanation will be the first order of business, and a major goal of this thesis.

Succeeding in creating the set-up and consequently carrying out the proposed experiments would give valuable insights into the hydrodynamic behaviour of these particles. In the long run, being able to predict the motions of such particles could lead to valuable separation systems based on flow-manipulation. Similarly, one could speed up crystallisation rates by organising the particles, which was the intended purpose of Uspal’s article [23].

The thesis starts with the theory governing flow profiles within our Hele-Shaw channel, followed by a model of particle motion and an explanation of the previously mentioned simulations. The experimental set-up is then described, including the way in which particles are formed. The results and discussion chapter is divided into three parts: a discussion on the improvements made to the set-up, a section identifying the remaining flaws in the set-up, and the results of the experiments on pairwise interactions. Afterwards, the discussion is summarised and recommendations are given. The appendix can be consulted for supplementary information on protocols, and lists the raw data of key figures within the thesis.

2

Theory

The underlying theoretical models for particle motion in Stokes flow will be discussed in this chapter. The chapter starts with a description of the fluid dynamics within the channel and around particles in section 2.1. Next, a model describing particle motion for a defined fluid flow is explained in section 2.2. In particular, the coupling of degrees of freedom for these particles is detailed. Using this theory as a framework, simulations on particle-pair interactions will be discussed in section 2.3.1

2.1. Fluid dynamics

The Navier-Stokes (NSE) and continuity equations are key starting points to describe the flow within a channel. The continuity equation basically describes the conservation of mass for an arbitrary geometry. Using density as our mass variable, the mass balance can be expressed as:

$$\frac{\partial \rho}{\partial t} + \nabla \cdot (\rho \mathbf{v}) = -\nabla \cdot \mathbf{f} + B_v \tag{2.1}$$

where ρ is the density, $\nabla \cdot \rho \mathbf{v}$ the convective term with $\mathbf{v}$ being the velocity vector, $\nabla \cdot \mathbf{f}$ the diffusive term and B_v an arbitrary source or sink of mass.

By definition there is no diffusive term for mass ($\nabla \cdot \mathbf{f} = 0$) [5] and we will not consider any sources or sinks ($B_v = 0$). Thus, the conservation equation reduces to the well-known *continuity equation*:

$$\frac{\partial \rho}{\partial t} + \nabla \cdot (\rho \mathbf{v}) = 0 \tag{2.2}$$

For incompressible fluids, this will reduce even further, yielding:

$$\nabla \cdot \mathbf{v} = 0 \qquad \text{or for cartesian coordinates:} \qquad \frac{\partial v_x}{\partial x} + \frac{\partial v_y}{\partial y} + \frac{\partial v_z}{\partial z} = 0 \tag{2.3}$$

The Navier-Stokes equation results from a momentum balance for an arbitrary geometry. For incompressible fluids, this can be expressed as:

$$\rho \left(\frac{\partial \mathbf{v}}{\partial t} + (\mathbf{v} \cdot \nabla) \mathbf{v} \right) = -\nabla p + \mu \nabla^2 \mathbf{v} + \rho \mathbf{g} \tag{2.4}$$

where p is the pressure, μ is the dynamic viscosity and $\mathbf{g}$ is the gravitational constant in vector notation.

Apart from the NSE and *continuity equation*, it also important to determine whether we are dealing with laminar or turbulent flow in the channel. Given the small size of the channel, and the fact that a low pressure will be applied to create the flow, we will assume that laminar flow is induced. The Reynolds number is a key indicator of whether flow is laminar or turbulent, and is defined as:

$$Re \equiv \frac{\rho v l_c}{\mu} \tag{2.5}$$

with l_c being the characteristic length of the channel. The Reynolds number measures the dominance of inertial forces relative to viscous forces present in the system. In the experimental phase, low Reynolds numbers ($Re < 10^{-4}$) will guarantee that the flow is indeed laminar, and that any assumptions made based on this are valid. For Stokes' flow or creeping flow, these assumptions are instantaneity, and because of it, the flow is time reversible [5]. Stokes' flow is independent of time, and therefore only relies on boundary conditions to be solved. Furthermore, flipping the direction of fluid flow will cause the fluid to retrace it steps.

2.1.1. Channel flow characteristics: height profile

Further analysis of the governing fluid dynamics require knowledge of the channel and particle geometry. Figure 2.1 shows a rectangular channel with length L, width W and height H. It is important to note that the figure is not properly scaled: the channel is significantly wider than it is high ($H \ll W$). The length of the channel is the largest dimension, and can be considered infinite for now.

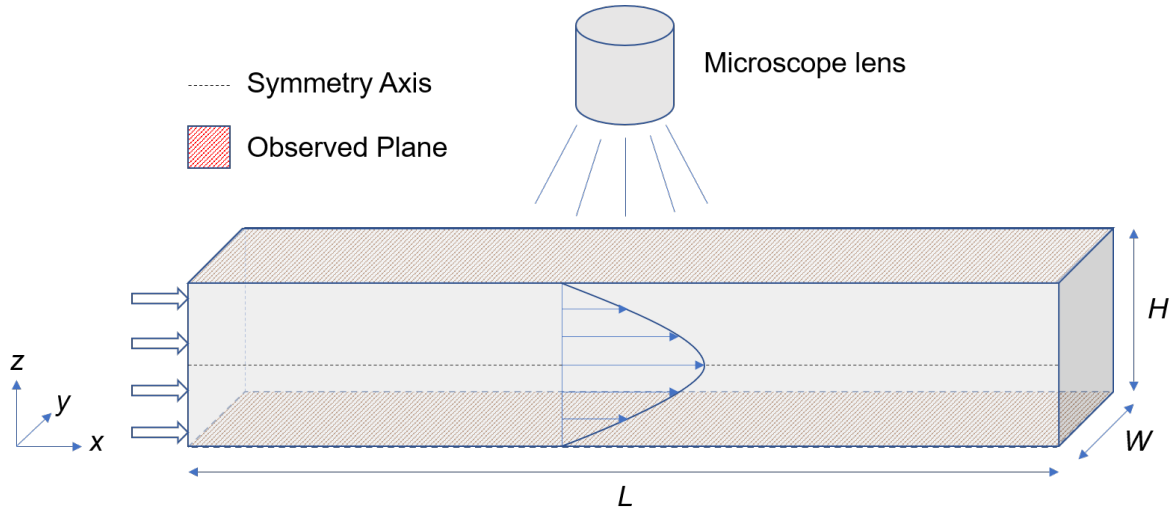

Figure 2.1: A rectangular channel with length L, width W and height H. The channel is not realistically scaled, since it is significantly wider than it is high ($H \ll W$). A uniform inlet velocity is shown at the beginning (left) of the channel, which transforms into *plane Poiseuille flow* after an arbitrary entrance length. To maintain a sense of direction, the microscope lens and the plane it observes are highlighted.

A 1D-solution can be found for the steady, fully developed flow-profile along the height of the channel (z-dimension) and far from the side walls. Starting point for this uni-directional flow problem is the NSE, eq. (2.4), for the x-direction:

$$\rho\left(\frac{\partial v_x}{\partial t} + v_x\frac{\partial v_x}{\partial x} + v_y\frac{\partial v_x}{\partial y} + v_z\frac{\partial v_x}{\partial z}\right) = -\frac{\mathrm{d}p}{\mathrm{d}x} + \mu\left(\frac{\partial^2 v_x}{\partial x^2} + \frac{\partial^2 v_x}{\partial y^2} + \frac{\partial^2 v_x}{\partial z^2}\right) \tag{2.6}$$

The time-derivative and convective term in the x-direction can be set to zero, since the flow is well-developed and at steady state for the channel portion of interest. The approximation of *nearly uni-directional flow* yields that the velocity in the y and z direction is also zero, setting the entire left hand side (LHS) of the equation to zero. Developed flow also requires that the velocity cannot change along the x-axis (for any streamline). The pressure can be considered a function of x and y only, due to the large differences in dimensions ($H \ll W \ll L$). Another consequence of the large dimensional differences is the fact that the diffusive terms in the x and y-direction are relatively small when compared to the z-direction, and can therefore be cancelled out.

Combining all these simplifications, equation (2.6) is reduced to:

$$0 = -\frac{\mathrm{d}p}{\mathrm{d}x} + \mu\frac{\mathrm{d}^2 v_x}{\mathrm{d}z^2} \tag{2.7}$$

No-slip boundary conditions are then imposed at the top and bottom walls of the channel, according to:

$$v_x(0) = 0 \qquad \text{and} \qquad v_x(H) = 0 \tag{2.8}$$

Combining equations (2.7) and (2.8) and solving for v_z yields a *plane Poiseuille flow*:

$$v_x(z) = \frac{1}{2\mu}\frac{\mathrm{d}p}{\mathrm{d}x}\left(z^2 - zH\right) \tag{2.9}$$

Alternatively, the maximum velocity v_{max} can be used to express the velocity field. The maximum velocity is attained at the axis of symmetry at $z = \frac{H}{2}$, where $\frac{\mathrm{d}v_x}{\mathrm{d}z} = 0$. This alternative form reads:

$$v_x(z) = \frac{4v_{max}}{H^2}\left(zH - z^2\right) \qquad \text{with} \qquad v_{max} = v_x\left(\frac{H}{2}\right) = -\frac{1}{8\mu}\frac{\mathrm{d}p}{\mathrm{d}x}H^2 \tag{2.10}$$

The 2D-solution of the *plane Poiseuille flow* has been illustrated in the previously shown figure 2.1

2.1.2. Channel flow characteristics: width profile

It must be noted, that the previously derived *Poiseuille flow* is only valid under strict conditions: the Reynolds number must be sufficiently low ($Re < 10^{-3}$) to justify the simplification of the NSE, and it only holds for flow far away from the side (vertical) walls and far away from any particles.

Nevertheless, this solution can be used in a more rigorous approach when considering v_{max} to be the local maximum velocity, dependent on x and y. Equation (2.10) then describes the 3D velocity field, adjusted for z, as:

$$\mathbf{v}(x,y,z) = \mathbf{v_{max}}(x,y)\frac{4(zH - z^2)}{H^2} \tag{2.11}$$

Substitution of this result into the general equation (2.7), and separating the $\frac{\partial^2}{\partial z^2}$ term from ∇^2 yields:

$$0 = -\nabla p + \frac{4\mu(zH - z^2)}{H^2}\nabla_{2D}^2\mathbf{v_{max}}(x,y) - \mathbf{v_{max}}(x,y)\left(\frac{8\mu}{H^2}\right) \tag{2.12}$$

with $\nabla_{2D}^2 = \left(\frac{\partial^2}{\partial x^2} + \frac{\partial^2}{\partial y^2}\right)$. Next, we define the height-averaged velocity $\mathbf{u}(x,y)$ by integrating equation (2.9) over the height:

$$\mathbf{u}(x,y) = \frac{1}{2\mu}\nabla p\frac{1}{H}\int_0^H z^2 - zH\,\mathrm{d}z = -\frac{1}{12\mu}\nabla pH^2 = \frac{2}{3}\mathbf{v_{max}}(x,y) \tag{2.13}$$

By height-averaging the entire equation (2.12) and substitution of equation (2.13) we obtain:

$$\mathbf{0} = -\nabla p + \mu\nabla_{2D}^2\mathbf{u}(x,y) - \left(\frac{12\mu}{H^2}\right)\mathbf{u}(x,y) \tag{2.14}$$

The derived result is the *Brinkman Equation* in two-dimensional form [4]. As shown in the previous derivation, the *Brinkman Equation* combines the NSE with an additional term that is linearly dependent on the velocity $(12\mu/H^2)\mathbf{u}(x,y)$. This term represents the resistance (force per unit volume) on the fluid due to any form of confinement, which will be particles or fibers in our case, and has the form of *Darcy's Law* [5]. A visual illustration of the *Brinkman* flow can be seen in figure 2.2a.

2.1.3. Channel flow characteristics: gap flow

Particles are strongly confined along the height of the channel. As such, a relatively small gap exists between either the channel floor or ceiling and the particle. This gap is characterised by the gap height h. The geometry is shown in figure 2.2b, along with the so-called *Couette-Poiseuille* flow. To derive the *Couette-Poiseuille* flow profile, we start with the lubrication approximation:

$$\frac{\partial^2 v_x}{\partial z^2} = \frac{1}{\mu}\frac{\mathrm{d}p}{\mathrm{d}x} \tag{2.15}$$

The no-slip boundary condition can be applied to both the channel wall ($z = 0$) and the particle boundary ($z = h$) according to:

$$v_x(0) = 0 \qquad \text{and} \qquad v_x(h) = U \tag{2.16}$$

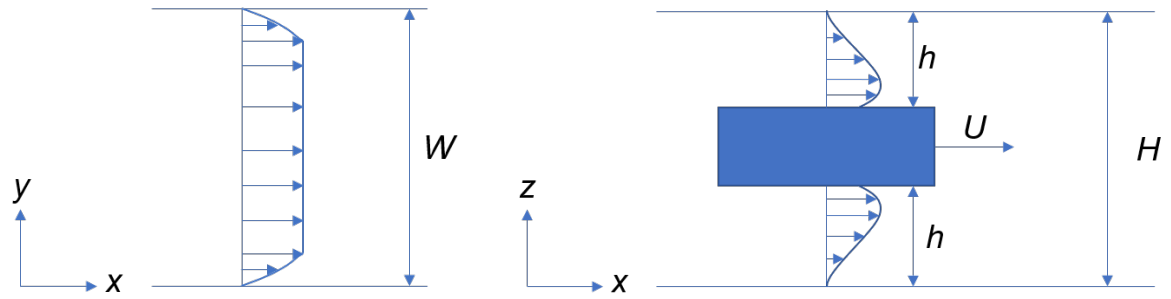

(a) *Brinkman* flow along the channel width (b) *Couette-Poiseuille* flow in the particle gap

Figure 2.2: (a) *Brinkman* flow along the channel width W, according to equation (2.14). (b) *Couette-Poiseuille* flow in the gaps between the particle and lower and upper walls, with the gap height given by h. The upper and lower gaps have identical but mirrored profiles.

with U being the particle velocity. Integrating equation (2.15) twice along z and substituting the boundary conditions (2.16) yields the *Couette-Poiseuille* flow:

$$v_x(z) = \frac{z(z-h)}{2\mu}\frac{\mathrm{d}p}{\mathrm{d}x} + \frac{u}{h}z \tag{2.17}$$

For the lubrication approximation and therefore equation (2.17) to be valid , the following conditions apply:

$$(1) \quad \frac{L_z}{L_x} \ll 1 \qquad \text{and} \qquad (2) \quad Re\,\frac{L_z}{L_x} \ll 1 \tag{2.18}$$

where L_z and L_x are the characteristic length-scales for the z-direction (height) and x-direction (length). Since particles are highly confined, h is generally very small: $h = \mathcal{O}(10)$ µm. Meanwhile, the length of the particles we will observe is generally an order of magnitude larger than the gap height, which satisfies condition (1). Typical Reynolds numbers proved to be on the order of $Re \sim 10^{-4}$ during experiments. Combining this with the previously mentioned geometric condition, satisfies condition (2).

Flow profiles along the height and width of the channel, as well as for the gaps between the particles and channel walls have been derived in this section. A literature study reveals that these derivations and approximations are widely employed in current literature on similar geometries and experiments [8, 10, 19, 20, 24], which further bolsters the reasoning behind these approximations.

2.2. Particle Motions

Now that the fluid flow in the channel is defined, it is time to relate those flows to the motion of particles. We will start by identifying some key mathematical concepts related to the particle motion. Afterwards we will relate these concepts to actual particle behaviour as found in literature.

2.2.1. Resistance Tensor

The fluid-induced motion of any particle can be related to the forces acting upon that particle. Those forces are the result of resistances of the particle on the fluid motion. In 1963, Brenner started a series of articles that mathematically describe the motion of arbitrary particles in Stokes' flow [2, 3]. One of the major conclusions from these articles was the existence of a resistance tensor $\mathbf{K}$, which is defined solely by the geometry of the particle [2]. We begin the analysis by defining the force acting upon an arbitrary particle:

$$\mathbf{F} = \iint_{\mathbf{S_P}} \mathrm{d}\mathbf{S} \cdot \mathbf{P} \tag{2.19}$$

where $\mathbf{F}$ is the force vector, $\mathbf{S_p}$ denotes the particle surface, $\mathrm{d}\mathbf{S}$ is an element of that surface area and $\mathbf{P}$ is the stress tensor. By equating any two translational fluid motions to one another, Brenner shows

that the force acting upon a particle has a linear relationship to the fluid velocity at the particle boundary $\mathbf{U}$:

$$\mathbf{F} = -\mu \mathbf{K} \cdot \mathbf{U} \tag{2.20}$$

where μ is the fluid viscosity. This equation signifies that the force a particle experiences - and therefore its motion - is determined by the resistance of the particle $\mathbf{K}$, on the fluid velocity $\mathbf{U}$. The resistance tensor is an inherent property of the particle itself, and is not influenced by the fluid [2]. It is defined as follows:

$$\mathbf{K} = \begin{pmatrix} K_{11} & K_{12} & K_{13} \\ K_{21} & K_{22} & K_{23} \\ K_{31} & K_{32} & K_{33} \end{pmatrix} \tag{2.21}$$

for which 1, 2 and 3 signify the coordinate system of choice. The different elements of the resistance tensor can be interpreted as the coupling between different directions for a given orientation of the particle: depending on the geometry of the particle, a force in one direction can have a resulting motion in a different direction. For a perfectly symmetrical body in all directions the resistance tensor will become a diagonal matrix: a force in one direction will only influence the velocity in that same direction.

The only example of such a particle would be a sphere: symmetry dictates that the resistance tensor becomes a diagonal matrix. On top of that, the resistance is equal for all directions and given by Stokes law $K_{11} = K_{22} = K_{33} = 6\pi D$, with D being the sphere diameter. Combining this with equation (2.20) gives us a familiar result for a sphere in Stokes' flow:

$$\mathbf{F} = -\mu \begin{pmatrix} 6\pi D & 0 & 0 \\ 0 & 6\pi D & 0 \\ 0 & 0 & 6\pi D \end{pmatrix} \cdot \mathbf{U} = -6\pi\mu D \mathbf{U} \tag{2.22}$$

The diagonal resistance matrix signifies that the velocity of the spherical particle is parallel to the force incurred: the zero elements signify that a velocity in a certain direction indeed cannot lead to a force in another direction.

2.2.2. Rotational tensor and coupling tensor

Similar to the resistance tensor described in the previous subsection, a rotational tensor $\mathbf{T}$ exists that couples different rotational forces. It is important to note, that both the resistance and the rotational tensor are symmetric in nature: any action will result in an equal and opposing reaction.

The coupling tensor $\mathbf{C}$ describes how a translational motion might impact the rotation of the particle, or vice versa, how torque can lead to translation. In contrast to the earlier two tensors, the coupling tensor is not inherently symmetric, due to a dependence on the point of origin chosen for the coordinate system. Nevertheless, a point exists for every geometry at which it becomes symmetric, called the *centre of hydrodynamic reaction* [3]. Including the coupling tensor in addition to the other two, is important for more complex shapes; An intuitive example would be a propeller-like particle, which will start rotating upon a purely translational fluid motion.

2.2.3. Resistance tensors applied to single particle behaviour

It is important to note that not all motions or dimensions are relevant for this work. In fact, both in literature and in this work, there is often only an interest in a small number of dimensions. When dealing with such a system, one can combine the previously mentioned tensors into a single resistance tensor, to keep the mathematical expressions clean and elegant. Therefore, from this point onwards, any mention of a resistance tensor will not necessarily be the translational resistance tensor as outlined by Brenner. Instead, it will be a tensor relating particle motions - be it rotational or translational - to the fluid velocity, and how they affect each other.

Georgiev et al. [10] performed experiments in very similar geometries and investigated trajectories of single particles, as shown in figure 2.3. Specifically, rotations of asymmetrical particles such as dimers and tripods were studied within a Hele-Shaw channel. For these experiments, the particles were tracked by a microscope and the motions of interest were in-plane translation and rotation. As such, they defined the force and torque experienced by the particle as follows:

$$\begin{pmatrix} F_x \\ F_y \\ T_z \end{pmatrix} = -\mu \mathbf{R_p} \cdot \begin{pmatrix} \dot{x} \\ \dot{y} \\ \dot{\theta} \end{pmatrix} \quad \text{with} \quad \mathbf{R_p} \sim \begin{pmatrix} l_{xx} & l_{xy} & l_{x\theta}^2 \\ l_{yx} & l_{yy} & l_{y\theta}^2 \\ l_{\theta x}^2 & l_{\theta y}^2 & l_{\theta\theta}^3 \end{pmatrix} \tag{2.23}$$

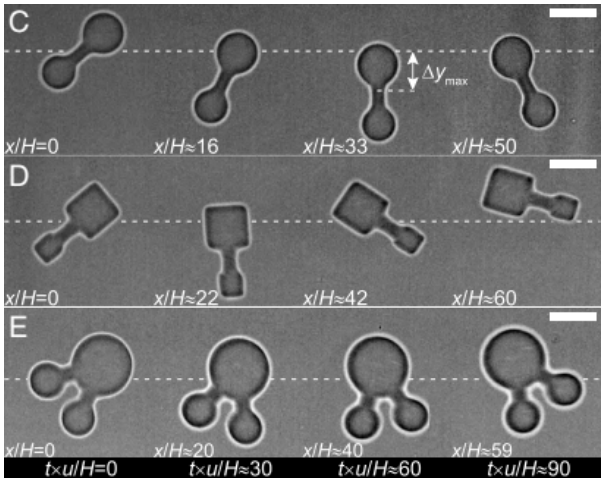

Figure 2.3: Shows the rotation of single particles as studied by Georgiev et al. [10]. The resistance tensor for such a system would only need to describe the in-plane translation and rotation. Scale bars, 50 µm.

We can clearly see from the equation that the resistance tensor $\mathbf{R_p}$ provides all necessary couplings to adequately describe the movement as shown in figure 2.3. For single particles, we will always obtain a second rank resistance tensor, which can be represented by a square matrix of size $m \times m$, where m represents the number of degrees of freedom that are of interest.

2.2.4. Resistance tensors applied to multi-particle systems

Since we are primarily interested in pairs of particles, it is important to extend this theorem so that it indeed applies for a multi-particle system. By raising the rank of each tensor element, Brenner [3] shows that the multi-particle equations can be represented similarly to the single-particle system:

$$(\mathbf{F}) = \begin{pmatrix} (\mathbf{F_1}) \\ (\mathbf{F_2}) \\ \vdots \\ (\mathbf{F_n}) \end{pmatrix} \quad \text{and} \quad (\mathbf{K}) = \begin{pmatrix} (\mathbf{K_{11}}) & (\mathbf{K_{12}}) & \cdots & (\mathbf{K_{1n}}) \\ (\mathbf{K_{21}}) & (\mathbf{K_{22}}) & \cdots & (\mathbf{K_{2n}}) \\ \vdots & \vdots & & \vdots \\ (\mathbf{K_{n1}}) & (\mathbf{K_{n2}}) & \cdots & (\mathbf{K_{nn}}) \end{pmatrix} \tag{2.24}$$

for which $(\mathbf{F_i})$ is a column vector containing the forces acting upon the i^{th} particle, and $(\mathbf{K_{ij}})$ represents the translational resistance tensor for particle i, affected by particle j. In other words, the diagonal is the resistance of each single particle with respect to the fluid flow, while the off-diagonal elements represent how one particle affects another particle. As with the single particle system, similar tensors exists that describe the rotational resistance $(\mathbf{T})$, and the coupling of these two $(\mathbf{C})$. The multi-particle expressions given above can be combined to resemble equation (2.20):

$$\boldsymbol{\mathcal{F}} = -\mu(\boldsymbol{\mathcal{R}})(\boldsymbol{\mathcal{U}}) \tag{2.25}$$

in which $\boldsymbol{\mathcal{F}}$ is the *force-torque matrix*, $\boldsymbol{\mathcal{U}}$ is the *velocity-spin matrix* and $\boldsymbol{\mathcal{R}}$ is the *grand resistance tensor*. Similarly to what was mentioned before, the grand resistance tensor incorporates all resistances experienced by the particle pair, and is not exclusively a translational resistance tensor. The grand resistance tensor has a size $i \times i$, where i is the number of particles described by the system. Each element of this tensor is a size $m \times m$ where m is the number of dimensions that are relevant.

2.3. Simulations on multi-particle systems

As mentioned before, the (grand) resistance tensor is determined solely by the geometry of the particle or system of particles. Once it has been determined, one can calculate the force acting upon a particle and thus predict its motion. Simulations are a good way of determining this grand resistance tensor, since you can create the perfect system: any experimental set-up will always have its inherent flaws and uncertainties.

In an internal document (unpublished work at the time of writing), R. N. Georgiev carries out simulations for a wide range of geometries on pairs of particles [9]. These simulations define an identical

Hele-Shaw geometry as used in the experimental set-up outlined in chapter 3. It is important to note at this point, that while the simulations were crucial for this work, they were in no way carried out by the author of this thesis. As such, the methodology of the simulations will be discussed so that its results can be properly understood, but the work itself should not be considered a part of this thesis.

The goal of these simulations is to solve for the fluid flow, so the resistance tensor - and with it the force acting upon the particle - can be determined for a range of particle shapes, sizes and intra-pair distances. From these simulation results, a force balance can be solved, to predict particle motion.

2.3.1. Simulation set-up

The simulations were carried out using COMSOL Multiphysics®. First, the Hele-Shaw geometry that is also used for the experimental work (the previously defined rectangular channel of height H) is defined in COMSOL. On the centreline of the channel, two particles are defined. These particles vary in size, shape, and intra-pair separation distance, but the pair always consists of two identical particles. As the geometry (including the particles that are discussed here) is symmetrical along the centreline and height of the channel, only a quarter of the simulation space will be solved for, as the other half consists of the mirrored solution.

The meshing of the solution space is done in a variable fashion. Having a coarse mesh for the bulk of the fluid and far away from any boundaries increases simulation speed. Meanwhile the integrity of the solution is still guaranteed by a fine mesh near those same boundaries, where slopes in fluid velocity are expected to be relatively high.

Boundary conditions are specified for the geometry, as well as an initial condition. Due to the time-independent nature of Stokes flow, the initial condition is trivial. To get a complete solution, COMSOL solves for the fluid velocity (in three dimensions) and the pressure field. This solution is generated using a direct, fully coupled solver.

Once the flow field is completely solved for, the stress acting upon the particles is integrated over all boundary elements to get the force acting upon the particle. This is done for three different situations: two particles at rest with an inlet pressure, and two simulations with no inlet pressure and a velocity ascribed to one of the particles. Having all three simulations allows one to solve a force balance which yields the relative velocity of the two particles for a certain background velocity. Given the fact that equation (2.25) is linear with respect to velocity, one can immediately express the intra-pair relative velocity as a dimensionless number, scaled with the background velocity.

2.3.2. Simulation results

The simulations as described above were used to identify the interactions between a pair of particles. We will be looking at two shapes of particle: tripods and dumbbells (or trimers and dimers, respectively), which are shown in figure 2.4. For both of these shapes, the change in interaction versus their disk-ratio was simulated, as well as the influence of the angle between the legs of tripods. Notably, each pair breaks the symmetry in the length-wise direction, as symmetric particles (such as disks) do not show any interaction.

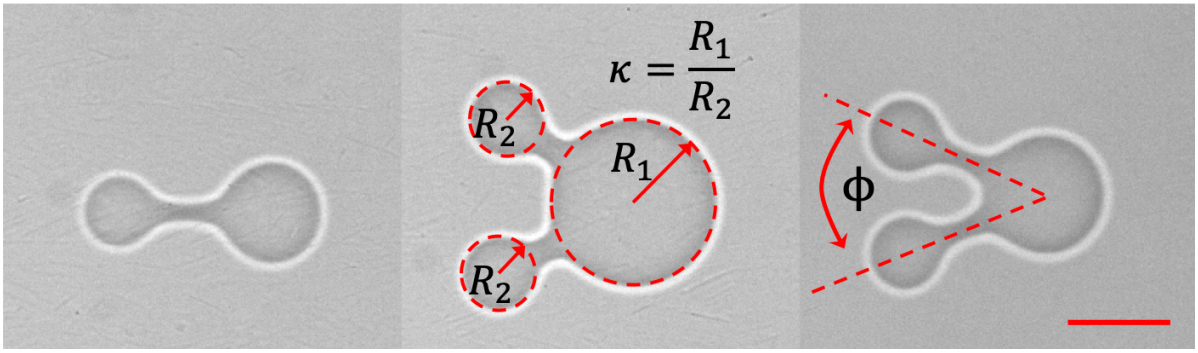

Figure 2.4: Examples of one dimer (or dumbbell) particle and two trimers (or tripods). All particles have different big to small disk ratio's (κ) and the tripods have two different leg angles (ϕ). Scale bar has a length of 100 µm.

Below, in figures 2.5 and 2.6, the results of the simulations that are of interest to us are shown. Overall, two things should be noticed here: all graphs generally show a strong net positive repulsion

peak $\Delta\dot{x}/u > 0$ where $\Delta\dot{x}$ is the relative velocity scaled by the background fluid velocity u, the horizontal axis shows the separation distance Δx scaled with the channel height H. Secondly, most of the graphs show a weak attraction well where $\Delta\dot{x}/u < 0$.

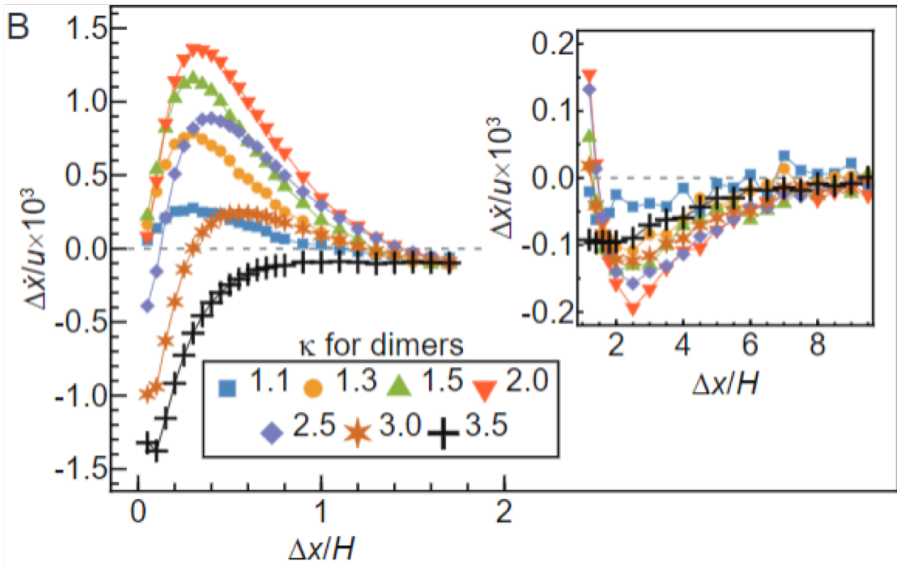

Figure 2.5: Dimer simulations along κ, where $\kappa = R_{\text{bigdisk}}/R_{\text{smalldisk}}$ with R_i being the radius of the big or small disk. $\Delta\dot{x}/u$ signifies the relative velocity between the pair, with a net positive value signifying repulsion, and a negative value signifying attraction.

Starting with the dimer graph in figure 2.5, we can see that all graphs, except for $\kappa = 3.5$ have a strong repulsion peak near $\Delta x/H = 0.5$. From there on out, the dimers experience a diminishing repulsion, which transitions into an attraction near $\Delta x/H = 2.0$. The interactions die out when $\Delta x/H \to \infty$, which is easily explained by the fact that the particles will no longer 'feel' each other's presence when the intra-pair distance is large. In other words, the particles scatter the fluid, causing these interactions, but at large distances, the flow field has been restored to its original situation.

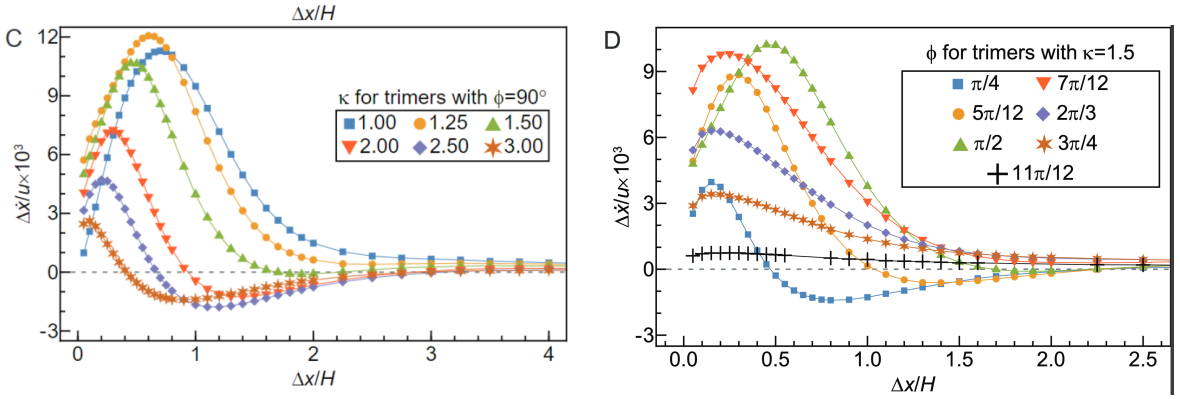

(a) Tripod disk ratio series

(b) Tripod angle series

Figure 2.6: Interaction graphs for Tripods where $\Delta\dot{x}/u$ signifies the relative velocity between the pair, with a net positive value signifying repulsion, and a negative value signifying attraction. (a) Tripod series over the disk ratio κ, where $\kappa = R_{\text{bigdisk}}/R_{\text{smalldisk}}$, with R_i being the radius of the big or small disk. (b) Tripod series over the angle ϕ in radians between the two tripod legs.

One thing that immediately stands out for tripods is that the interactions are much larger than for dimers. While relative velocities for dumbbells did not exceed $\Delta\dot{x}/H < 1.5$, for tripods we see that they reach an order of magnitude higher. In the experimental work, we will therefore expect that the interaction of tripods will be more noticeable than for the dimers. On top of that, tripods with $\kappa < 1.5$ and $\phi > 5\pi/12$ do not show an attraction well at all.

3

Methodology

This chapter begins with a general outline of the experimental procedures and techniques that were used. The various sections following this outline discuss the individual techniques in more detail. Exact protocols on channel fabrication, solution preparation and benchmarking can be found in appendix A. The chapter ends with a specification of the key equipment used.

3.1. General outline

Experiments start with the creation of a suitable Hele-Shaw geometry. Using soft-lithography techniques, as outlined by Whitesides et al. [18], channels are created that conform to this geometry. These channels — or microfluidic devices or chips — consist of polydimethylsiloxane (PDMS), a transparent and slightly flexible elastomer which is widely employed in academia for the creation of microfluidic devices. Examples include, but are not limited to, the work of Dendukuri et al [6, 7], Wexler et al [25] and Attia et al [1]. These channels encased in PDMS are then attached to glass microscope slides to complete the microfluidic device or chip, as shown below in figure 3.1a.

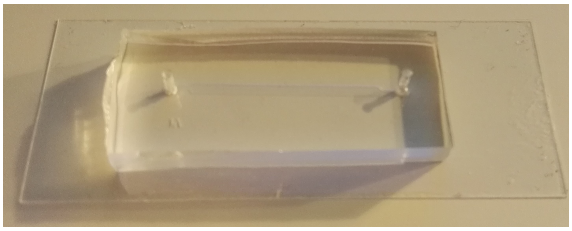

(a) Microfluidic device

(b) UV-light mask

Figure 3.1: Typical Examples of (a) a microfluidic device as used in the experimental set-up, and (b) a mask used to control the shape of a particle, by selectively blocking part of the light beam.

Particle creation within the channel is done using *Stop-Flow Lithography* (SFL), as originally described by Dendukuri et al [6]. The chip is placed on top of the microscope stage, and attached to a high-precision pressure pump. After proper set-up, a photoreactive solution is flown through the channel, which will polymerise when exposed to ultra-violet light. For particle creation, the flow is first stopped by controlling the pressure pump. While the fluid is at rest, a UV-pulse will be directed at the fluid leading to the polymerisation of a particle. The flow can then be started to observe the particle in motion.

The shape of the particle can be accurately controlled by placing a mask (shown in figure 3.1b) inside the pathway of the UV-light, thereby selectively blocking part of the light beam. This results in a UV-light projection of the mask on the chip. The resulting projection is passed through the magnification

objective of the microscope. This allows for both accurate control over the position of the projection, and an intensification of the light beam.

3.2. Creating polymer particles

The creation of the polymer particles (or hydrogel particles) consists of two parts: one part theory on why and how these particles are formed, and one part fine-tuning of system parameters to get the 'perfect' particle to carry out experiments with. The former is described below and starts with the reaction mechanism that governs particle formation. The latter has been standardised to a certain degree, and is described in appendix A.3. All the available masks used within this project can be viewed in appendix B.

3.2.1. Reaction mechanism

The photoreactive mixture that is used to produce particles within the microfluidic device consists of two parts; The bulk of the solution is the oligomer poly(ethyleneglycol)-diacrylate (PEG-DA). The oligomer has varying chain lengths and as such is characterised by its mean molecular weight M_n. The properties of the different varieties of PEG-DA can be seen in table 3.1.

Table 3.1: Properties of different varieties of PEG-DA and the photoinitiator Darocure. M_n, ρ and μ are the (average) molecular weight, density and viscosity, respectively. † Viscosity not listed by manufacturer

M_n [g mol^{-1}]	ρ [kg m^{-3}] at 25 °C	μ [mPa s] at 25 °C	Refractive index [-]	Manufacturer	
		PEG-DA varieties			
700	$1.12 \cdot 10^3$	- †	1.470	Sigma-Aldrich	[16]
575	$1.12 \cdot 10^3$	57	1.467	Sigma-Aldrich	[15]
400	$1.12 \cdot 10^3$	57	1.466	Polysciences	[12]
250	$1.11 \cdot 10^3$	- †	1.463	Sigma-Aldrich	[14]
		Photoinitiator (2-Hydroxy-2-methylpropiophenone)			
164.2	$1.08 \cdot 10^3$	- †	1.533	Sigma-Aldrich	[13]

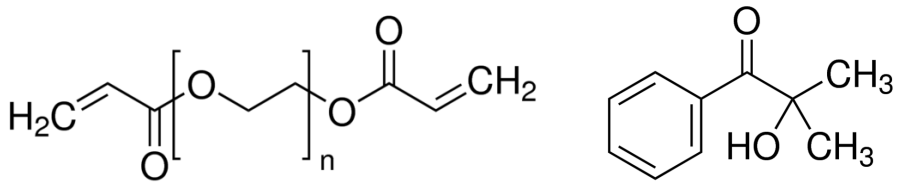

(a) Molecular structure of PEG-DA

(b) Molecular structure of Darocure 1173

Figure 3.2: Molecular structures of PEG-DA [16] and 2-hydroxy-2-methylpropiophenone (Darocure 1173) [13], the photo-initiator.

A smaller part of the solution (generally between 1-10%) is a polymerisation initiator (2-hydroxy-2-methylpropiophenone) that is activated by UV-light. The properties of this photoinitiator (PI) are also listed in the previously mentioned table. The molecular structure of both PEG-DA and the PI are shown in figure 3.2. This process, called free-radical photopolymerisation, can be described by the simplified reaction mechanism below (table 3.2, as taken from Dendukuri et al. [7]).

The first four steps of the reaction mechanism are essential to creating the particles of our desire: from the mixture of single oligomer strands, a large cross-linked polymer block or hydrogel is created. This starts with the photoinitiator being activated by UV-light, thus creating a radical species (Ṙ). This radical will react with a PEG-DA (M) strand which forms the new radical species, and initiating the chain. This chain is propagated by multiple additions of other PEG-DA strands which can react with the radical. When two radicals react with each other, the chain is terminated and the a stable polymer hydrogel has been formed. The chain can also be terminated by a reaction with oxygen as shown in step five.

Table 3.2: Simplified reaction mechanism of the free-radical photopolymerisation of the used photoreactive mixture, as proposed by Dendukuri et al. [7]. PI is the photoinitiator, R is the photolysed product of PI, and M is a PEG-DA chain. k_p, k_t and k_O are the rate constants for the propagation, termination and oxygen inhibition step, respectively. The n and m suffixes represent the lengths of the polymer at a certain step.

#	Reaction	Mechanism step
1	$\mathrm{PI} \xrightarrow{h\nu} \dot{\mathrm{R}}$	Photolysis
2	$\dot{\mathrm{R}} + \mathrm{M} \longrightarrow \mathrm{R}\dot{\mathrm{M}}$	Chain initiation
3	$\mathrm{R}\dot{\mathrm{M}}_n + \mathrm{M} \xrightarrow{k_p} \mathrm{R}\dot{\mathrm{M}}_{n+1}$	Chain propagation
4	$\mathrm{R}\dot{\mathrm{M}}_n + \mathrm{R}\dot{\mathrm{M}}_m \xrightarrow{k_t} \mathrm{RM}_n\mathrm{M}_m$	Chain termination
5	$\mathrm{R}\dot{\mathrm{M}}_n + \mathrm{O}_2 \xrightarrow{k_{O_2}} \mathrm{RM}_n\mathrm{OO}$	Inhibition

3.2.2. Inhibition mechanism

The termination due to a reaction with oxygen has another beneficial effect on our system, since it can prevent particles from becoming stuck inside the channel. Oxygen diffuses into the liquid through the PDMS walls, creating an inhibition layer near the PDMS [7, 8, 25]. As such, a particle will grow outwards from the centre of the channel [7], and is initially prevented from getting stuck to either the ceiling or the floor of the channel. Only when the oxygen near the walls has been depleted to a large degree, will the particle grow so thick that it will no longer be able to flow. It is convenient to know the time-scale of this process, which can be obtained through a species balance:

$$\frac{\partial[\mathrm{O}_2]}{\partial t} = D_{\mathrm{O}_2}\frac{\partial^2[\mathrm{O}_2]}{\partial z^2} - k_{\mathrm{O}_2}[\dot{\mathrm{X}}][\mathrm{O}_2] \tag{3.1}$$

where $[\mathrm{O}_2]$ is the oxygen concentration in the oligomer medium and $[\dot{\mathrm{X}}]$ is the concentration of all radicals in that same medium. D_{O_2} and k_{O_2} are the diffusivity of oxygen in PEG-DA and the reaction coefficient of the inhibition step, respectively.

The following boundary conditions and initial condition can be applied:

$$(1)\quad [\mathrm{O}_2](t,0) = \theta_{eq} \qquad (2)\quad \frac{\partial[\mathrm{O}_2]}{\partial z}\left(t,\frac{H}{2}\right) = 0 \qquad (3)\quad [\mathrm{O}_2](0,z) = \theta_{eq} \tag{3.2}$$

with c_{eq} the equilibrium concentration of oxygen in PEG-DA and H the channel height. The diffusivity of oxygen in PEG-DA ($\mathcal{O}(D_{\mathrm{O}_2}) = 10^{-6}$ cm^2 s^{-1}) is significantly lower than the diffusivity of oxygen in PDMS ($\mathcal{O}(D_{\mathrm{O}_2}) = 10^{-4}$ cm^2 s^{-1}) [17]. We can therefore assume a constant oxygen concentration at the interface between PDMS and PEG-DA, leading to boundary condition (1). Boundary condition (2) is a symmetry condition along the centreline of the channel. Note that this approximation is slightly flawed, as it does not account for the glass slide underneath the device. The initial condition (3) is justified by assuming complete oxygen saturation prior to the experiment.

Based on the PI's rate of absorption of UV-light, Dendukuri et al. [7] proposed the following formula for the concentration of radicals $[\dot{\mathrm{X}}]$ in the medium:

$$[\dot{\mathrm{X}}] = \frac{-k_{\mathrm{O}_2}[\mathrm{O}_2] + \sqrt{(k_{\mathrm{O}_2}[\mathrm{O}_2])^2 + 4r_a k_t}}{2k_t} \tag{3.3}$$

where k_t is the rate coefficient of chain termination and r_a is the rate of radical production, which can be expanded to be:

$$r_a = \phi\epsilon[\mathrm{PI}]I_0\exp(-\epsilon[\mathrm{PI}]z) \tag{3.4}$$

where ϕ, ϵ and I_0 are the quantum yield of formation of radicals, molar extinction coefficient and light intensity, respectively. Using the following scales:

$$[\mathrm{O}_2] = \theta_{eq}\theta \qquad z = \frac{H}{2}\eta \qquad t = \frac{H^2}{4D_{\mathrm{O}_2}}\tau \tag{3.5}$$

and substitution of equations (3.3) and (3.4), we can nondimensionalise species balance (3.1) to yield:

$$\frac{\partial\theta}{\partial\tau} = \frac{\partial^2\theta}{\partial\eta^2} + Da_1\,\theta\left(\theta - \sqrt{\theta^2 + \alpha\exp(-\beta\eta)}\right) \tag{3.6}$$

with

$$\alpha = \frac{4\phi\epsilon[\mathrm{PI}]I_0 k_t}{(k_{\mathrm{O}_2}\theta_{eq})^2} \qquad \beta = \frac{\epsilon[\mathrm{PI}]H}{2} \qquad Da_1 = \frac{k_{\mathrm{O}_2}^2\theta_{eq}H^2}{8k_t D_{\mathrm{O}_2}} \tag{3.7}$$

and boundary conditions:

$$(1)\quad \theta(\tau,0) = 1 \qquad (2)\quad \frac{\partial\theta}{\partial\eta}(\tau,1) = 0 \qquad (3)\quad \theta(0,\eta) = 1 \tag{3.8}$$

The Damköhler number Da_1 signifies the ratio of the oxygen inhibition reaction over the diffusion of oxygen into the channel. A similar analysis can be done to model the competition between the chain propagation (step (3)) and oxygen diffusion. The species balance for unreacted oligomer [M] reads:

$$\frac{\partial[\mathrm{M}]}{\partial t} = -k_p[\dot{\mathrm{X}}][\mathrm{M}] \qquad \text{with initial condition:} \qquad [\mathrm{M}](0,z) = M_0 \tag{3.9}$$

where M_0 is the initial concentration of oligomer. Diffusion of oligomer is assumed to be negligible, due to the extreme size of one oligomer-strand. Scaling of the previous species balance yields:

$$\frac{\partial\xi}{\partial\tau} = Da_2\,\xi\left(\theta - \sqrt{\theta^2 + \alpha\exp(-\beta\eta)}\right) \tag{3.10}$$

where ξ is the scaled oligomer concentration [M], and Da_2 is the Damköhler number, according to:

$$[\mathrm{M}] = M_0\xi \qquad Da_2 = \frac{k_p k_{\mathrm{O}_2}\theta_{eq}H^2}{8k_t D_{\mathrm{O}_2}} \tag{3.11}$$

The two expressions for Da_1 and Da_2 allow us to get a feel for the timescale of oxygen diffusion relative to the timescales of the inhibition reaction (step (5)) and the chain propagation (step (3)). This becomes apparent when rewriting both Damköhler numbers:

$$Da_1 \sim \frac{H^2}{D_{\mathrm{O}_2}}\left(\frac{k_t}{k_{\mathrm{O}_2}^2\theta_{eq}}\right)^{-1} = \frac{t_D}{t_{\mathrm{O}_2}} \qquad \text{and} \qquad Da_2 \sim \frac{H^2}{D_{\mathrm{O}_2}}\left(\frac{k_t}{k_p k_{\mathrm{O}_2}\theta_{eq}}\right)^{-1} = \frac{t_D}{t_p} \tag{3.12}$$

where t_D, t_{O_2} and t_p signify the characteristic timescales of oxygen diffusion, the oxygen inhibition reaction (5), and the propagation reaction (3), respectively. Table 3.3 shows high Damköhler numbers on the order of $Da_1 \sim 10^9$ and $Da_2 \sim 10^5$, signifying that the timescale of oxygen diffusion is much greater than the other timescales:

$$t_D \gg t_{\mathrm{O}_2} \qquad \text{and} \qquad t_D \gg t_p \tag{3.13}$$

Physically, this shows us that both reactions (3) and (5), which happen on a relatively small timescale, dominate the slower oxygen diffusion. We can therefore expect the oxygen that is initially present in the oligomer to deplete very rapidly, after which the propagation reaction (along with the termination reaction) will carry on unhindered. Meanwhile, the inhibition reaction will prevent any oxygen from significantly penetrating into the oligomer, keeping it locally depleted.

In the results section 4.4 it is shown that Dendukuri only paints part of the picture; For our experimental method, a 1D-analysis proved insufficient to correctly estimate the particle thickness, but most importantly, it was shown that particle projection size or perimeter plays a role in it's thickness.

3.3. Measuring pairwise interactions

The aim of this thesis is to show experimentally that pairwise interactions not only exist, but are also dependent on shape. A great deal of work consists of adequately creating a reproducible pair of particles with which we can measure this, but that is only half the story. Once the pair has been produced,

Table 3.3: General parameters relating to the chemical reactions or oxygen diffusion, as well as some relevent dimensionless numbers calculated using these parameters. Values taken from Dendukuri et al. [7] unless denoted with a "†", signifying that the value was measured or calculated by the author of this thesis.

Parameter	Value	Units
k_p	25	$m^3\,mol^{-1}\,s^{-1}$
k_t	2520	$m^3\,mol^{-1}\,s^{-1}$
k_{O_2}	$5 \cdot 10^5$	$m^3\,mol^{-1}\,s^{-1}$
D_{O_2}	$2.84 \cdot 10^{-11}$	$m^2\,s^{-1}$
$H^\dagger$	82	µm
I_0	$1.5 \cdot 10^{-2}$	$E\,m^{-2}\,s^{-1}$
[PI]†	197.32	$mol\,m^{-3}$
ϵ	1.6	$m^2\,mol^{-1}$
θ_{eq}	1.5	$mol\,m^{-3}$
ϕ	0.6	-
Dimensionless numbers and parameters		
$Da_1{}^\dagger$	$4.30 \cdot 10^9$	-
$Da_2{}^\dagger$	$2.15 \cdot 10^5$	-
$\alpha^\dagger$	$5.1 \cdot 10^{-8}$	-
$\beta^\dagger$	$12.8 \cdot 10^{-3}$	-

it will be recorded while flowing along inside the channel. Using image processing techniques, we will obtain data about the position of the particles for each time-step recorded. This data is then processed further to obtain the relative velocity that the particles have with respect to each other. This is done by fitting a line to the trajectory of each particle, and then subtracting their slopes.

For repelling particles, we expect a net positive relative velocity (the upstream particle is moving slower than it's downstream counterpart) and similarly we expect negative relative velocities for attracting particles. To improve the quality of the results, each experiment (that is a certain particle shape at a certain initial separation distance) is repeated ten to fifteen times. For all these repetitions, the relative velocity is calculated, after which an average can be calculated with a certain standard deviation.

We will repeat this procedure for multiple shapes of particles, at varying initial separations, to obtain a graph similar in nature as those resulting from the simulations of section 2.3.2.

3.4. Equipment specification & microscope set-up

The set-up starts with a 130 W mercury lamp (Nikon) with a strong UV-component. The lamp-unit furthermore consists of a manual shutter and a range of neutral density filters (ND2, ND4, ND8, ND16, ND32), which allows us to control the intensity of the beam. This unit is connected to an automated shutter through an optical cable. This shutter can be controlled through the Nikon camera software with minimal latency, and allows for accurate exposure times for $t_{exp} > 0.1\,s$. Included within this shutter-unit are two additional ND4 and ND8 filters, and a regular neutral density filter (ND1). This shutter-unit was directly attached to the Nikon TI-Eclipse inverted microscope, and leads to a turret containing multiple filters. These filters cut certain wavelengths from the beam, so only a select range is passed through. In this way, we transform the light of our mercury lamp into an intense UV-light beam. Afterwards, the light is passed through the mask holder, giving the light beam its intended shape, and is magnified through the camera objective.

The fluid flow is controlled by hooking up the in-/outlet to an 8-channel Fluigent MFCS™-EX microfluidics flow controller system. The first four channels allow for continuous pressures ranging from 0 mbar to 69 mbar. The pressures have to be manually adjusted, but can be fine-tuned realtime to obtain the desired flow state. The inlet has been connected through a Solenoid three-way valve (normally open), which can be controlled through the Nikon camera software. This allows us to automate the stop and start of fluid flow to a certain degree.

4

Results and discussion

This thesis had two main goals: firstly, to improve the set-up with regards to both reproducibility and accuracy, and secondly, to use this improved set-up to show the existence of shape-dependent pairwise interactions. Experiments played a crucial part in improving the set-up, so as to allow for the second goal to be achieved. The chapter is therefore structured to first show experimental data that led to certain improvements. The data, corresponding discussion, and resulting improvement are detailed in section 4.2.

Furthermore, it is important to remember while reading this chapter, that all these experiments were carried out on the microscale. Noise and small inconsistencies therefore cannot be avoided. Noise will be reduced as much as possible, and frequently occurring inconsistencies or anomalies are highlighted and discussed in section 4.1.

In the duration of this project, some relevant observations with regards to the experimental method were made that were important for the successful generation of pairwise interaction data. The second part of this chapter discusses these observations. Most importantly, it is shown that the one-dimensional model as proposed by Dendukuri [7] is incomplete once one considers different shapes. Furthermore, it is shown that with the current set-up, the intra-pair particle height is always skewed in favour of higher down-stream particles. Due to time and material constraints, this flaw could not be remedied.

The third part of this chapter (section 4.5) will deal with the experiments related to showing pairwise interactions, and their dependency on shape. Unless specified otherwise, the data will have been generated using the improvements and observations that were discussed earlier in this chapter.

4.1. Anomalies, inconsistencies and noise

Prior to properly evaluating a certain improvement, we need to be able to discern random noise, anomalies or inconsistencies from the actual data. The most important and frequently occurring one are channel defects, which will be discussed first. Afterwards, inconsistent data points and the amount of noise present in the data will be discussed.

4.1.1. Channel defects

An anomaly within the channel (or a channel defect) can be described as a point within the channel, at which $H \neq 82\,\mu\text{m}$, but some other value. Examples of this are dirt from the channel production process which has become trapped inside, or small defects present on the mould that was used for casting the channels. Regardless of origin, a channel defect will always interfere with the motion of particles, and affects both its translational and rotational velocities. Fortunately, these defects are easy to spot while carrying out experiments, and are also clearly present within the processed data, as shown in figure 4.1.

As is clear from the graph, a channel defect can often be recognised by two distinct features: a sudden jump in separation distance, and the individual experiments taking a distinct and unique path through the channel. The jump is caused by the downstream particle interacting with a channel defect; the locally higher or narrower channel alters the gap height and thus the confinement experienced by the downstream particle. As a consequence, the particle will suddenly speed up or slow down,

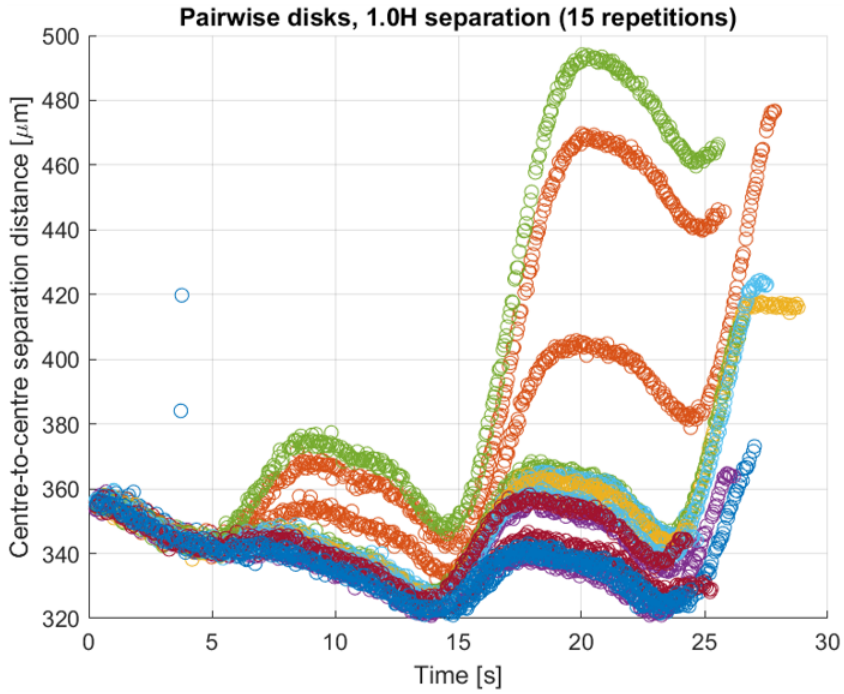

Figure 4.1: Example of channel defects that interfere with the flow behaviour of the particles. The separation distance of the particles (based on the centres of both particles) in µm is plotted versus time: in other words, the graph shows the variation in separation as they travel inside the channel. This experiment was carried out with a pair of disks that should not interact: one expects a straight line, as can be seen until roughly $t = 5\,\mathrm{s}$. Afterwards, a sudden change in separation distance can be noticed, symbolising a defect. Similar defects can be noticed further into the experiment. Inconsistencies can also be spotted around $t = 4\,\mathrm{s}$, where two data points are seemingly detached from any graph.

depending on the nature of the defect. Meanwhile, the upstream (or trailing) particle carries on with its unaltered speed, causing it to either catch up to or further lag behind the downstream particle, which leads to the sudden change in separation distance.

As particle thickness varies slightly for each iteration of an experiment, each pair of particles will react slightly different when confronted with a defect: a highly confined particle will experience a much stronger interaction with a channel defect, than one that is relatively thin. As such, all pairs belonging to the same experiment will travel along a significantly different path once confronted with a defect, causing a large spread in the data. For example, in the previously shown figure 4.1, it is evident that the topmost three pairs were strongly affected by the defect, while the other twelve pairs carry on with only a minor disturbance.

Because defects can be easily spotted, they provide a natural cut-off point for generated data. For all of the data discussed in section 4.5, cut-off points will be defined based on locating these defects and any data after this point will no longer be considered.

4.1.2. Inconsistent data points

Apart from the channel defects, figure 4.1 also shows two inconsistent data points near $t = 4\,\mathrm{s}$, at 380 µm and 420 µm. These data points are detached from any graph, and are the result of a small processing flaw. While tracking the particles, the stage upon which the sample rests is shifted at certain intervals so the particles won't flow out of camera view. Sometimes, the camera captures a frame while the stage is moving as shown in figure 4.2. During such a frame, the processing script misrecognises both the stage-position and the location of both particles, resulting in misaligned data points. Such data points can immediately be disregarded when spotted, and won't significantly affect any calculations done using this data, as the amount of frames taken vastly outnumbers the seldom occurring inconsistent ones.

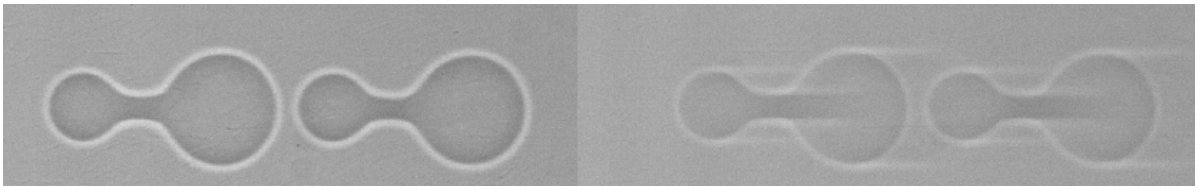

Figure 4.2: Comparison between (part of) a normal frame (left) and one captured during stage-movement (right). The latter frame will be produce an inconsistent data point, due to an incorrect stage position, and improperly recognised particles by the image-processing script.

4.1.3. Noise and error within data sets

Since the processing of a recording relies on image-processing techniques, there will always be some amount of noise present. The amount of noise basically depends on three aspects: the magnification used while tracking particles, the 'correctness' of the focal point used while tracking, and the precision of the image processing itself. The magnification used while tracking the particles directly relates to the size of a pixel: for example, 10x magnification will produce a pixelsize of $p_{x,10} = 0.6496\,\mu\text{m/px}$, while 20x magnification has half of that $p_{x,20} = 0.3248\,\mu\text{m/px}$. It is clear when measuring something, that being one pixel off will provide a greater error when using 10x as opposed to 20x. Since 20x is inconvenient when recording over larger distances, the decision was made to use 10x for regular recordings, and thus accept the inferior accuracy.

The image-processing technique relies on focussing somewhat above the particle, causing a white halo to appear: the contrast between white and dark is used to recognise the boundaries of the particles. In itself, this already introduces noise due to the halo eating partly into the true size of the particle. Furthermore, the exact width and position of this halo is affected by the choice of focal point. Since this focal point is not necessarily constant along the entire channel, the noise that arises here is variable, but will be on the order of half the halo size, according to experimental experience.

Lastly, a certain error is associated with the image-processing technique itself. As mentioned before, this error decreases or increases with pixelsize. The error stems from the fact that the processing script sometimes includes (part of) the halo that was previously described. Due to this, there is always some fluctuation in the exact position and size of the disk.

4.2. Improvements

At the start of this project, the set-up proved to be unable to provide the sought-after data on pairwise interactions. The desire to work with higher channels than previously used within the group (82 µm over 33 µm) caused the particles to be over-susceptible to anomalies. Apart from that, the experiments were too inaccurate to be able to directly measure the pairwise interactions. Many of these troubles turned out to be caused by variations in the thickness of particles. Most of the improvements outlined in this section will therefore affect the particle thickness in a certain way. A summary of the improvements is given below in table 4.1.

Table 4.1: List of set-up improvements, showing the variable they affect, and in what way, and the respective subsections in which they are discussed. † This improvement will not be discussed in depth in this chapter, as the appendix details the entire procedure and its reasoning. Apart from that, the old procedure was not well documented, so no proper comparison between the old and new procedure can be made.

Change in method	Variable affected	Resulting improvement	Section
10x vs 20x objective	Depth of field	Decreased particle deformation	4.2.1
Channel production procedure	Cleanliness	Channel defect reduction	A.1†
Ambient pressure compensation	Ambient velocity	Increased thickness reproducibility	4.2.2
Pairwise production method	Particle thickness	Matching thicknesses within pair	4.2.3

4.2.1. Choice of objective: 10x vs 20x

When producing a particle, the UV-light beam that produces the oligomer radicals is focussed onto the channel by the microscope objective. Changing this objective for one with a different magnification,

allows us to affect (amongst others) the depth of field, and the projected size of the mask image. The latter was corrected for by creating multiple sets of masks, that belong to a certain magnification. In this way, particles of a certain size could be created by both a 10x or 20x objective.

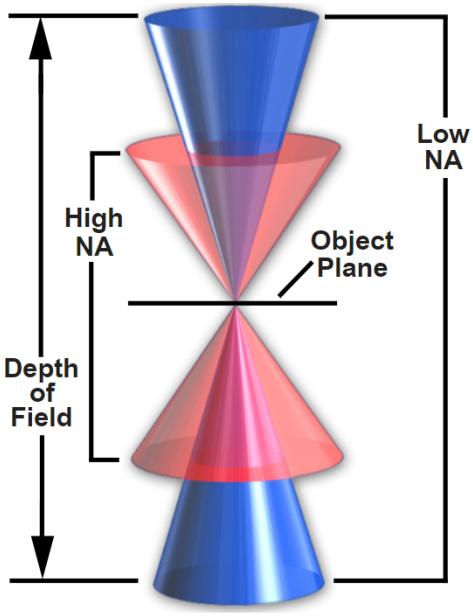

Figure 4.3: Illustration of depth of field. The red cones have a smaller depth of field than the blue cones. Taken from ©Nikon Instruments inc. [21]

Having both sets of masks, meant that the choice of objective comes down to a preference in depth of field. The concept of depth of field is illustrated in figure 4.3, and is defined as "the distance from the nearest object plane in focus to that of the farthest plane also simultaneously in focus." [21]. Due to other set-up constraints, we are limited to 10x and 20x objectives, and their respective depths of field: d_{10} =8.5 µm and d_{20} = 5.8 µm [21]. Perhaps counter-intuitively, the smaller depth of field of the 20x objective was easier to work with, and provided better results. In contrast to the 20x objective, the 10x objective proved to be somewhat insensitive to the choice of focal point, making it hard to properly focus. This is particularly important for the shape of the particle in the height direction: while the particle projection - that is, its in-plane shape - might be fine, it can be skewed along the height.

For 20x objective, a range of approximately 20 µm can be deterimined in which a flipped rod seems rectangular. For the 10x objective, this range is significantly larger, which makes it harder to pin-point the proper focal point. The choice of objective to produce a particle was therefore changed to 20x.

4.2.2. Ambient flow correction

Making sure that the fluid is at a complete standstill at the time of particle production is crucial to getting reliable and reproducible results, in terms of particle thickness and projection integrity. A three-way valve was installed before the channel inlet, allowing us to set an ambient correction pressure, as well as a regular pressure to induce flow. The supplied pressure consisted of two components:

$$\Delta P_{tot} = P_{back} + P_{flow} \tag{4.1}$$

with P_{back} being the pressure needed to let the fluid be at rest, and P_{flow} the additional pressure to induce flow. While P_{flow} is kept constant for all experiments, P_{back} is manually adjusted as needed to keep the fluid at rest. In this way, we ensure that the fluid velocity is constant among all experiments.

4.2.3. Pairwise particle production method

A supply of masks containing single particles on them, was left over from previous work done by the group. As such, using single-particle masks was a natural starting point for the experiments. Two methods were devised to create a pair of particles: one involving the production of a particle, moving the (microscope) stage to a different position, and then creating a second particle. The second technique

was based on producing a particle, temporarily switching on fluid flow to move the first particle out of the way, and then creating a second particle.

The first technique (stage-movement) was the easiest to implement, but had a few disadvantages: particles were never precisely on the same streamline (for instance, when the channel was at a slight angle with respect to the microscope stage) and the two particles were not produced at the same location. This last fact resulted in possible variation in particle thickness, due to the fact that the UV-light takes a slightly different path.

The second technique (flow-movement) solved both disadvantages of the stage-movement technique; Particles were both created in the same spot in the channel, and because the first particle was flown downstream from the production-site, both particles were necessarily on the same streamline. Unfortunately, this technique had some reproducibility issues. Switching off/on the flow introduces a small temporal effect due to the channel expanding and relaxing upon changes in pressure [6]. This caused the initial separation distance of the particles both hard to control and somewhat susceptible to random variations. This last effect was worsened by the fact that switching the flow on or off (while automated) still had a significant and random lag. The exact time for which fluid had flown (and with it, the resulting separation distance) was therefore unknown and varying. Making multiple repetitions of the same experiments therefore proved difficult.

Despite these small difficulties, the largest error for both of these techniques were variations in the light intensity. Even while settings remain unchanged, each repetition of an experiment will have a slight variation in the exact of amount of light leading to particle synthesis. For both methods described above, particle thickness varied by as much as 3 µm within a pair. Such large differences among the pair causes a high difference in particle velocity ($\mathcal{O}(10)$ µm s^{-1}), while the interactions we'd like to measure are much smaller ($\mathcal{O}(1)$ µm s^{-1}) [9]. In summary, both techniques lack reproducibility and consistency both between experiments, and within one experiment (or pair).

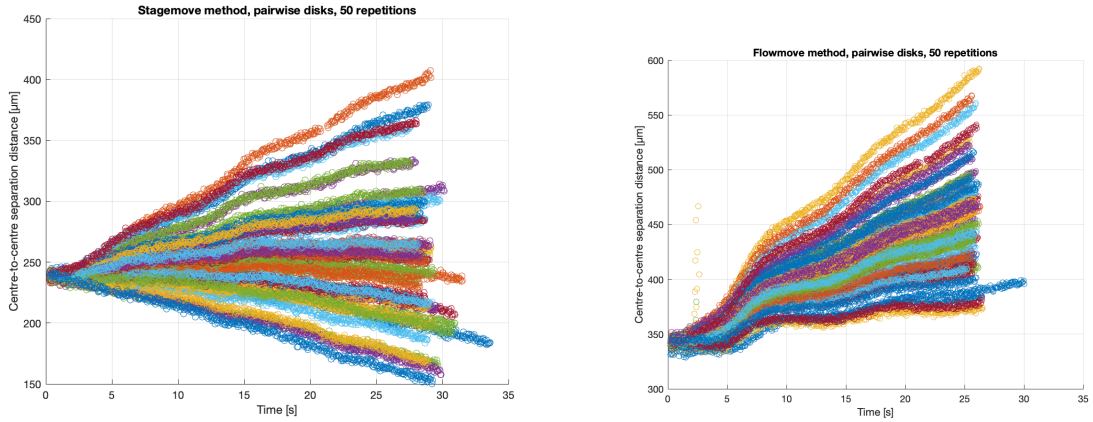

Figure 4.4: Separation distance of pairs of particles plotted versus the time. The left-hand graph was generated with the stage-move technique, while the right-hand graph used the flow-move technique. For both graphs, it is apparent that the spread between the repetitions is extremely large.

Visually, this is immediately clear when looking at figure 4.4. For both techniques, 50 repetitions of pairwise disks were created and tracked. Ideally these should all follow roughly the same pathway through the channel, but the graphs shows a large spread in the data instead. Relative velocities range approximately from −3 µm s^{-1} to 8 µm s^{-1} and from 1 µm s^{-1} to 10 µm s^{-1} for the stage-move and flow-move technique, respectively.

To remedy this large spread in data, a third technique was developed that employed masks with a pair of particles on them instead of just a single particle. By creating both particles of the pair in one single exposure event, we eliminate any variation in intensity within the pair itself. While the thickness will still vary between repetitions, the results were significantly improved over the old techniques, as shown in figure 4.5a.

The improvement of the 2-particles-1-mask technique is obvious when quantitatively comparing the spread in relative velocities. For this technique, the relative velocities ranged from −0.5 µm s^{-1} to 0.1 µm s^{-1}, which is a factor 30 smaller spread compared to the flow-move method. Figure 4.5b shows

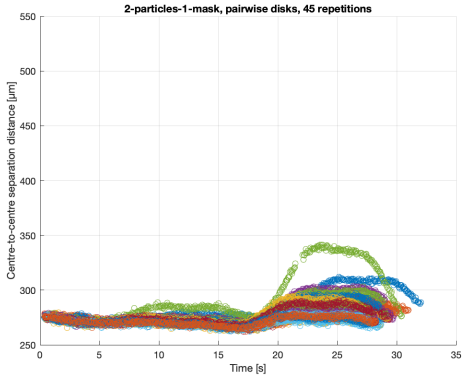

(a) Pairwise disks, 2-partiles-1-mask

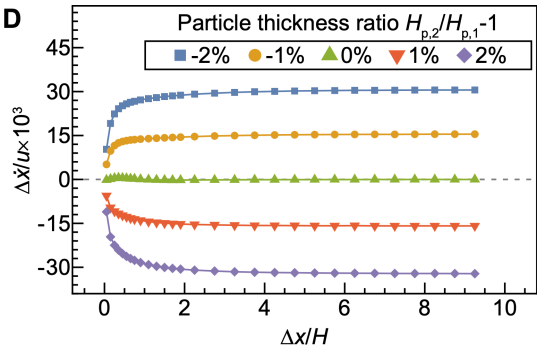

(b) Simulations on intra-pair thickness difference

Figure 4.5: (a) Example of 50 repetitions of pairwise disks using the 2-particles-1-mask technique. The length of the vertical axis was taken from the previously shown flow-move graph, to highlight the significantly reduced spread in data: all 45 repetitions initially follow the same route, until interference of a channel defect around $t \approx 18$ s. (b) Simulations on the effect of mismatching particle thickness within a pair [9]. Small mismatches will already cause large relative velocities, as was observed with the flow-move and stage-move techniques.

why this improvement is so large: even small mismatches in particle thickness within a pair, already lead to large relative velocities. By creating a pair with a single exposure event, we force them to have similar thicknesses.

These results have been summarised in table 4.2, and the 2-particle-1-mask technique was chosen for further experimental work.

Table 4.2: Summarises the results for each method tested for particle pair production. The 2-particle-1-mask technique outperforms the other two techniques by an order of magnitude for both the spread in data and its standard deviation. Spread size signifies the spansize of the relative velocity for multiple iterations of the same experiment.

	Stage-move	Flow-move	2-particles-1-mask
Spread size [µm s^{-1}]	9.40	8.35	0.62
Standard deviation [µm s^{-1}]	2.13	1.89	0.15

4.3. Time reversibility and non-uniform light beam

Raw data for the measurements and graphs contained in this section can be viewed in appendix C.

One of the implications of Stokes' flow is that time should not be a factor in the flow behaviour. This leads to time reversibility within the system: simply put, if a particle flows for a certain time τ, then the exactly reversed flow will make the particle retrace its steps back to its original position. The path taken, and the initial and ending position should be identical. To show that time-reversibility applies, three experiments doing exactly this were carried out, the results of which can be seen in appendix D.

By mirroring and superimposing the return path onto the original pathway of the particle, we can see if trajectories indeed match. For all three experiments, the return path agrees very well with the original path, though a minor mismatch in velocity (approximately 2.5 µm s^{-1}) can be noticed along the entire length of the path. A very simple explanation for this effect is a slightly different return pressure: 0.1 mbar (or 2.5% of the total pressure drop) of pressure difference would cause such a velocity difference.

4.3.1. Thinner upstream particles

During the many experiments carried out for this thesis, it became apparent that almost all particle pairs exhibited an attractive relative velocity. This included symmetric particles, such as disks, which should have no interaction (and thus no relative velocity) according to simulations [9]. The attraction was very constant in nature, with a value ranging from −1.5 µm s^{-1} to −2.0 µm s^{-1}, regardless of device

or position. As shown before in figure 4.5b, a mismatch of intra-pair particle thickness will lead to a significant relative velocity. Having such a consistent mismatch in particle thickness would explain this relative velocity. To determine whether this was the case, 30 pairs of rods were measured, using 30x magnification for increased precision.

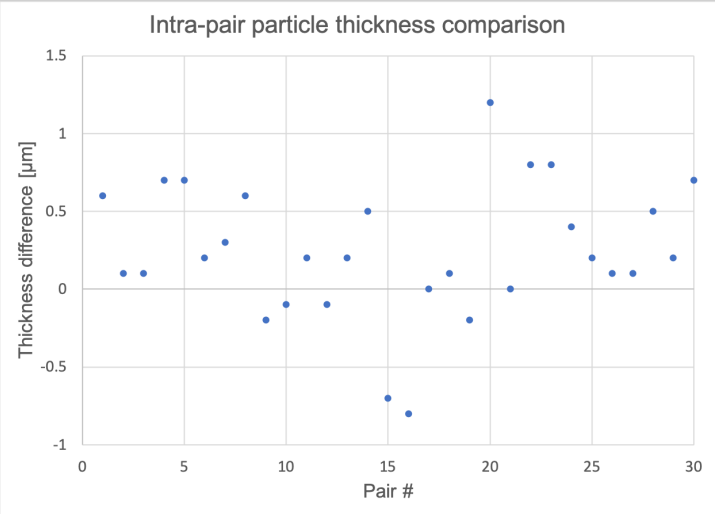

Figure 4.6: Comparison of intra-pair particle thickness. The vertical axis lists the difference in particle thickness, as given by $\delta_{\text{down}} - \delta_{\text{up}}$, where δ_i is the thickness of the up-/downstream particle in [µm]. The horizontal axis lists the repetition number. A positive difference indicates that the upstream particle is the thinner one, and vice versa.

The results of this experiment are shown in figure 4.6 and paint a clear picture. For the vast majority of pairs, the upstream particle is the thinner one, by approximately 0.3 µm. Having a thinner upstream particle, means that it will always catch up to the thicker downstream particle. When performing experiments this will indeed result in a seeming attraction between the particles. This knowledge is crucial when discussing the upcoming results regarding pairwise interactions. Knowing that the intra-pair particle thickness always mismatches in favour of thinner upstream particles, means our results will be skewed: non-interacting pairs will seem to attract, while weak repulsion will manifest as a 'reduced attraction'.

4.3.2. Non-uniformity of light beam

While the discrepancy in particle thickness explains the constant relative velocity for non-interacting pairs, it is still unclear what causes it in the first place. Regular channel defects and masks not place dead-centre inside the mask holder were ruled out: the former due to the consistency of the relative velocity regardless of device or position, and the latter was ruled out because this would cause a random effect. If a mispositioned mask in one direction would cause attraction, then it would follow that it would cause repulsion if misplaced in the other direction and no relative velocity if it was perfectly in the centre of the holder. The constant bias towards thinner upstream particles therefore rules this out. Differences in refraction of the mask material was also ruled out by flipping the mask upside down: particles produced in this manner behaved identically when compared to a set taken with the mask 'right' side up.

A non-uniform UV-light beam is a plausible cause of a constant bias towards thinner upstream particles. If the trailing particle is always hit with slightly fewer photons, it will consistently propagate less with respect to the downstream particle. To test this idea, the channel was physically rotated 180°, and the mask was rotated in such a way that the pair of particles would still be produced with the stable orientation with respect to the streamline. In this way, the particles will still travel along the same path as they regularly do, but with one key difference: what is normally the upstream particle, has now become the downstream particle and vice versa. In other words, the entire system has been rotated 180°, with the exception of the light beam. Therefore, if the beam is skewed to produce a thinner particle on the right hand side, that would result in a thinner upstream particle in the regular set-up, but a thinner downstream particle in the rotated set-up.

This somewhat confusing rotation of the set-up was necessary to de-couple time-reversibility from

Table 4.3: Comparison of relative velocities for the regular set-up, and a rotated system as described above. By rotating the entire system except for the light-beam, particles will travel along the same path as usual, but what is normally the upstream particle will now be the downstream particle and vice versa. Comparison consists of the average of (at least) five repetitions for each shape. Shapes are described by their geometry, separation and big-to-small disk ratio, respectively (if applicable). Positive relative velocities signify repulsion.

Shape	Regular system Relative velocity [µm s^{-1}]	Rotated system Relative velocity [µm s^{-1}]
Disk, 1.0H	-0.90	4.70
Dimer, 0.5H, R1.50	-3.02	3.24
Dimer, 1.0H, R1.50	-2.04	4.78

the system: simply reversing the flow (outlet to inlet) would only prove time-reversibility, instead of showing that the light-beam is the source of the thickness discrepancy.

As table 4.3 shows, for all shapes, the attraction has vanished and turned into a repulsion for the rotated system, pointing towards the fact that the light beam is indeed not uniformly hitting the sample. Unfortunately, the relative velocities are not exactly flipped in sign; If the discrepancy in particle thickness was the sole reason for the relative velocity, one would expect equal but opposing velocities for a rotated system (of non-interacting pairs), as indicated by the previously shown figure 4.5b. Small deviations are expected as the exact starting position of the pair can never be reproduced once the channel is physically flipped, but that effect is not large enough to explain this data.

One possible explanation is that a skewed beam not only affects the particle thickness, but also slightly deforms it: in this case, the effect would be a combination of the intra-pair thickness discrepancy - which has a linear effect on the relative velocity - and a form-factor that is not necessarily linear. Further investigation would be needed to fully explain the observed relative velocity and remove it from the set-up. Nevertheless, the discoveries here are sufficient to explain a consistent bias towards attraction in the results further on.

4.4. Shape-dependent thickness variations

Raw data for the measurements and graphs contained in this section can be viewed in appendix D.

To measure the thickness of our particles, we create a pair of rods and flip them over. The original height of the particle is now in-plane with the microscope, and can therefore be measured. This thickness is taken to be constant for certain settings (light intensity, focal point, exposure time, etc.) and independent of particle shape. This is supported by Dendukuri's model [7], in which the area or perimeter of the particle does not play a role in its thickness.

Nevertheless, suspicion arose during experiments that the particle projection size - that is, the in-plane shape and size of the particle as it is produced and viewed - was also a factor in the thickness of the particle. Since regular particles are not thin enough to be toppled inside the channel, their thickness cannot be as easily determined as for thin rods. A first attempt therefore involved the removal of particles contained in the outlet to a droplet of fluid on a glass slide, in which they can freely rotate. Unfortunately, particles sedimented onto the glass slide fairly quickly, which meant only a few measurements were taken. These measurements did indicate significantly thicker disks and dumbbells than their respective rods.

A second attempt involved measuring five repetitions of pairwise rods, and with identical settings and position, producing five pairs of disks which are flipped within the channel outlet; By removing the outlet-tip, we obtain a fairly good contrast within the outlet of the channel, which allows all particles to freely rotate since it is no longer a Hele-Shaw geometry. The results of this second test are shown in figure 4.7, along with an example of a flipping disk.

The graph clearly shows that disks are on average 8 µm thicker than rods produced with identical settings, which is equal to a boost in confinement of approximately 10%. The only relevant difference between these experiments was the size and shape of the particle projection: the rods were relatively thin with a width of $W \approx 34\,\mu m$, compared to the large disk diameter of $D_{disk} \approx 195\,\mu m$. A possible explanation for this phenomenon lies in realising that Dendukuri's [7] 1D-model relies on oxygen diffusion only being relevant along the height of the channel: this assumption leads to the formulation of

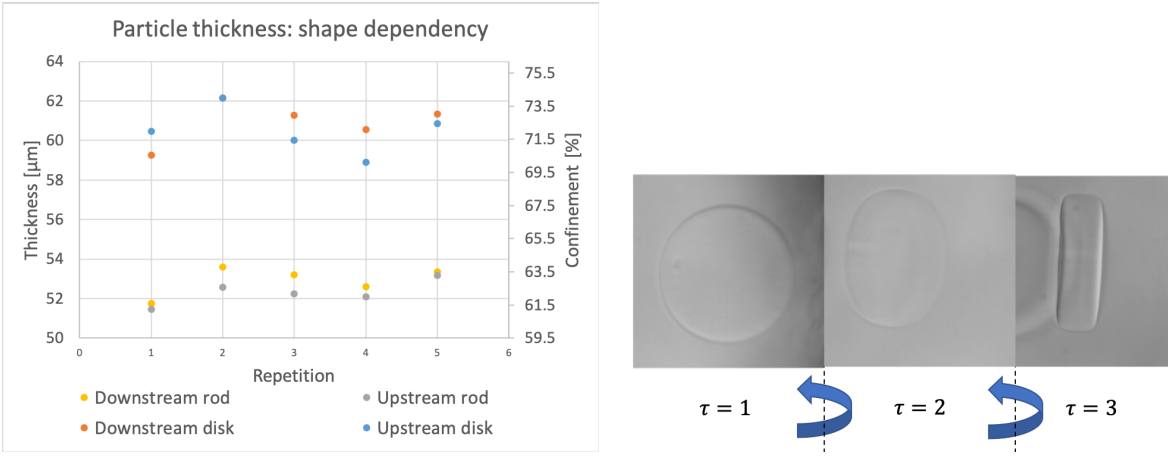

Figure 4.7: By flipping disks in the outlet (shown on the right), the thickness of five pairs of disks was measured and compared to five pairs of rods made with identical settings and position. This comparison is shown in the left-hand graph. Confinement is based on a channel height of H =84 µm. For both disks and rods, it can be seen that the upstream particle is always the thinner one, which agrees with the previously posited theory of a non-uniform light source. Average thickness and standard deviation is δ_{rod} = 52.6 ± 0.7 µm and δ_{disk} = 60.7 ± 1.0 µm, for rods and disks respectively. Disk diameter and rod thickness are given by D_{disk} ≈195 µm and W_{rod} ≈34 µm, respectively.

the 1D-model.

To recap from section 3.2.2, the presence of oxygen inhibits the particle propagation reaction, and thus limits the growth of the particle. While Dendukuri's model is based on oxygen diffusing in along the height, we hypothesise that for certain particle sizes, oxygen diffusion from the sides becomes significantly important in inhibiting the reaction. A useful analysis in this case is a comparison of the penetration depth of oxygen to the particle sizes. The penetration depth of oxygen in PEG-DA can be approximated to be:

$$\delta_p = \sqrt{\pi D_O t_{exp}} = 7.3\,\mu\text{m} \tag{4.2}$$

with δ_p the penetration depth in [m], D_O the diffusivity of oxygen in PEG-DA in [m^2 s^{-1}] and t_{exp} the exposure time in [s]. This equation is a valid approximation for flat geometries and 1-dimensional diffusion. For a rod of $W \approx 34$ µm, it is immediately apparent that oxygen diffusion from the sides cannot be ignored, as it penetrates into more than 40% of the particle. Similarly, a disk of diameter $D_{disk} \approx 195$ µm is expected to be affected much less significantly as oxygen penetrates into a much smaller portion of the disk.

To summarise, we hypothesise that very thin or slender objects are inhibited significantly in their particle growth due to oxygen diffusing in from the sides, while particles of increasing size are decreasingly affected by this phenomenon and thus become thicker. To further test this hypothesis, we replaced the mask holder by a diaphragm. With this diaphragm we can easily create octagonal particles of increasing size. As with the previously shown disks, these octagons are flipped in the outlet to measure their thickness, which is expected to increase with particle size. The results are shown in figure 4.8.

It is clear from the figure that particle thickness indeed increases with particle size for the octagons. The rod also stands out in how small it is: it does not seem to follow the seemingly linear trend of the octagons. Since oxygen diffusion is dependent on the exact shape of the particle, the rod is likely to experience a significantly different oxygen flux when compared to an octagon. In fact, it is likely that different geometries (rods, disks, tripods, etc.) all have a unique size versus thickness curve. Regardless of geometry, it is expected that as the projection size of the particles tends to infinity, the thickness becomes constant as the oxygen penetration depth becomes insignificant next to the projection size.

Proving that particle projection size factors into the thickness of said particle, has two major implications for this work: first, using rods as a measuring tool for particle thickness is no longer valid. This solves a previous problem in which particles got stuck often for 'seemingly thin particles', while they were in fact at least 10% more confined than initially presumed.

Secondly, results of different shapes can no longer be compared 1-on-1 with each other, since a difference in particle shape will also mean a difference in thickness. Any conclusions drawn from such comparisons can therefore not only be attributed to the shape dependence, but also to a difference

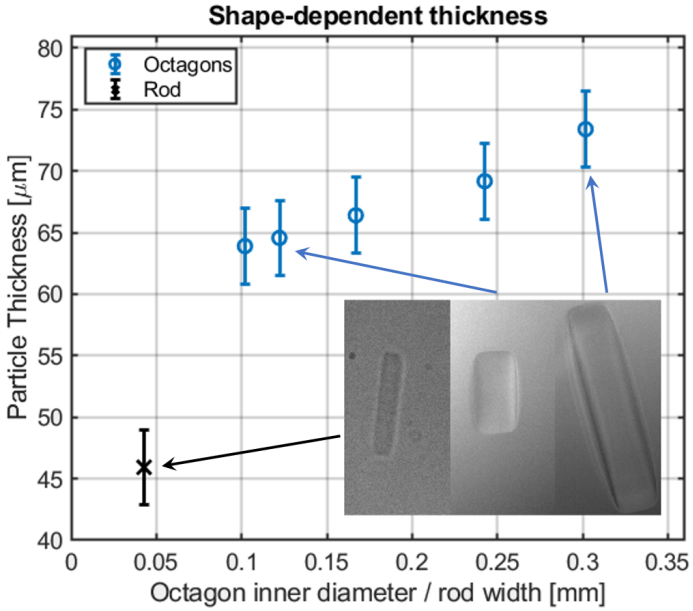

Figure 4.8: Particle thickness in [µm] plotted versus particle size in [mm]. For the octagons, the particle size is based on the inner diameter (a circle bounded by the octagon). The images in the bottom-right corner show examples of the flipped particles. All images are on the same scale, and the scale bar represents 100 µm. All particles were synthesised using identical production settings and in the same position of the channel. Error bars indicate 5 pixels of uncertainty on both sides while measuring.

in confinement. For the results following this section, the emphasis will therefore lie on the behaviour of a certain shape at different separation distances, and will not be compared to other shapes in a quantitative manner.

4.5. Pairwise interactions

Pairwise interactions have been measured for a selection of different shapes, ratios and angles. For the dimers (dumbbells) a series has been captured over different ratios, where the ratio is defined as $\kappa = R_1/R_2$, where R_1 and R_2 are the radii of the big and small disk, respectively. For trimers (tripods), a similar ratio series has been made, as well as a series over different leg-angles. As mentioned before, when discussing these results, we should keep the following intermediate results in mind:

- Particle thickness is not equal among different shapes (section 4.4). Therefore, we cannot directly compare the graphs of different shapes.
- The upstream particle is always thinner, causing an attractive (negative) relative velocity even for non-interacting pairs (section 4.3).
- The exact confinement of the particles is unknown, due to their dependency on shape (section 4.4). The expected behaviour of the particles is dependent on their confinement [9] and this might cause discrepancies between the simulations and the results.

For easy comparison between experimental and simulation results, the figures containing the simulation results will be repeated in each section.

4.5.1. Dimer ratio series

Raw data for the measurements and graphs contained in this section can be viewed in appendix E.

As mentioned in section 2.3.2, the dimer ratio series is characterised by a repulsion peak at small separations ($0 < \Delta x/H < 1$), which transitions into a weak attractive well around $2 < \Delta x/H < 6$. The interactions are at their strongest for a ratio of $\kappa = 2.00$, and decrease as the ratio drifts away from this value.

Figure 4.10 shows the experimental results for pairwise dimers. It is immediately clear that for all separations, the dimers are attracting: at no point does the relative velocity become positive. This was an expected outcome due to the discussion on thinner upstream particles. Looking at the general trend of each graph is more insightful: with no exception, each pair increasingly attracts with larger separation distances up to and including $\Delta x = 2.0H$. Only the last data point at $\Delta x = 4.0H$ differs from graph to graph. Physically, this can be easily explained; Each pair starts at peak repulsion at $\Delta x = 0.5H$, which transitions into an attraction at $\Delta x = 2.0H$. Therefore, the particles will speed up toward one another, as they start experiencing less and less repulsion, and eventually even attraction.

For $\Delta x = 4.0H$, this is not the case: this data point is on the opposite side of the attraction well (when compared to $\Delta x = 2.0H$). Based on simulations, one would therefore expect the attraction to slightly die out (yielding a slower attraction), or to stay roughly the same, depending on the exact ratio. While ratios κ =1.50, 2.00, 2.50 indeed adhere to this expectation, κ =1.30 is clearly the odd one out with a significantly stronger attraction for the latest data point.

4.5.2. Trimer ratio series

Raw data for the measurements and graphs contained in this section can be viewed in appendix F.

The trimer ratio series differs from its dimer counterpart in multiple ways: the repulsion effect at small separations is almost ten times stronger than for the dimers and the location of its peak shifts with ratio. The attractive well only exists for certain ratios. A last important difference is that for any tripod, we expect the interactions to have died out for $\Delta x = 4.0H$.

Figure 4.12 shows the experimental results for trimers with varying ratio. The increased strength of the repulsion peak is immediately noticed. Except for the weakest tripod (κ = 2.50), all tripods exhibit less attraction initially when compared to the dimers. A downwards trend is again observed: for increasing separation distance, attractive forces increase for all tripods. This disagrees with the simulations on multiple points. First of all, for all tripods, we expect the measured velocity to be roughly the same from $\Delta x = 2.0H$ onwards. Apart from that, for κ = 2.00 and 2.50, the highest relative velocity should occur at $\Delta x = 1.0H$, which is clearly not the case in the experimental results.

Looking more globally, we notice that for all tripods, the interactions do seem to die out, albeit on a much larger length scale than initially presumed, based on simulations. While the last observation points towards a possible flaw in length scales in the simulations, a more likely explanation can be found in confinement issues. As mentioned before, the exact confinement of these particles is unknown, due to the shape-dependence of particle thickness. For relatively thin particles ($\beta < 70\%$), the repulsion peak is both flattened and shifted towards attractive potentials.

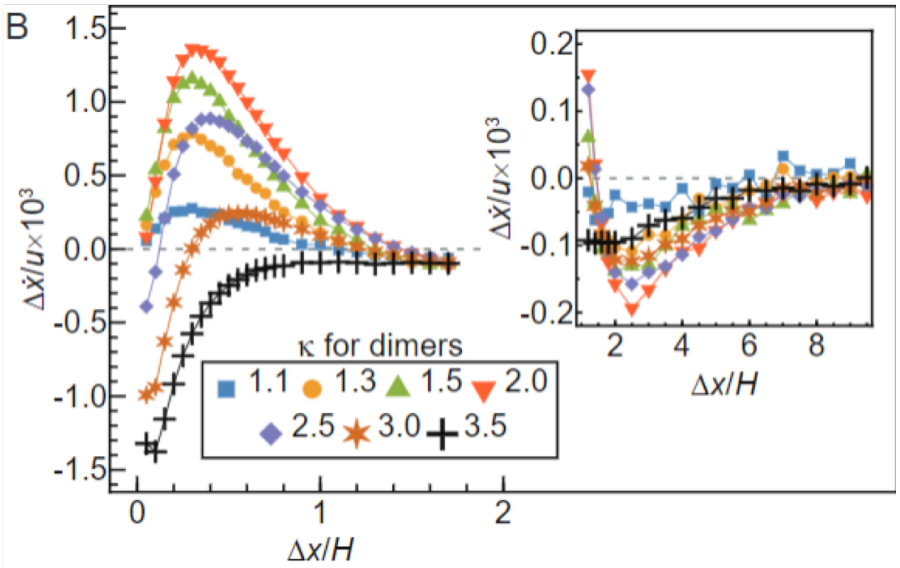

Figure 4.9: Dimer simulations along κ, where $\kappa = R_1/R_2$ with R_1 and R_2 the radius of the big and small disk, respectively. $\Delta\dot{x}/u$ signifies the relative velocity between the pair, with a net positive value signifying repulsion, and a negative value signifying attraction. Relative velocity has been scaled with the background (ambient) velocity u

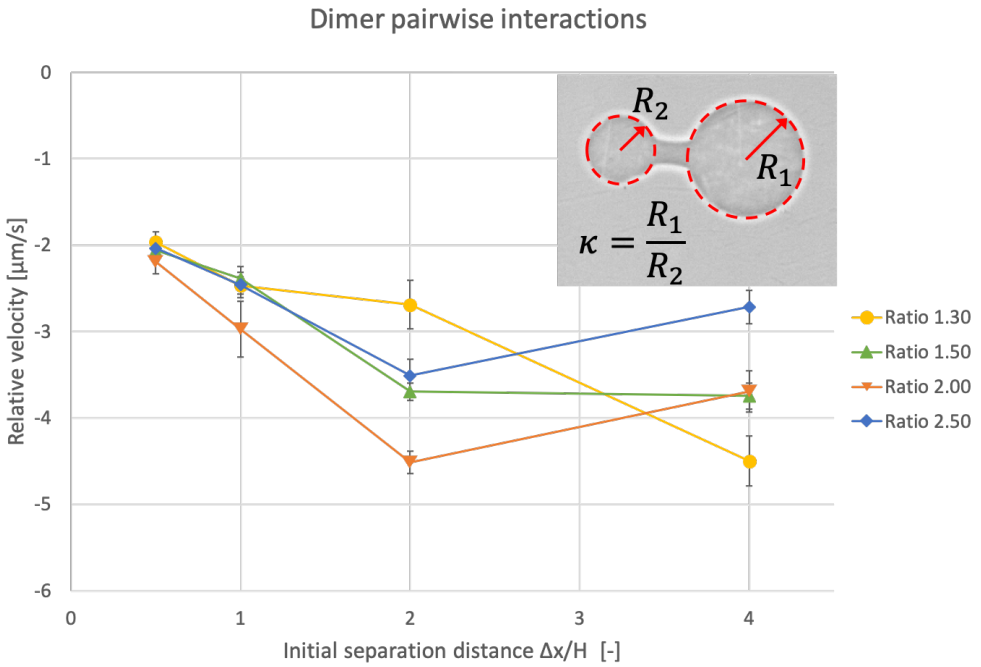

Figure 4.10: Experimental results on dimers over different ratios κ, where $\kappa = R_1/R_2$ with R_1 and R_2 the big and small disk radius, respectively. The vertical axis lists the averaged relative velocity in [µm s^{-1}] for a certain initial separation. For all data points, between ten and fifteen repetitions were averaged and the error bars indicate the standard deviation of these measurements.

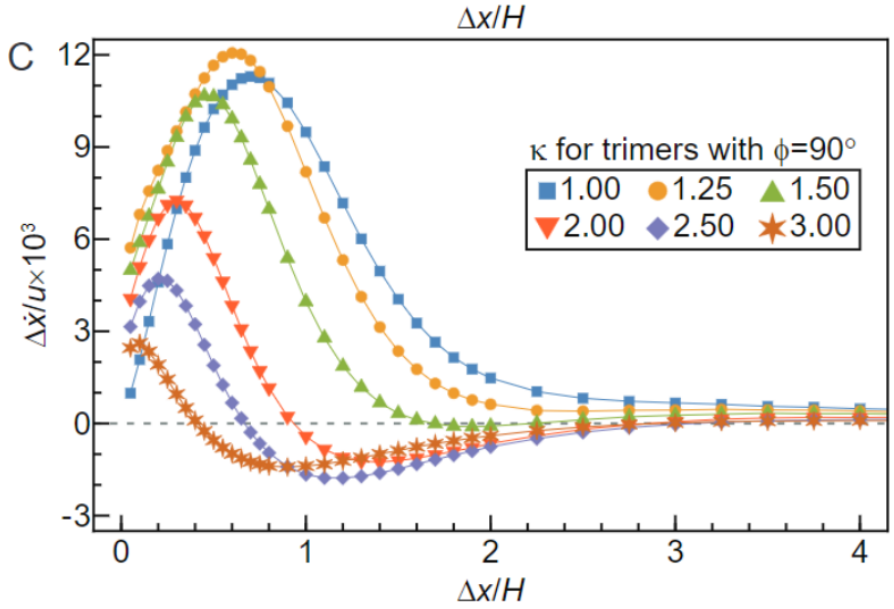

Figure 4.11: Trimer simulations along κ, where $\kappa = R_1/R_2$ with R_1 and R_2 the radius of the big and small disks, respectively. $\Delta\dot{x}/u$ signifies the relative velocity between the pair, with a net positive value signifying repulsion, and a negative value signifying attraction. Relative velocity has been scaled with the background (ambient) velocity u

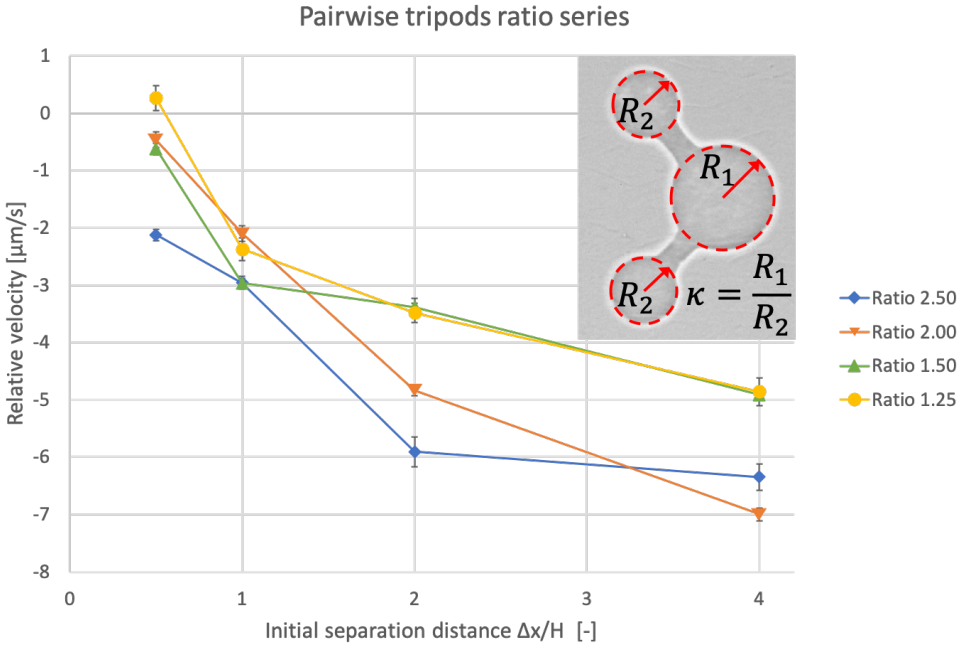

Figure 4.12: Experimental results on trimers over different ratios κ, where $\kappa = R_1/R_2$ with R_1 and R_2 the big and small disk radius, respectively. The vertical axis lists the averaged relative velocity in [µm s^{-1}] for a certain initial separation. For all data points, between ten and fifteen repetitions were averaged and the error bars indicate the standard deviation of these measurements.

4.5.3. Trimer angle series

Raw data for the measurements and graphs contained in this section can be viewed in appendix G.

The angle series is very similar to the kappa series for tripods: depending on the ratio, an attractive well might exist, and all interactions should basically have died out from $\Delta x = 2.0H$ onwards. One notable exception is the ϕ =165° set, which is almost independent of separation distance. Figure 4.14 shows the experimental results for the angle series.

The same downwards trend is noticed as before, which carries on over the entire range of separation distances. At the initial separation distance of $\Delta x = 0.5H$ high repulsion effects are noticed, which agrees with the simulations. Similar to the tripod kappa series. Interactions do seem to die out near the end of the graph, but not convincingly so. The graph for $\phi = 165°$ is especially interesting, as it disagrees sharply with the simulations: instead of barely changing with the separation distance, we actually see a significant change in relative velocity happening. Assuming the simulations are correct, this tells us that what we are actually measuring is a different physical effect, in addition to the possible interactions

4.5.4. Overall discussion

Overall, it is clear that the shape and geometry of a particle affects the interactions felt by said particle. Even though particle confinement is unknown amongst the different series, the dimer series differs from both tripod series in many ways; At small separation distances (which correspond to peak repulsion) we notice a clear difference in magnitude of the relative velocity. The same holds for the range of relative velocities: while all dimer interactions happen within a span of 2.5 µm s^{-1}, both tripods series operate on a span of 8.0 µm s^{-1}. Physically this makes sense, as the tripods show much greater interaction potentials than the dimers, and are therefore expected to have larger differences in relative velocity.

The large (difference in) interaction potentials for the tripods is observed when looking solely at the first data point for each shape: for both the angle and ratio series, the order of the shapes qualitatively agrees with the simulations. That is to say, the order of the shapes in terms of their interaction potential at $\Delta x = 0.5H$ is identical to their order in terms of relative velocity at this point.

While the dimer data agrees reasonably well with the simulations, this can not be said for either of the trimer series. While it is possible that the simulations for the tripods are incorrect, an alternative explanation can be offered based on the previously shown flaws in the set-up. If the UV-light hitting the sample is indeed non-uniform, then this could increasingly deform particles as separation distances increase on the mask. This deformation would then manifest as a relative velocity which varies with the initial separation. The already proven intra-pair particle thickness discrepancy could also be dependent on how far apart the two particles are on the mask, which even further obscures the real interactions from the measured data.

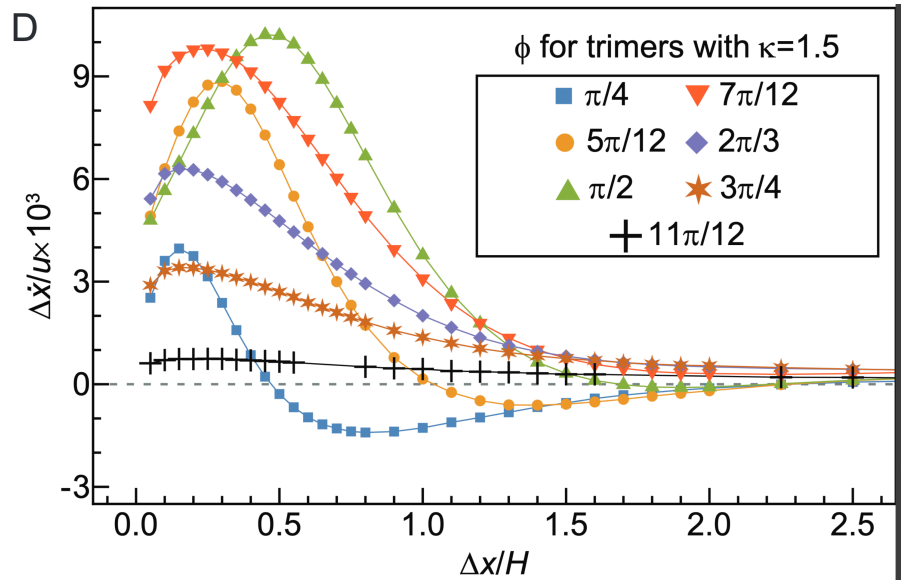

Figure 4.13: Trimer simulations along ϕ, where ϕ is the angle between the legs of the tripod. $\frac{\Delta \dot{x}}{u}$ signifies the relative velocity between the pair, with a net positive value signifying repulsion, and a negative value signifying attraction. Relative velocity has been scaled with the background (ambient) velocity u

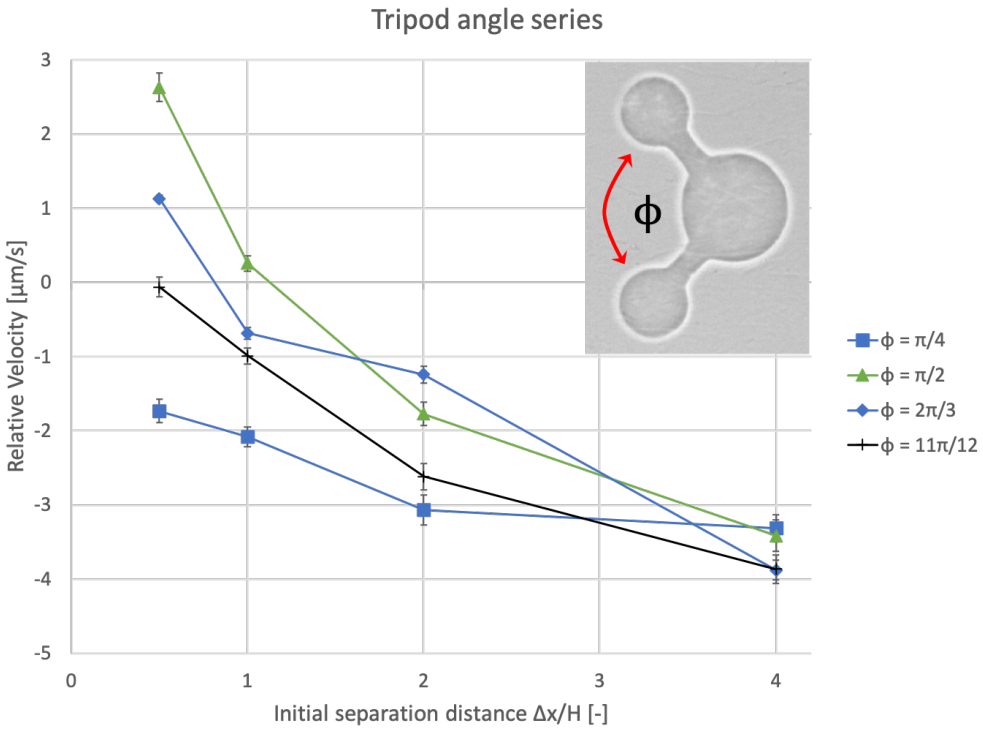

Figure 4.14: Experimental results on trimers over different leg angles ϕ. The vertical axis lists the averaged relative velocity in [$\mu m\, s^{-1}$] for a certain initial separation. For all data points, between ten and fifteen repetitions were averaged and the error bars indicate the standard deviation of these measurements.

5

Conclusion and recommendations

Two main goals were formulated in the beginning of this thesis: first, to create a suitably precise and accurate experimental set-up for hydrodynamic experiments on the micro-scale. The second goal was to make use of this set-up to investigate pairwise particle interactions and show their dependence on shape.

Numerous improvements were made to the set-up, that increased the precision and reproducibility of experiments. The most important improvement was the technique with which a pair of particles was produced: by combining two particles on one mask, the variation in particle thickness within the pair was greatly reduced, improving the reproducibility of results by a factor 30. One remaining flaw was identified within the optical path of UV-light leading to the sample. Strong evidence was presented to indicate that the UV-light hitting the sample is not uniformly distributed, resulting in a bias towards thinner upstream particles. Physical rotation of the channel de-coupled time-reversibility from this problem, and ruled out channel tapering as the possible cause. Unfortunately, the flaw was not resolved due to (amongst others) time constraints.

On the subject of particle thickness, we gained novel insight into the applicability of the current stop-flow lithography particle growth model, as proposed by Dendukuri et al. in 2008. It has been shown that this 1D-model is insufficient when analysing particles of different size and shape. Experimentally, it was demonstrated that particle thickness increases with the projection size of the particle, despite an otherwise identical set-up. It was hypothesised that for larger particles, oxygen diffusing in from the sides of particles - in contrast to only diffusion from the top and bottom, as the model suggests - becomes less significant, while for smaller particles, oxygen can still fully penetrate into the reaction zone. Therefore, as particles increase in size, they experience less oxygen inhibition, allowing them to grow into a thicker particle.

Investigations into pairwise particles interactions yielded ambiguous results: a dependence on shape was shown, especially when comparing the magnitude of interactions measured. Yet, the experimental data only qualitatively agreed with some of the simulation aspects. Notably, the difference in magnitude of the interaction potential was experimentally observed for all tripod shapes. The disagreement between simulations and experimental data finds its possible cause in the previously discussed non-uniformity of the UV-light beam. Apart from creating a discrepancy in particle thickness, it might also slightly deform the particles. What is more important, is that this effect might vary with the distance between particles on the mask (which determines the separation distance). As such, a non-constant error is introduced into the measurements, obscuring the actual interactions from view.

5.1. Recommendations

In light of our observations and conclusions drawn, we can formulate a few recommendations and improvements:

- The non-uniformity of the UV-light beam influences all obtained results, in an unclear and inconsistent way. Dedicating time and effort into creating a uniform light source that hits the sample exactly perpendicular is well worth the effort. Experiments can be done measuring the variation in particle thickness with separation distance to provide more convincing proof that the UV-light beam is indeed the culprit.
- The 1D-model of Dendukuri et al. (2008) can be expanded to become more general. This work showed that as of yet, an unmodelled dependency on particle projection size exists, but hypothesises that this dependency is only valid for relatively slender or thin objects. Determining at what point(s) projection size is no longer a factor, would provide proper boundaries for the validity of the model. Apart from that, corrections can be formulated for varying shapes while operating outside of these boundaries.
- In line with the previous recommendation which deals with the theory of particle propagation, it might be worthwhile to develop channels that possess a screw-like geometry at the end. For example, rotating the entire Hele-Shaw cell by 90° towards the outlet, allows one to easily measure the thickness of any and all particles, as produced within the channel immediately. In this way, one no longer relies on theory or assumptions to indirectly measure particle thickness, but can obtain the measurement directly.
- Pairwise interactions were measured for a small selection of shapes, this selection can be expanded to also include asymmetrical particles (e.g. a tripod in which all disk sizes are different) or different 'base' shapes such as triangles instead of disks.
- The results of these particle pair interactions can serve as a base case to continue research into other hydrodynamic aspects on this scale, such as the effect of elasticity on these interactions.
- Knowledge on pairwise interactions could be applied to the 'self-ordering' of particles, which might be of interest when trying to increase crystallisation rates.

A

Experimental Protocols

In this appendix, various protocols can be found that were used to standardise most of the lab work. This was done in order to minimise the human error in any results due to inconsistent preparations. In any of these protocols, it is assumed that all used containers, instruments or other materials that come in contact with the mixture have been cleaned thoroughly. For some instances, it is mentioned explicitly in the protocol if the cleaning is particularly important in that step. Also, for most steps, it is assumed that the work is carried out in a suitable environment (e.g. a laminar flow hood) that protects the prepared samples from contamination by the environment.

The protocol for microfluidic device preparation can be found in section A.1, followed by the protocol for mixing the PEGDA solution in section A.2. Section A.3 shows a general procedure for setting-up a proper experiment, with as non-deformed particles as possible.

A.1. Protocol for microfluidic device preparation

This protocol was used for the preparation of microfluidic devices. This protocol is an adaptation (by the author of this thesis) of an earlier version, obtained from supervisors.

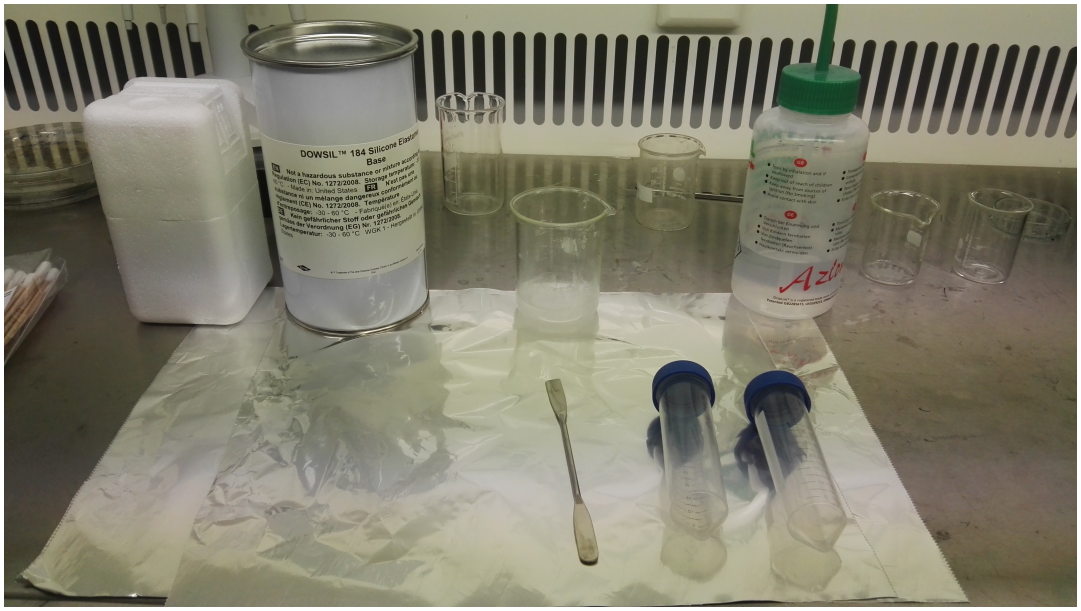

Figure A.1: Cleaned working surface with the necessary materials for preparing a PDMS mixture. From left to right: DOWSIL™ 184 Silicon Elastomer Kit (Curing agent and Base), waste beaker, cleaned spatula, two cleaned 50 ml tubes (suitable for centrifuging). Also needed but not shown: pipet capable of handling 1 ml to 5 ml and corresponding tips.

A.1.1. Preparation of PDMS mixture

- Prepare a clean work surface containing the materials and equipment as shown in figure A.1.
- Pour 50 g of PDMS base from the container into a clean Cornell 50 ml tube.
- Using a pipet, add 5 g of curing agent to the PDMS base. If other quantities are desired, make sure the 1:10 ratio of curing agent to PDMS base is maintained, as instructed by the manufacturer.
- Use a cleaned spatula to thoroughly mix the curing agent with the PDMS base. Make sure to scrape down the sides to ensure mixing of outer layers.
- When the mixture becomes turbid due to mixed in air bubbles along the entire length of the tube (shown in figure A.2), continue mixing for one more minute to ensure proper mixing.
- Centrifuge mixture at 7400 rpm for 15 min to force dust to the bottom of the tube.

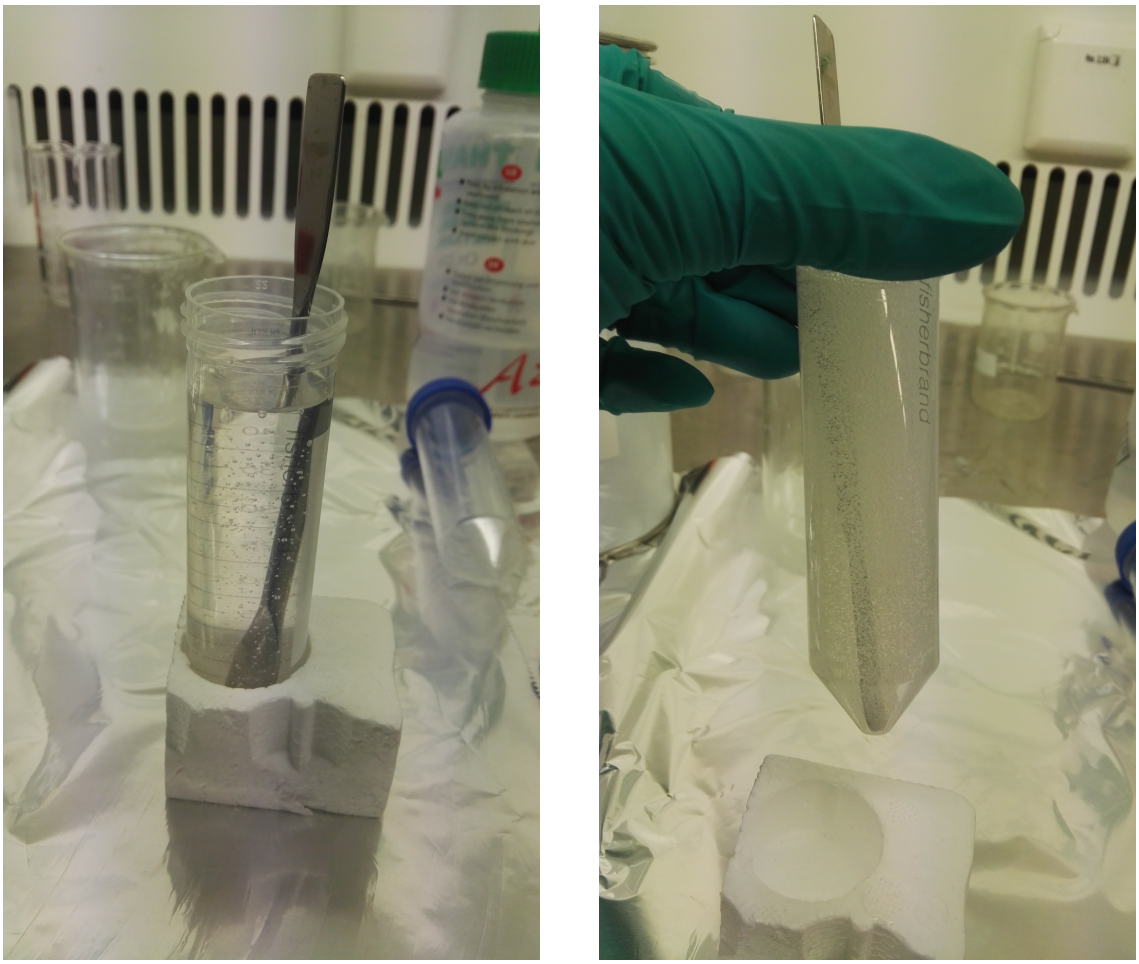

Figure A.2: The left image shows the unmixed solution. Mix rigorously until the mixture resembles the right image in terms of turbidity, then continue for one more minute to ensure complete mixing.

A.1.2. Prepare PDMS mould

- Clean the mould thoroughly with methanol, water and methanol again, then dry the mould using pressurised nitrogen or air.
- Place the mould inside a large enough petri dish and pour the previously prepared PDMS mixture into the petri dish. Pour slowly to avoid air bubbles and make sure that the PDMS layer is at least 5 mm higher than the mould. Always pour from the same corner, and slightly tilt the petri dish away from this corner: this way, any contamination in the mixture will gather in the same spot.

- Gently place the petri dish inside a vacuum chamber; keep the petri dish level at all times to minimise spillage and possible contamination of the PDMS.
- Pump air out of the vacuum chamber to attain an absolute pressure of at maximum 100 mbar. Let rest for at least thirty minutes to degas the PDMS layer.
- Slowly bring vacuum chamber back to atmospheric pressure and remove the petri dish from the vacuum chamber into an oven at 65 °C and let sit overnight to ensure complete curing.
- Remove the petri dish from the oven and **immediately** cut the cured PDMS a little wide around the edges of the mould using a clean scalpel then gently lift the mould, encased in PDMS, out of the petri dish as shown in figure A.3.
- Cut/peel the thin layer of PDMS from the backside of the mould. When free of PDMS, gently remove the mould from the remaining PDMS block (figure A.4). **Do not** use any spatula's or other tools to act as lever between the mould and the PDMS, as this might damage the channels. Place the PDMS block containing the channels into a clean petri dish and cover it. At all times, make sure that the channel side is facing upwards, so it cannot be contaminated by the petri dish or any other surface it rests upon.

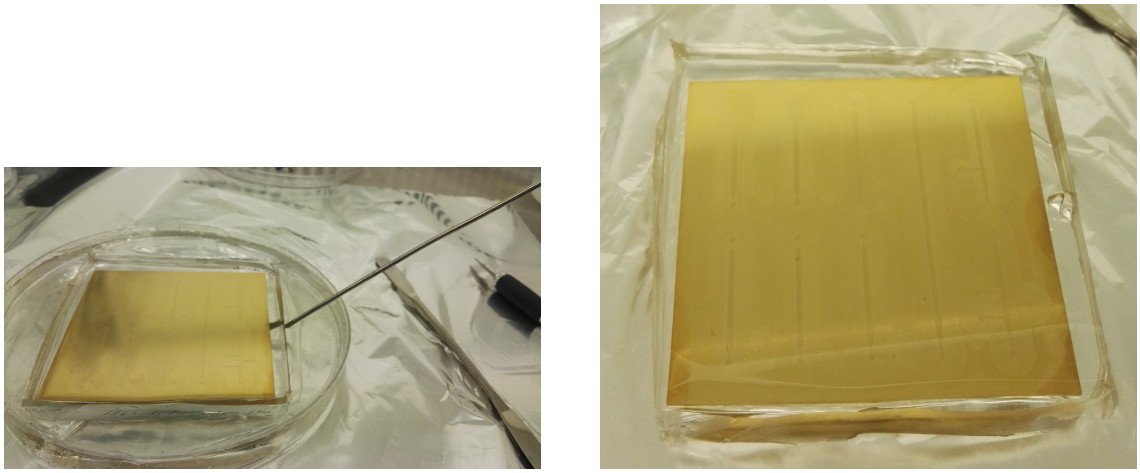

Figure A.3: The left image shows the cut PDMS block being levered out of the petri dish. Do so gently, to avoid damage to the channels. The right image shows the levered out PDMS block.

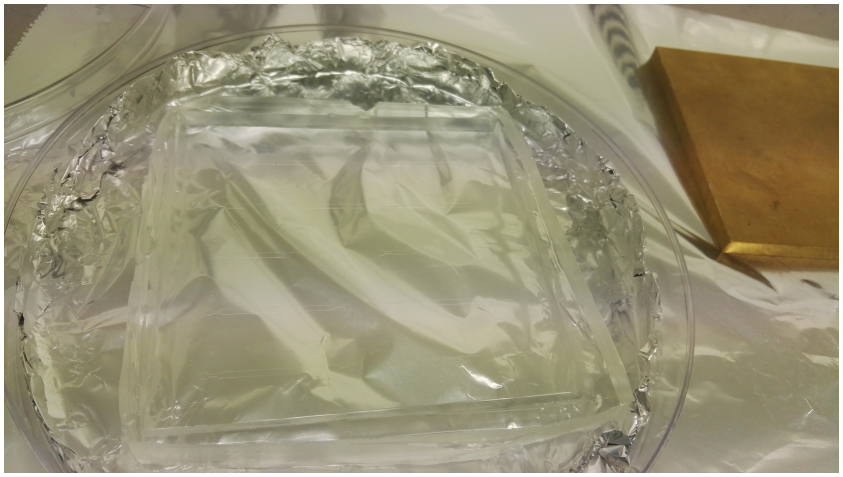

Figure A.4: The mould (seen on the right) has been removed from the PDMS block (left). The PDMS block faintly shows the channels that have been indented in it by the mould.

A.1.3. Cut individual channels

- Make sure that all channels are still facing upwards.
- Using a clean scalpel, cut into the PDMS block in the middle between two channels. Keep as much space around the in- and outlets as possible, to prevent rupturing further on in the process. In this fashion, cut a rectangular PDMS device out of the entire PDMS block, as shown in figure A.5. Cut as closely through the entire PDMS layer as possible.
- Gently liberate the individual device from the larger PDMS block; refrain from touching the top part of the devices to avoid contamination or damaging of the channels. Instead, try to only hold the devices by their cut sides. After separation, immediately place the individual device into a cleaned petri dish and cover with the petri dish lid to avoid contamination or damaging.
- Repeat procedure for all other channels contained inside the large PDMS block, until all devices have been liberated.

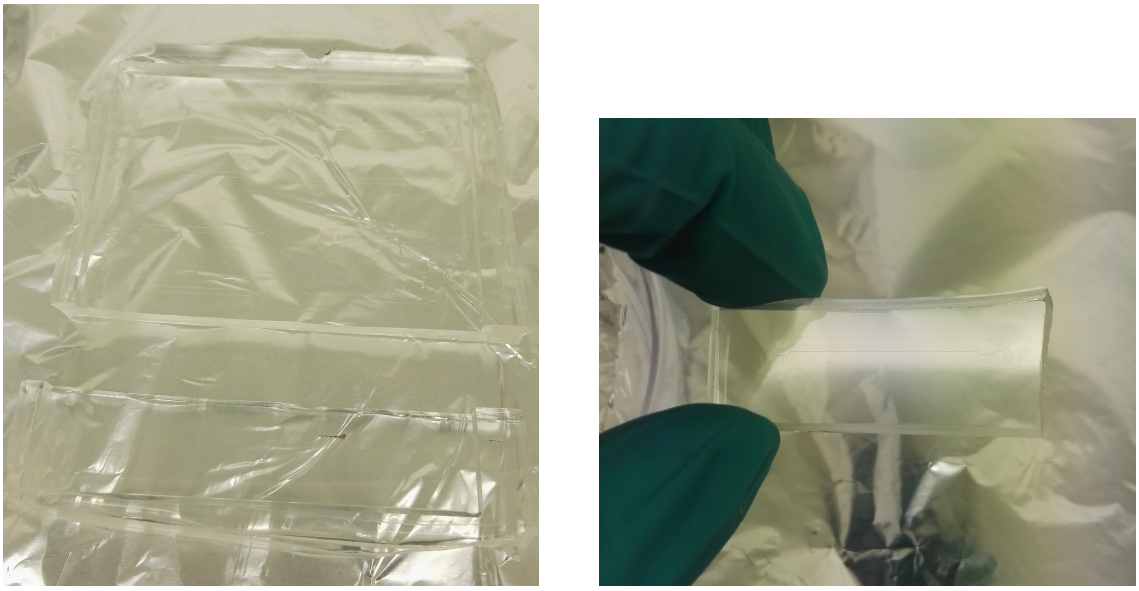

Figure A.5: First, cut strips (containing two channels) from the larger PDMS block, as shown in the left image. Then proceed to cut the individual devices from these strips as shown in the right image.

A.1.4. Punching in-/outlet ports

- Make sure that all channels are still facing upwards.
- Using a cleaned 15 gauge Nordson Optimum© General Purpose Tip (amber coloured tips), position the tip gently above the in-/outlet outline of a device.
- When confident about the precise positioning, apply a constant downwards pressure to punch a hole through the entire PDMS layer. Make sure at all times to keep the tip as vertical as possible, to avoid slanted or skewed ports. **Do not** remove the tip.
- Using an instrument with a smaller diameter than the tip (syringe needles are ideal), push the small cylinder of PDMS out of the tip, and dispose of it. Use pressurized air/nitrogen to remove any residual PDMS particles from the tip. This procedure is shown in figure A.6.
- Remove the tip from the device by pulling it back out. Make sure to only pull, **do not** twist, as the PDMS might rupture upon too much rotation.
- Repeat the procedure for any other ports (generally two per device), then use pressurised air or nitrogen to clean both ports and the channel itself. Immediately place the device back into the cleaned petri dish and cover it with the petri dish lid to avoid contamination or accidental damaging.

- Repeat the entire procedure for all other devices.
- At this point, clean and sonicate the devices in methanol to ensure that PDMS slivers or other contaminants have been washed from the channels. Afterwards, dry them and immediately return them to a clean petridish.

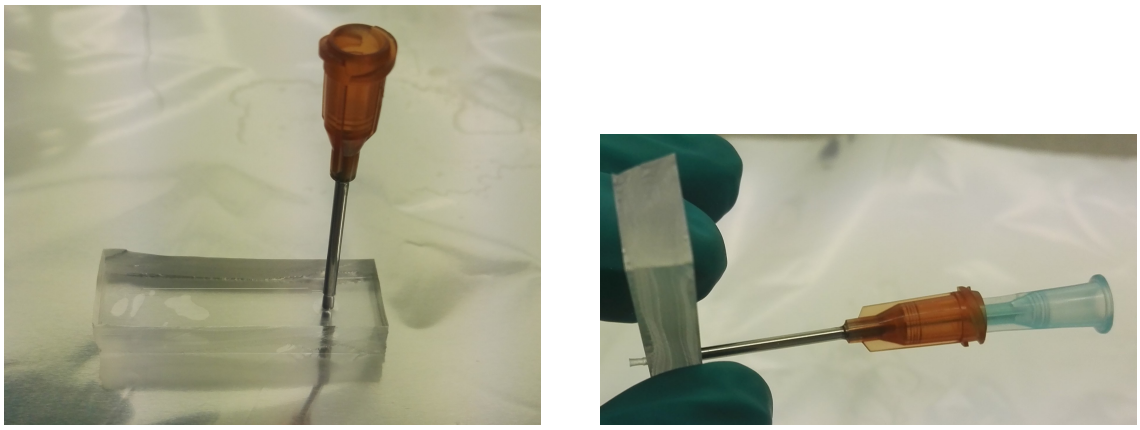

Figure A.6: With the channel facing up, apply pressure to punch the IO-port as shown in the left image. Make sure the tip has fully punctured the PDMS. Lift the device from the workbench, and use a syringe needle to push the PDMS cylinder through and remove it, as shown in the right image.

A.1.5. Preparing glass PDMS slides

- Prepare approximately 1 ml of PDMS mixture per microfluidic device, according to the procedure outlined in the beginning of this protocol, subsection A.1.1. **NOTE:** The times listed below were used for an 8:50 weight ratio of curing agent of PDMS instead. This procedure can be done with the original ratio, but times will then vary.
- Clean glass slides with methanol and water, and thoroughly dry off using pressurised air or nitrogen. Place the glass slides in a cleaned petri dish and cover them with petri dish lid to avoid contamination. Repeat this step until the desired number of glass slides have been cleaned.
- Place one glass slide into the spin coater and apply vacuum pump. Ensure that the glass slide is indeed suctioned to the spin coater axle.
- Fill a 1 ml syringe with 0.5 ml of the previously prepared PDMS mixture. Gently pour the contents of the syringe onto the middle of the glass slides along the length, avoiding the edges.
- Close the spin coater and spin coat for 1:09 minutes in total, at the settings shown in figure A.7.
- After completion of the spin coating program, remove the vacuum from the glass slide and gently place it in a petri dish lined with aluminium foil. Make sure that the glass slides are placed as level as possible, to prevent the PDMS from forming an uneven layer. Cover the petri dish with the petri dish lid. Repeat this procedure for as many glass slides as desired.
- Let all slides stand in the petri dish for approximately ten minutes.
- Place the petri dish with the glass slides into the oven at 65 °C for 35 min. This will semi-cure the PDMS layer on the glass slides, and so, timing is crucial. To check whether or not the PDMS is semi-cured to our desire, one can do the following test: place your finger on the glass slide (at the edge). This should leave a finger print, but the PDMS should no longer stick to your finger. No finger print: overcured. Very sticky: undercured.

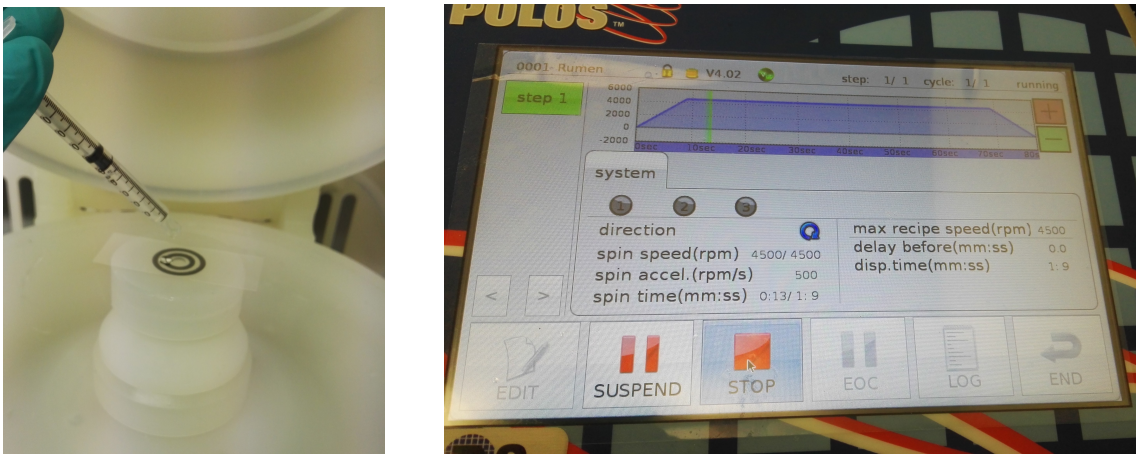

Figure A.7: The left image shows the application of 0.5 ml of PDMS onto the glass microscopy slide. A vacuum pump holds the glass slide in place on the spincoater. The right image shows the spincoater settings.

A.1.6. Attaching glass slide to PDMS device

- Immediately remove the petri dish from the oven to prevent over-curing of the PDMS layer; it should be semi-cured at this point.
- Very gently place a previously prepared PDMS device with the channel side facing **downwards** onto a glass slide, encasing the channel fully in PDMS. **Make sure not to press** the channel onto the glass slide as this might cause the channel to collapse onto the glass slide. When done properly, one should immediately observe lamination of the PDMS layers. Place the completed device into a clean petri dish and cover it with the petri dish lid to avoid contamination or accidental damaging.
- Repeat the above step for the desired number of devices.
- Place the petri dish(es) holding the completed devices into an oven at 65 °C overnight, to ensure complete curing of the microfluidic devices.

A.2. Protocol for mixing PEGDA solution

A.2.1. Prepare stock solution

- If the stock solutions are more than two weeks old, follow these steps to create new stock solutions.
- Take the desired PEG-DA and PI containers from the refrigerator.
- Take the appropriate vials (10 ml for the PEG-DA, 2 ml with brown glass for the PI) and clean them with methanol, water, then methanol again and dry them. Do not forget to also clean the caps in an identical fashion.
- Label the vials, wrap them in aluminium foil and label the foil.
- Check if the appropriate pipet is clean, if so, pipet 1.5 ml of PI into its designated vial. Screw the cap on immediately, and ensure that the entire vial is properly covered in aluminium foil. Do the same for the vendor solution.
- Depending on the average polymer weight of the PEG-DA, either scoop or pipet approximately 8 ml of PEG-DA into its designated vial. Immediately screw the cap on, and ensure that the entire vial is properly covered in aluminium foil. Do the same for the vendor solution.
- Return the vendor solutions to the refrigerator.

A.2.2. Prepare photoreactive solution

- Rinse a 1.5 ml Eppendorf tube with methanol, water, then methanol again and dry. Keep aluminium foil nearby so the tube can be wrapped quickly.
- Check if the appropriate pipet is clean and pipet 970 µl of PEG-DA into the Eppendorf tube. For solid PEG-DA (in case of high average polymer weight), warm up (with your hands) prior to pipetting.
- Pipet 30 µl of PI into the Eppendorf tube. Close the Eppendorf tube, and cover it with aluminium foil (do not wrap it yet). Close and re-wrap the PI stock solution with aluminium foil.
- Prepare a counter-weight for the Eppendorf tube and cover it with aluminium foil (do not wrap it yet). Cut of the thumb of a large nitrile glove, place the tube inside the cut-off thumb and use this to vortex the tube for ten minutes. Meanwhile, return the stock solutions to the refrigerator. Vortexing will properly mix the two reagents together.
- After vortexing, centrifuge the tube for ten minutes at 6000 RPM, using the previously prepared counterweight. This will sediment any dust or solids to the side walls or bottom. Cover the centrifuge with aluminium foil. It is advised to switch on all microscope-related equipment at this point to allow the UV-lamp to warm up.
- When done, remove the tube and wrap it in aluminium foil.

A.2.3. Loading solution

- Clean the two bent in-/outlet tips using methanol, water, then methanol again and dry.
- Attach a tip to a 1 ml syringe using some tubing.
- Place the tip into the Eppendorf tube. Make sure to avoid the walls and bottom of the tube, since dust will have sedimented there. Slowly draw solution into the tip, and fill the tip for approximately three quarters; do not draw liquid into the tubing, as this has not been cleaned.
- Carefully, without twisting, insert the tip into the inlet port. Make sure to insert it straight down and not at an angle. At the other end, insert the second tip in a similar fashion. Wrap the Eppendorf tube in aluminium foil.
- Attach some tubing to the outlet and remove the syringe and tubing from the inlet tip.
- Place the sample appropriately on the microscope stage and connect the pressure pump tubing to the inlet tip.
- Tape the in- and outlet tubing to the microscope stage to avoid dislodgement of the tips (due to the weight of the tubing).
- Cover the device with aluminium foil for now and clean up the laminar flow hood for other people to use.
- When ready to start experiments, kill the lights, remove aluminium foil, ensure that the tips are still properly attached and proceed with setting up the microscope in terms of lighting and diaphragm settings.

A.3. Particle creation: fine-tuning procedure

Once all preparatory work has been completed, as outlined in the previous appendices, it is time to perform experiments. Before any flow-behaviour can be observed, we need to make sure that our particles are formed as perfect as possible, and are not in any way deformed. This basically comes down to three settings: The light-beam intensity as determined by the neutral density filters, the exposure time, and the focal point. These three together will determine both the integrity of your particle (in terms of its shape) and the particle thickness. By following the procedure as outlined below, you will ensure that your settings are (at the very least) close to generating a proper particle.

A.3.1. Köhler illumination and other small preparations

- Place a chip on the microscope holder. You can use a (3D-printed) holder that allows you to rotate the device while underneath the microscope, if so mount the holder and place a device in it.

- Play with the focus until you can see the channel relatively clear (for the normal stage, you should start seeing shadows of the channel when above 2000 µm). While the channel is in sight, attach the tubing to the tips and rotate so that it appears straight. Confirm by moving the stage exclusively in the horizontal direction: the space on either side (top and bottom) of the channel should not in-/decrease if the channel is truly straightly placed on. Once it's straight on, try to tape down the tubing onto the microscope stage to keep the device in this position. It will slightly shift while doing this, so reposition one last time before taping the last tubing.

- Make sure that the glass slide is level with respect to the microscope stage: if one corner is higher up than the others, than it will be very hard to create proper particles and adequately track them, due to focal difficulties.

- (*this part of the procedure is also shown on the poster near the microscope*) Once confirmed, switch the microscope to the eyepieces and close the field diaphragm completely. Rotate both condensor knobs simultaneously until the octagon is focussed properly.

- Use the two diagonal screws to move the focussed octagon to the centre. Once there, open the field diaphragm to extend the edges of the octagon to be slightly out of view: you should no longer be able to see any of the octagon edges, and a clear image of the channel should be observed.

- Switch an eyepiece of your choice for the telescopic lens, and adjust its ring so that it produces a sharp image of an octagon. Adjust the aperture diaphragm (this is a different diaphragm than previously adjusted) until the octagon covers approximately 80% of the field of view. Switch it back to the original eyepiece, making sure that it clicks into place.

- Switch back to camera view and make sure that the channel is still level. The contrast on the channel can now be set in the LUT settings in the Nikon software.

A.3.2. Filling the channel and choosing an initial location

- If the channel hasn't filled on its own already, apply a small pressure ($\Delta P = 8\,\mathrm{mbar}$, is normally ok) and observe how it fills. The capillary fluid interface within the channel can indicate where certain defects are in the channel: for a completely smooth channel, the concave meniscus will stay smooth along the entire length while filling the channel. The moment it stumbles upon a defect, you can see the interface break and bend around it. In this way, you can already get a sense of where the suitable positions within your channel are.

- For an initial position, make sure that you are at least 1 full frame away from the inlet (or outlet for that matter) of the channel. Within this distance, temporal effects of the necks of the channel might still be felt. Taking that one frame into account, it is always advisable to start close the inlet. This way, you still have enough room to try again if a particle gets stuck soon.

- Once a position has been chosen, look at the angle of the channel: regardless of your efforts in the previous subsection, channels will almost never be perfectly straight. While horizontally moving the stage, see if the channel moves out of frame at the top or bottom. For the processing of the recordings, you always want your top wall in frame. Therefore, you can slightly shift your initial Y position to include more or less space on top, as required by the channel angle. Note that this causes the particles to be out of the centreline of the channel: if you need to shift too much, then scripting a camera shift after particle production might be preferable.

- Note down the X and Y positions of your chosen position into the script of your choice. Switch to the 20x objective, and manoeuvre towards the bottom wall (which is actually the side wall closest to you, not the floor of the channel). Focus accurately on the bottom of this side wall, and use this focal position as Z value in your script.

A.3.3. Determining rod thickness and focal point range

- Load up a (pair of) rod(s) in the mask holder. For a 3 vol% PI solution and 82 µm channel, use ND16, $t_{exp} = 0.50$ and $dZ = -15$ µm as initial settings. Open the shutter, produce your rod(s) and apply a pressure to let them flip. Once flipped, stop the flow and observe. Flipped, the rods should look rectangular. If their bottom/top walls are divergent/convergent (the rod is a trapezium) then the focal point (dZ) is off.

- For this production method, a range of approximately 20 µm exists for which rods will seem rectangular. If you produced a rectangular rod, you are within this range. If not, change your focal point and keep producing particles in one direction to find the boundary at which they start looking rectangular. follow the same procedure from the other side to find both boundaries. The middle of this range, is often near the ideal focal point.

- Once the centre of this range has been determined, produce a rod with these settings, flip them, and measure their thickness. Change the exposure time and/or filter to achieve the desired thickness. Note that the thickness of a rod **does not** equal the thickness of another shape produced with identical settings.

- Try to observe the following limits while achieving your desired thickness: exposure time should always be above $t_{exp} > 0.1$ s to avoid shutter inconsistencies. Apart from that, it is advised to keep it below 1 s because the fluid will never be completely at rest, which leads to particle 'smearing' for high exposure times.

A.3.4. Narrowing down the focal point

- To narrow down the focal point, we will now load a mask with a (pair of) disk(s). Starting at the middle of the previously determined range, produce a disk and look at their edges. The shadows around the disk should be equal in size along the entire disk if it is a uniformly produced disk. Therefore, slightly change the focal point (increments of 5 µm) to achieve this equal shadow.

- A further optimisation of the focal point can be done by analysing the flow behaviour, particularly of disks and dumbbells. When flowing one of these particles, slightly changing their focal point will sometimes cause them to rotate less, or more smoothly past any defects. Single dumbbells are ideal for this procedure, but one can also try to do this with disks.

- In the author's opinion, one can at best improve the focal point to be given by a 2.5 µm range. Any improvement past that point is unlikely, given the fact that we've passed well into the depth of field of the 20x objective. Be sure not to use the last technique (observing rotation) for too broad a range of focal points, as that might cause you to overcompensate (e.g. creating a skewed particle that flows smoothly past a defect, while it should in fact bump into it). If in doubt whether or not this improves your results or if it's simply inconclusive, stick to your original shadow-equalling focal point. You can always slightly adjust for flow behaviour once you start your experiments.

A.3.5. Resulting situation and starting experiments

- You've now attained a position in the channel for which everything is calibrated as well as possible. You know the rod thickness and focal point for this position, as well as the cleanliness of the path (since you've already observed quite a few particles.)

- Note that the focal point dZ is defined with respect to the original focal point Z. Therefore, when changing positions, if you redetermine Z, your focal point dZ should still hold, and you **do not** have to repeat the focal point experiment for each position you try. It is important to remember that you need to keep determining Z in a consistent manner, for example by always focussing on the bottom of the channel, for the lower side wall, as proposed by this protocol. Having said that, you can define Z in any way you like, so long as you do it consistently.

- You can now start your experiments by finding a position that has a long enough clean path for your intended purpose. Some last tips & tricks:

- Always note your old positions down, in case you'd want to return to a previous one.

- Be wary of shifting glass slides: if you suddenly get odd looking particles, check if your slide is still level, and both your in-/outlet still attached.
- Avoid particle production for a position that is hard to focus: you will never be able to produce a proper particle if you are trying to focus on a bent part of the channel (only relevant for thin glass slides).
- Save a test-run to the Nikon PC and process it directly. Having one testrun processed often allows you to judge the cleanliness of your path much more accurately than just 'eyeballing it'. One minute of work here can save you an entire day of uesless, failed experiments.

B

Particle masks

This appendix shows all masks that were available for the pairwise particle production. More masks (of single particles) were available, but were not included in this appendix as they were not used for any of the experiments.

The masks will start on the next page and the rest of this page was intentionally left blank.

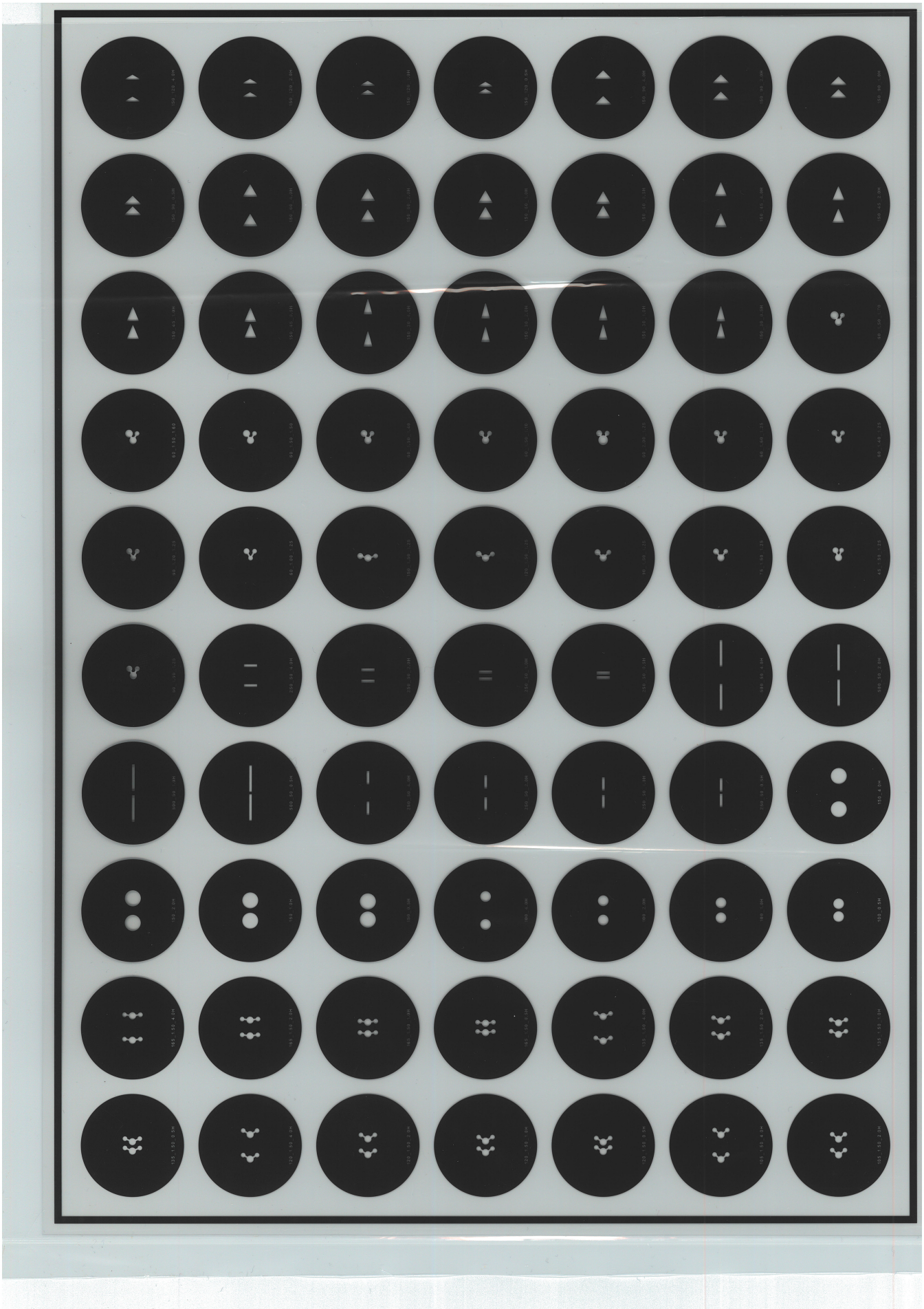

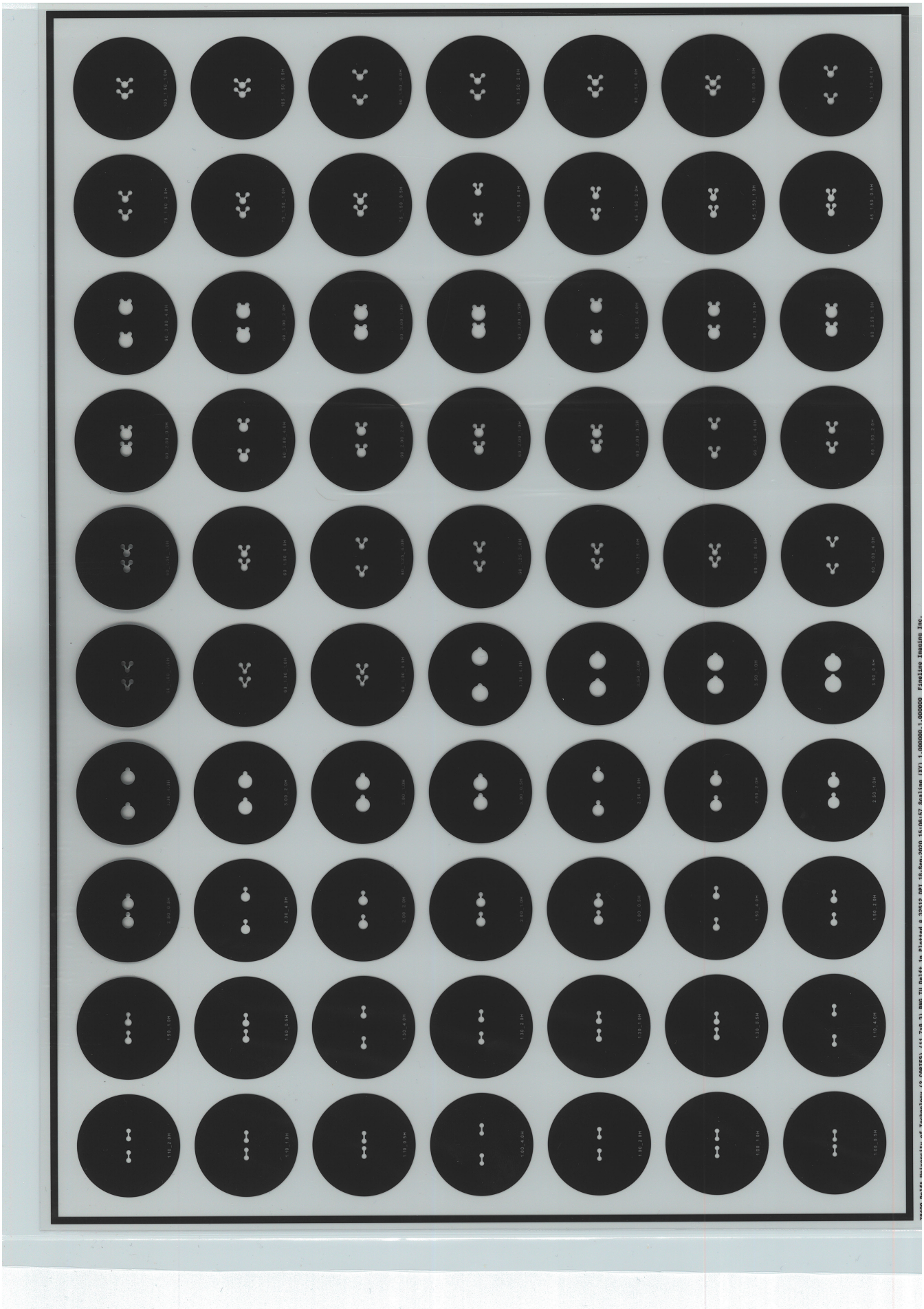

C

Raw data: Time-reversibility and non-uniform light beam

This appendix contains the raw data for section 4.3.

C.1. Intra-pair particle thickness comparison

Table C.1: Raw data for the intra-pair thickness comparison. Data was originally captured to see if particles relax and change size if left idle for a certain amount of time, hence the 'Idle time' column. This column of data has not been used in the main body of this thesis. 'down' and 'up' represent the downstream and upstream particle, respectively. All thicknesses have been measured in [µm].

	Repetition 1		Repetition 2		Repetition 3		Repetition 4		Repetition 5	
Idle time [s]	down	up	down	up	down	up	down	up	down	up
0	62.8	62.2	63.5	63.2	63.0	62.8	64.2	64.4	64.6	64.4
5	65.2	65.1	63.6	63.0	63.2	62.7	64.5	63.3	64.0	63.9
10	62.8	62.7	62.4	62.6	62.6	63.3	63.1	63.1	63.7	63.6
20	63.3	62.6	63.2	63.3	62.3	63.1	64.2	63.4	62.9	62.4
40	64.5	63.8	63.4	63.2	62.5	62.5	63.8	63.0	63.8	63.6
80	63.3	63.1	63.3	63.4	63.6	63.5	63.4	63.0	64.8	64.1

C.2. Time-reversibility data

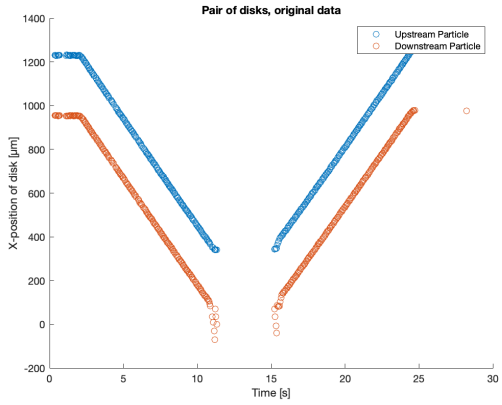

Trajectory of pair of disks #1

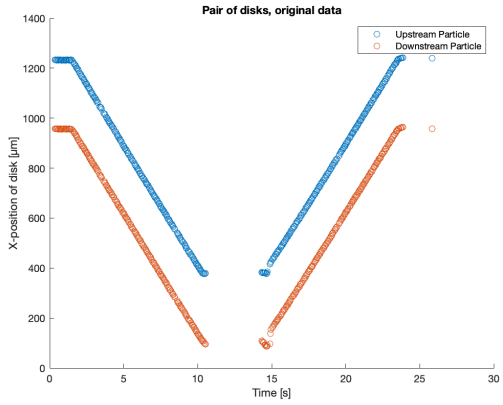

Trajectory of pair of disks #2

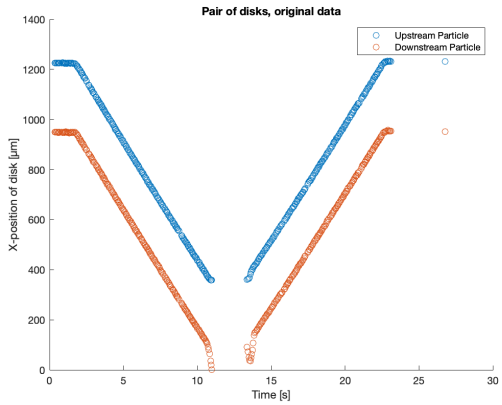

Trajectory of pair of disks #3

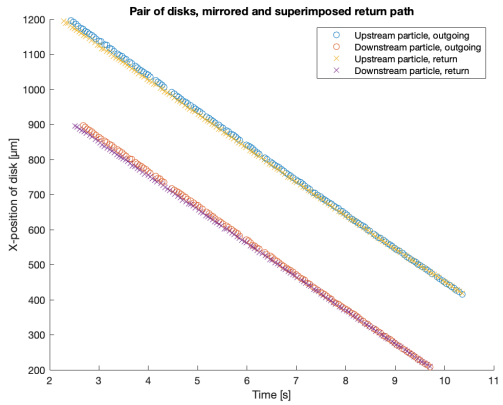

Mirrored & superimposed return path, #1

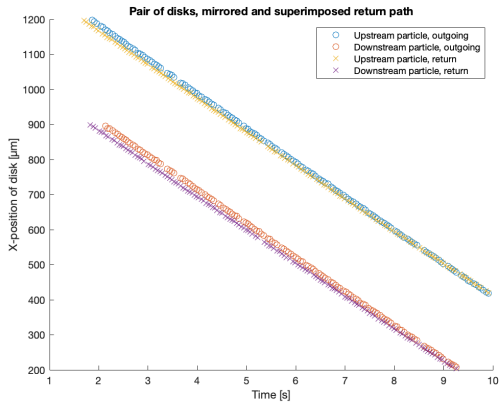

Mirrored & superimposed return path, #2

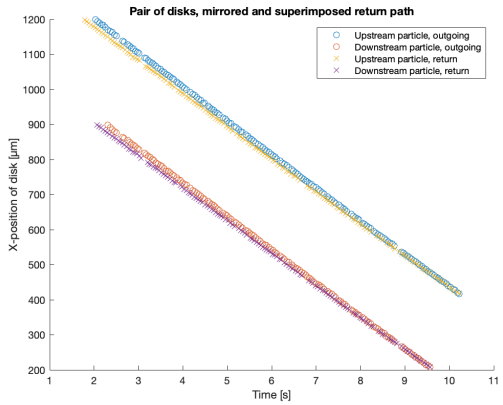

Mirrored & superimposed return path, #3

C.3. Light-beam uniformity data

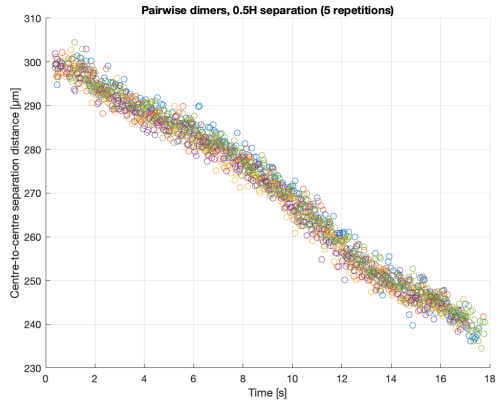

0.5H, regular dimer pair

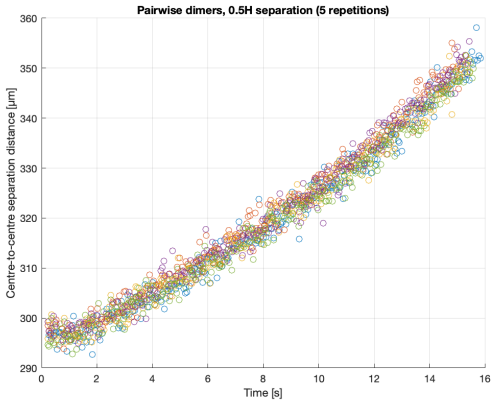

0.5H, reversed dimer pair (flipped channel)

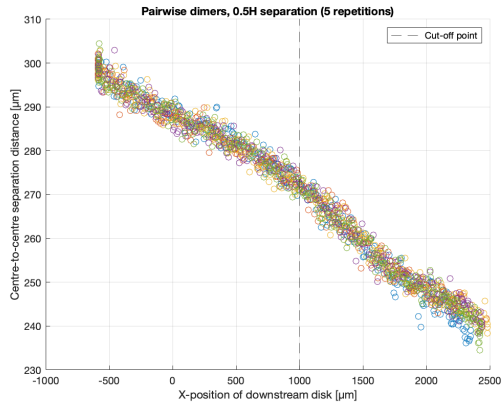

0.5H, regular dimer pair

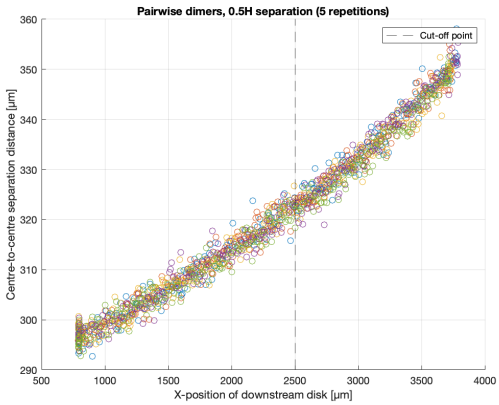

0.5H, reversed dimer pair (flipped channel)

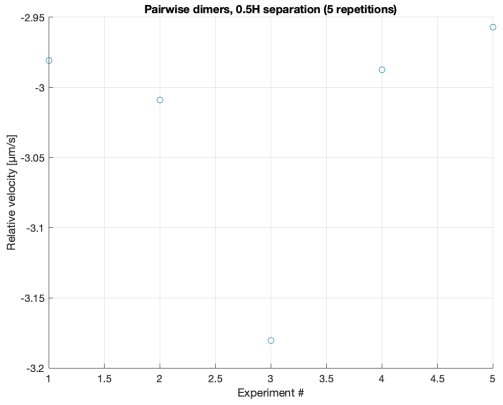

0.5H, regular dimer pair

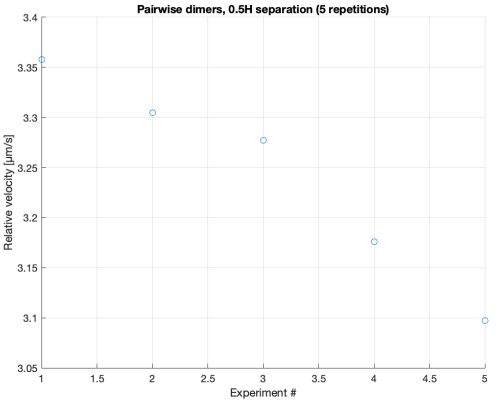

0.5H, reversed dimer pair (flipped channel)

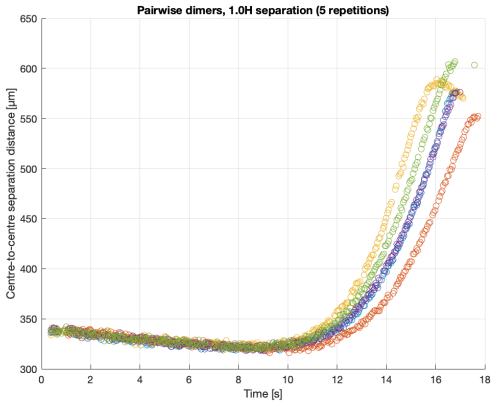

1.0H, regular dimer pair

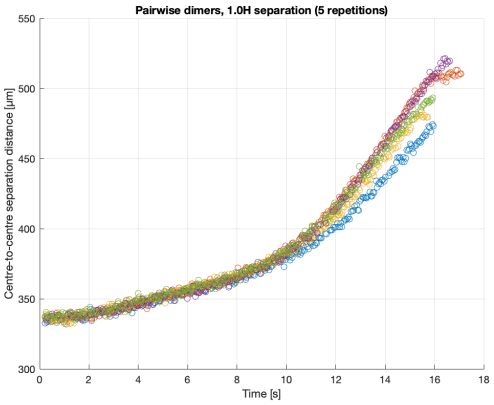

1.0H, reversed dimer pair (flipped channel)

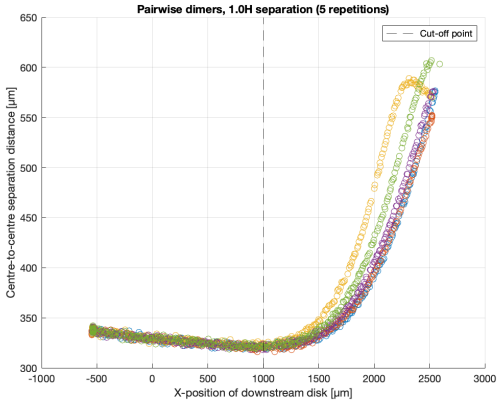

1.0H, regular dimer pair

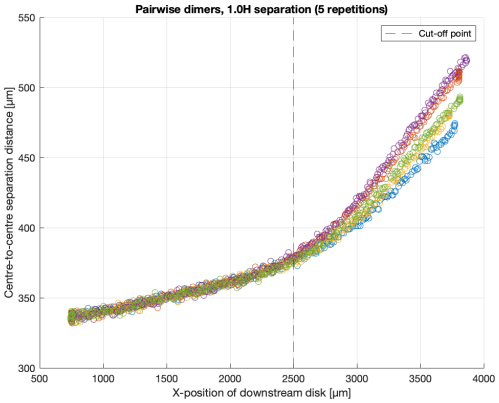

1.0H, reversed dimer pair (flipped channel)

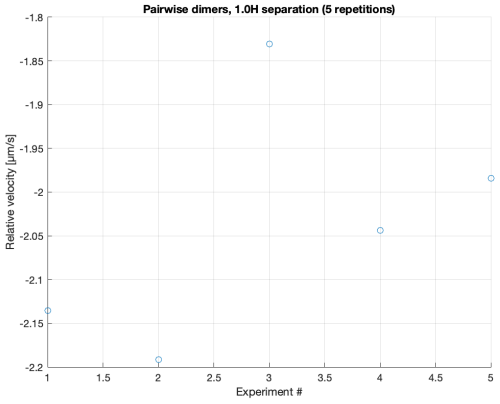

1.0H, regular dimer pair

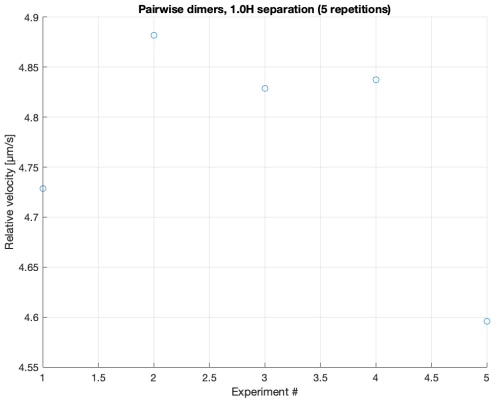

1.0H, reversed dimer pair (flipped channel)

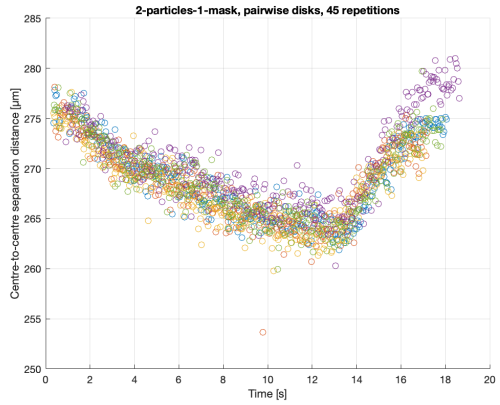

1.0H, regular disk pair

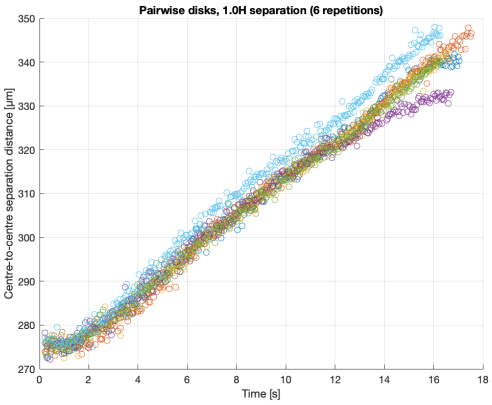

1.0H, reversed disk pair (flipped channel)

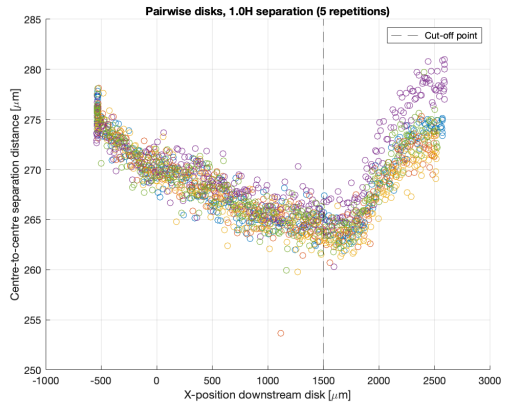

1.0H, regular disk pair

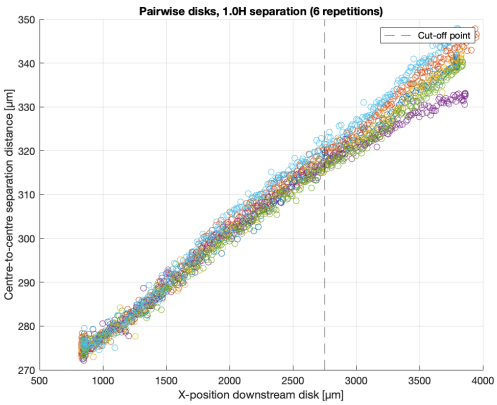

1.0H, reversed disk pair (flipped channel)

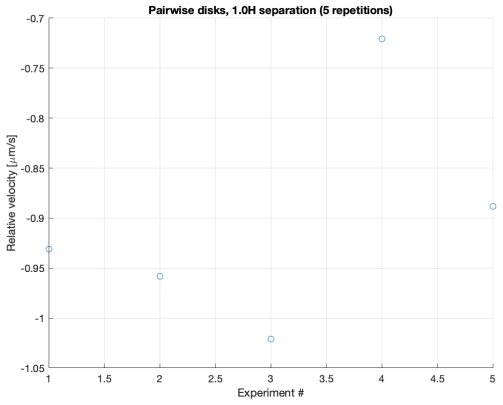

1.0H, regular disk pair

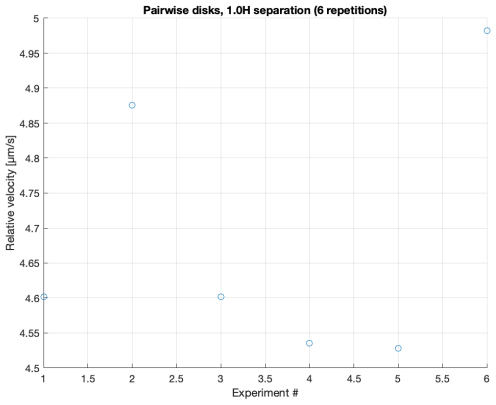

1.0H, reversed disk pair (flipped channel)

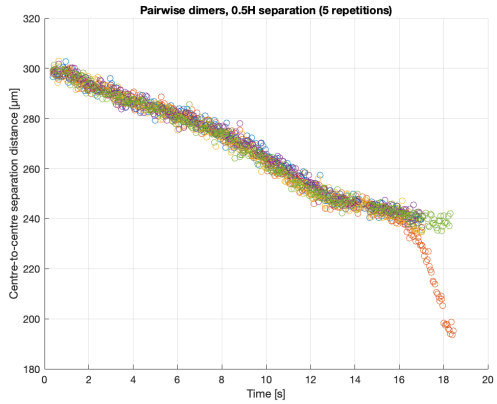

0.5H, flipped mask dimer pair

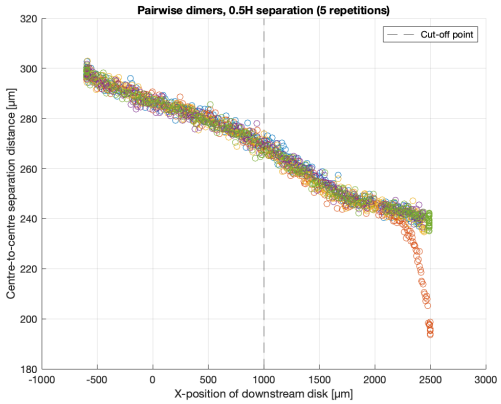

0.5H, flipped mask dimer pair (flipped channel)

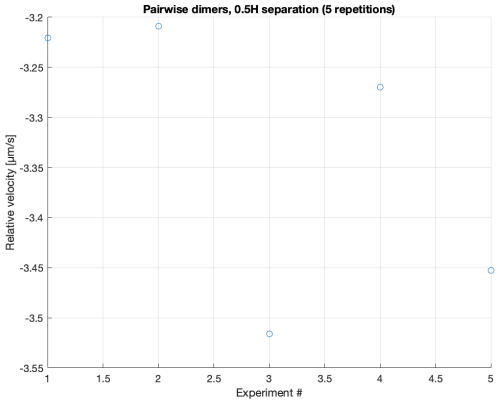

0.5H, flipped mask dimer pair

D

Raw data: shape-dependent particle thickness

This appendix lists the raw data for the shape-dependence of particle thickness results, of section 4.4. The data is structured on a per-figure basis.

D.1. Figure 4.7

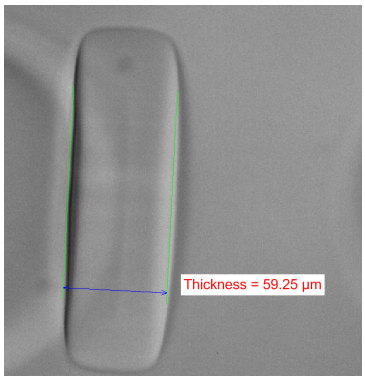

Disk pair #1, downstream particle

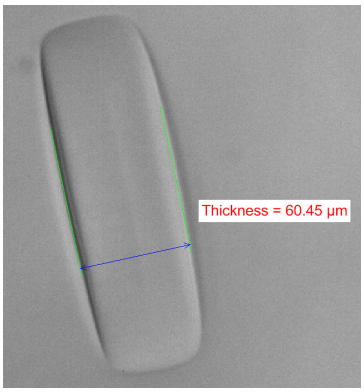

Disk pair #1, upstream particle

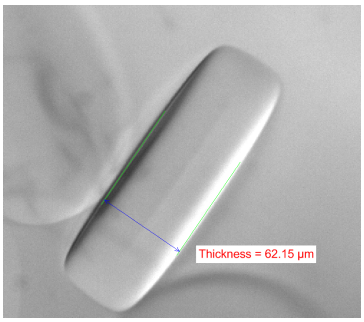

Disk pair #2, downstream particle

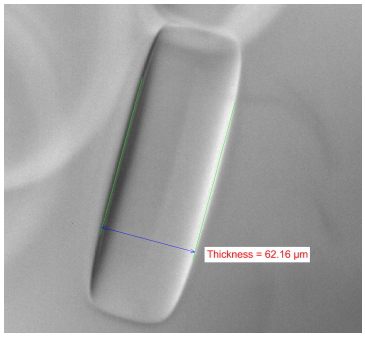

Disk pair #2, upstream particle

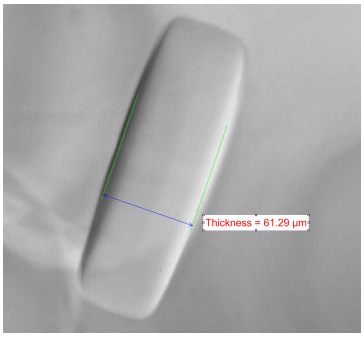

Disk pair #3, downstream particle

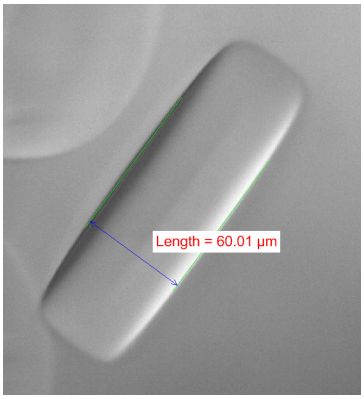

Disk pair #3, upstream particle

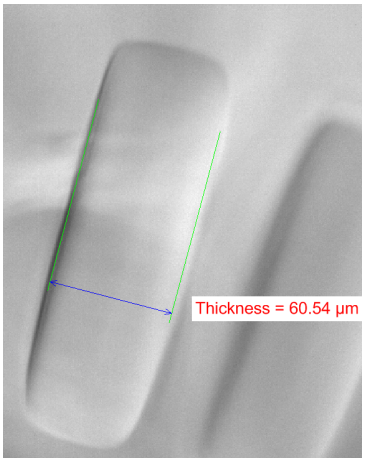

Disk pair #4, downstream particle

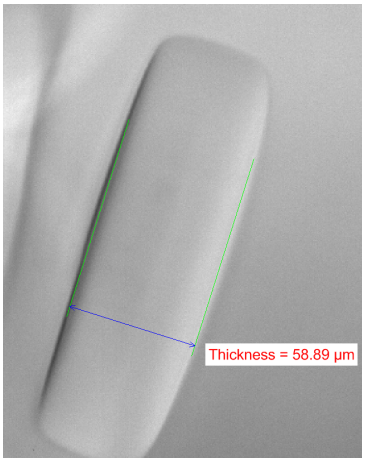

Disk pair #4, upstream particle

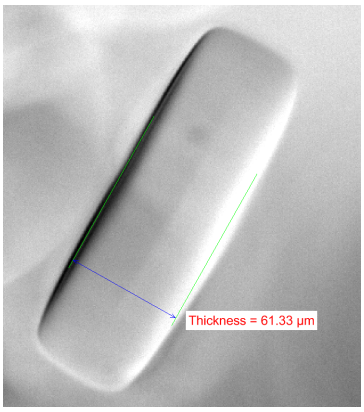

Disk pair #5, downstream particle

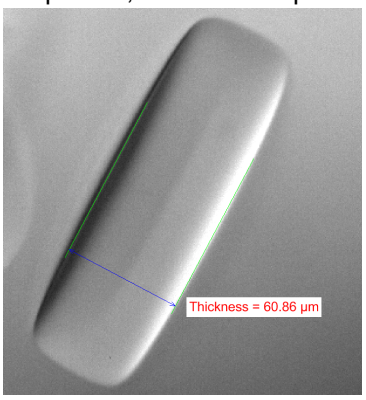

Disk pair #5, upstream particle

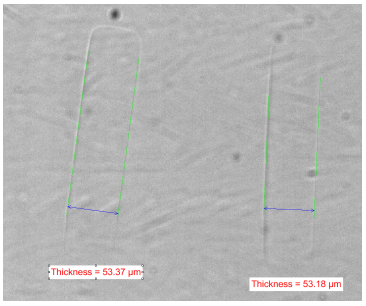

Rod pair #1

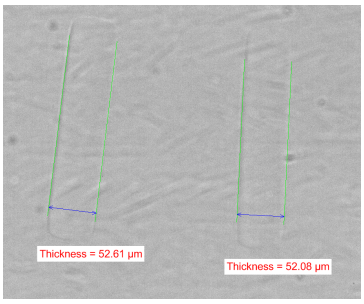

Rod pair #2

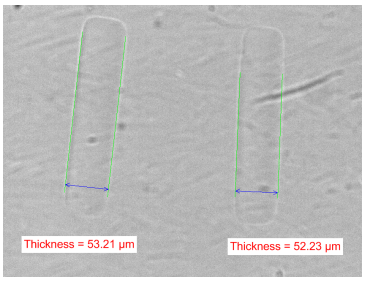

Rod pair #3

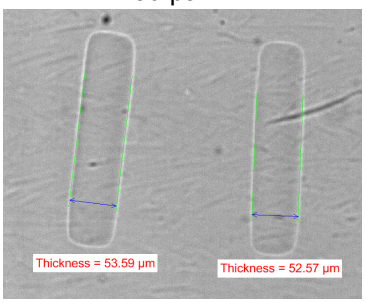

Rod pair #4

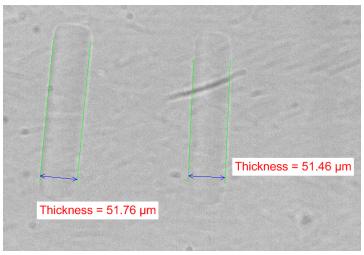

Rod pair #5

E

Raw data: dimer ratio series

This appendix lists all graphs with raw data for the dimer ratio series. Graphs start on the next page.

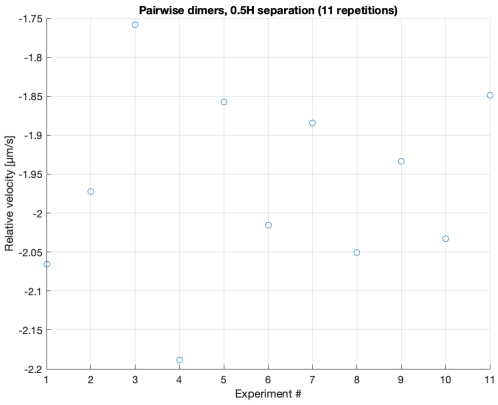

0.5H, Dimer, $\kappa = 1.30$

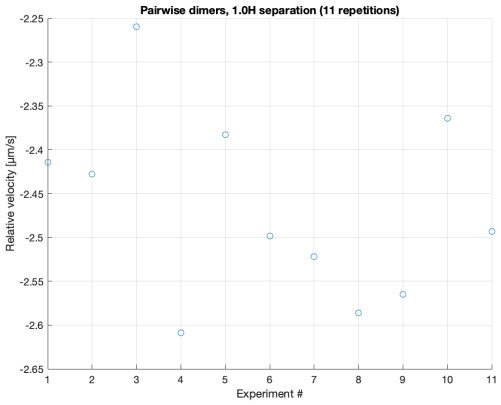

1.0H, Dimer, $\kappa = 1.30$

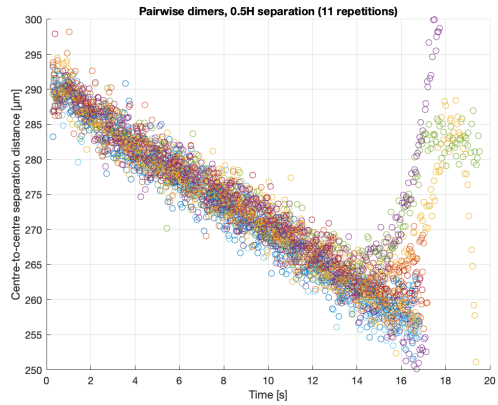

0.5H, Dimer, $\kappa = 1.30$

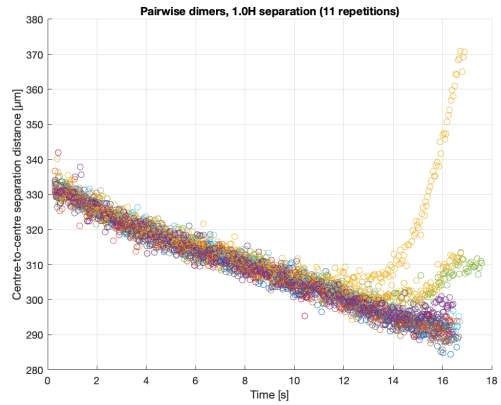

1.0H, Dimer, $\kappa = 1.30$

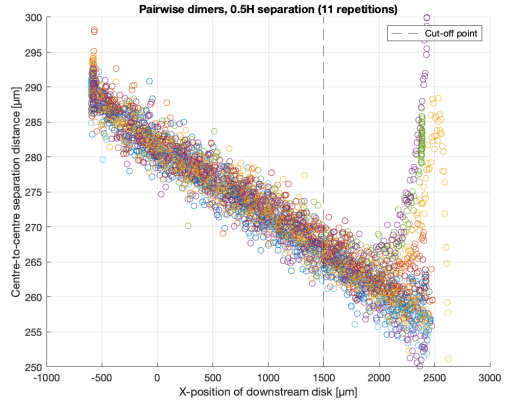

0.5H, Dimer, $\kappa = 1.30$

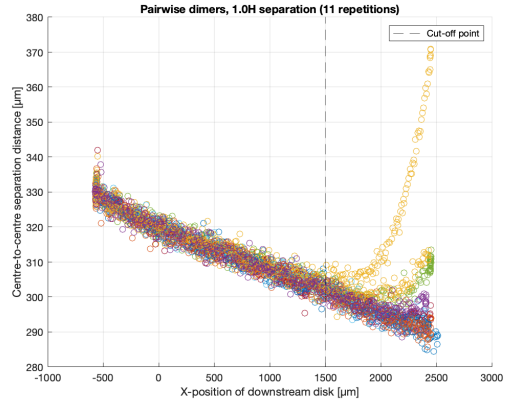

1.0H, Dimer, $\kappa = 1.30$

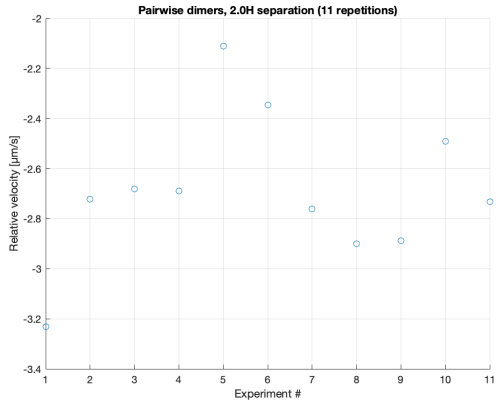

2.0H, Dimer, $\kappa = 1.30$

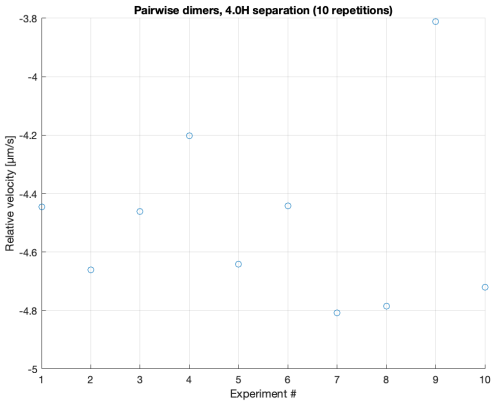

4.0H, Dimer, $\kappa = 1.30$

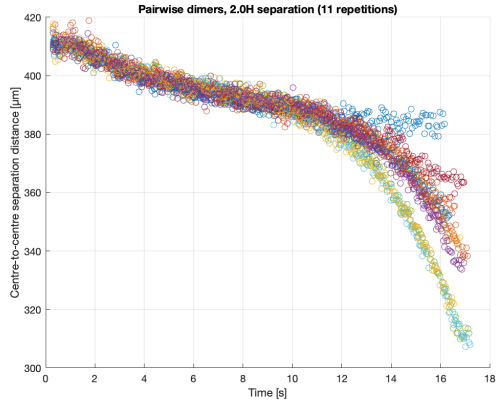

2.0H, Dimer, $\kappa = 1.30$

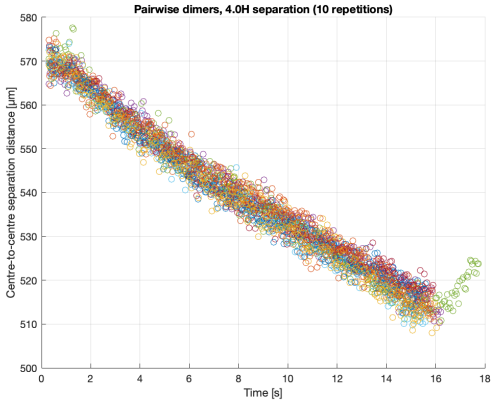

4.0H, Dimer, $\kappa = 1.30$

2.0H, Dimer, $\kappa = 1.30$

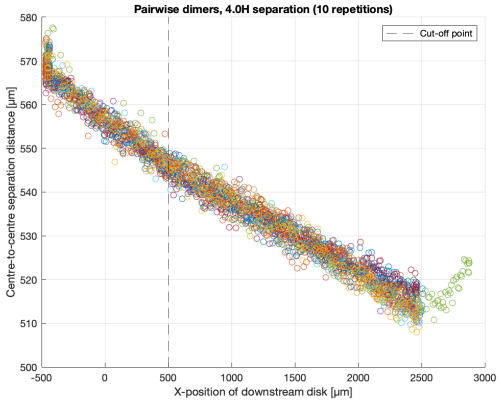

4.0H, Dimer, $\kappa = 1.30$

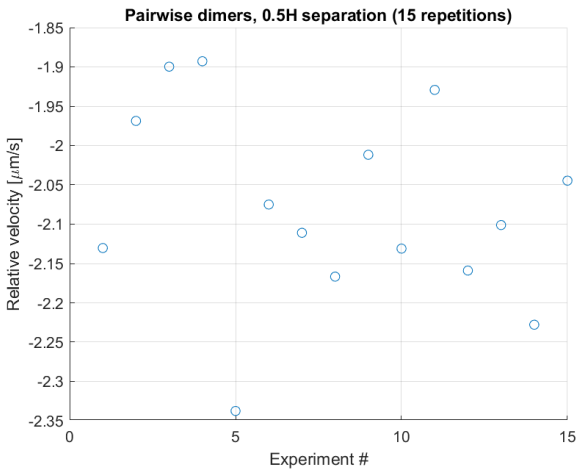

0.5H, Dimer, $\kappa = 1.50$

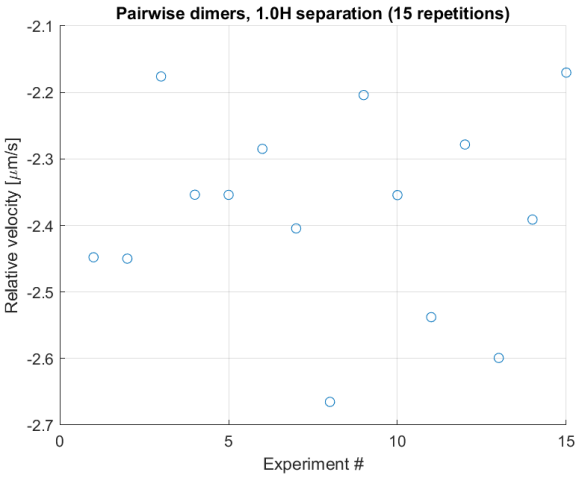

1.0H, Dimer, $\kappa = 1.50$

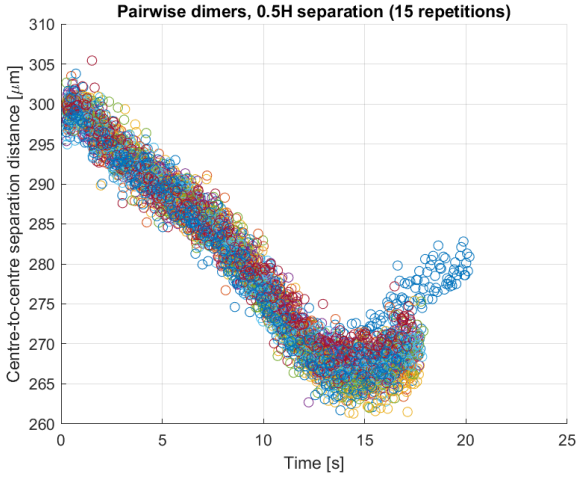

0.5H, Dimer, $\kappa = 1.50$

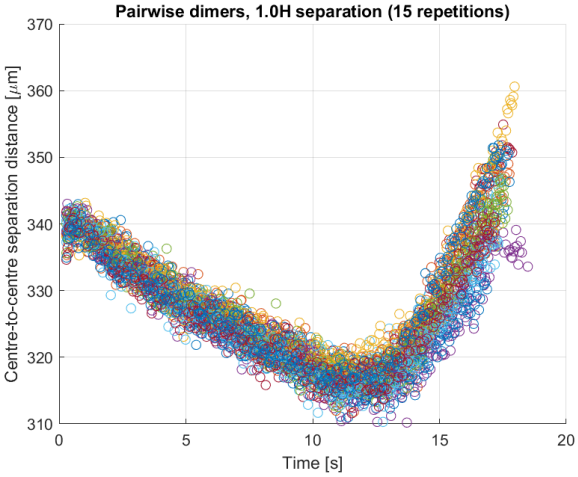

1.0H, Dimer, $\kappa = 1.50$

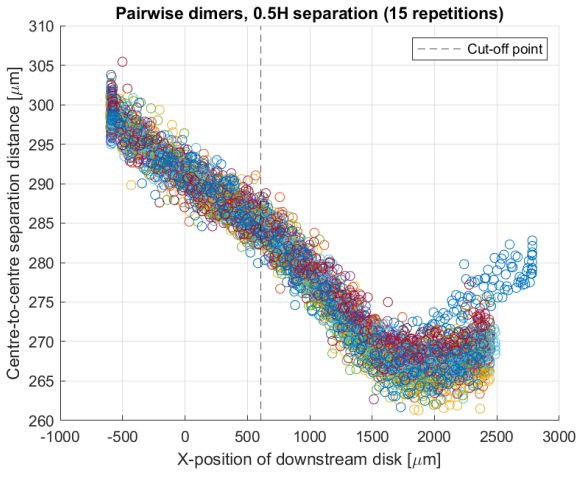

0.5H, Dimer, $\kappa = 1.50$

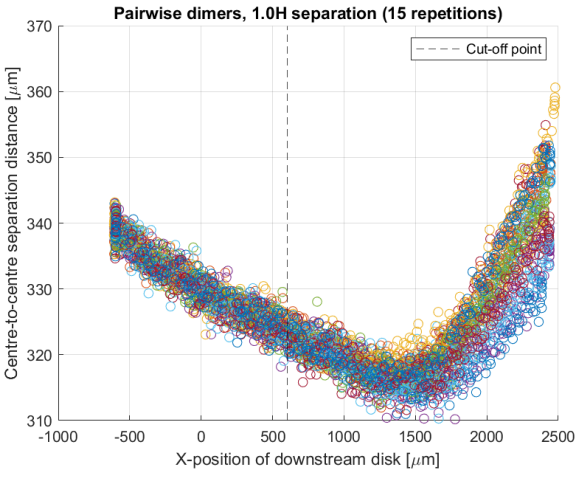

1.0H, Dimer, $\kappa = 1.50$

2.0H, Dimer, $\kappa = 1.50$

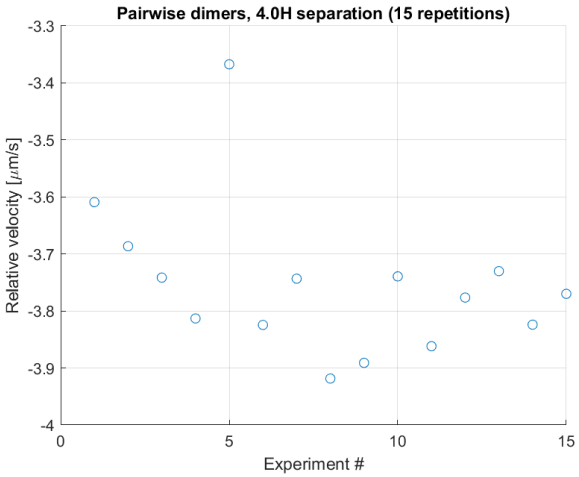

4.0H, Dimer, $\kappa = 1.50$

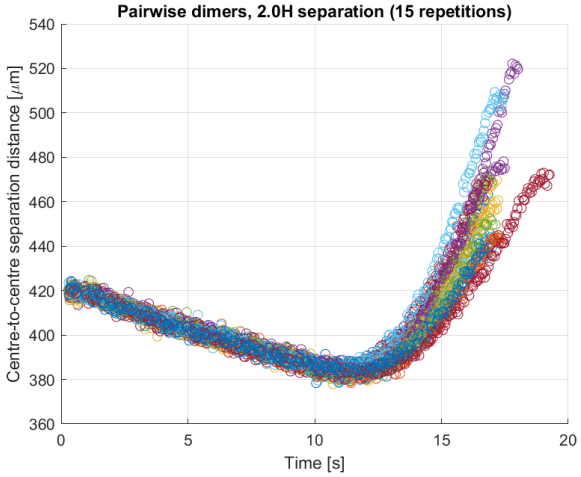

2.0H, Dimer, $\kappa = 1.50$

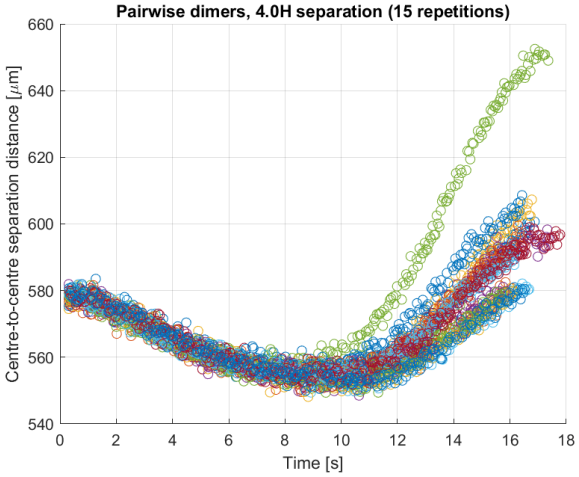

4.0H, Dimer, $\kappa = 1.50$

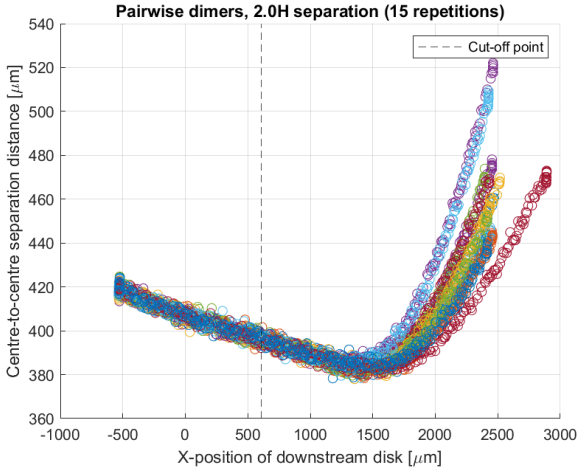

2.0H, Dimer, $\kappa = 1.50$

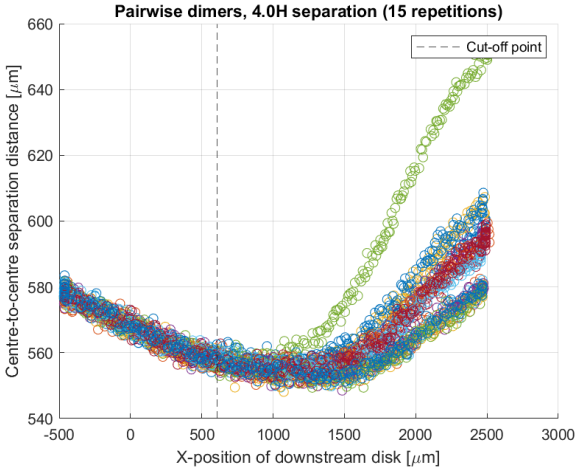

4.0H, Dimer, $\kappa = 1.50$

0.5H, Dimer, $\kappa = 2.00$

1.0H, Dimer, $\kappa = 2.00$

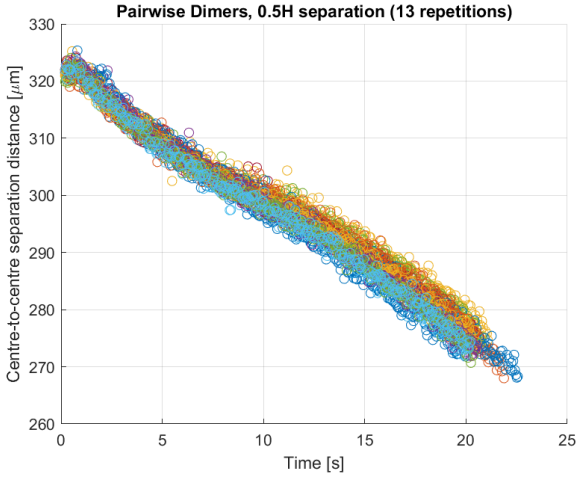

0.5H, Dimer, $\kappa = 2.00$

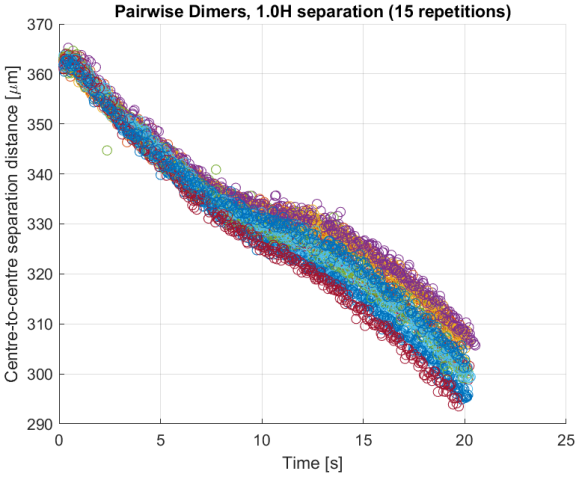

1.0H, Dimer, $\kappa = 2.00$

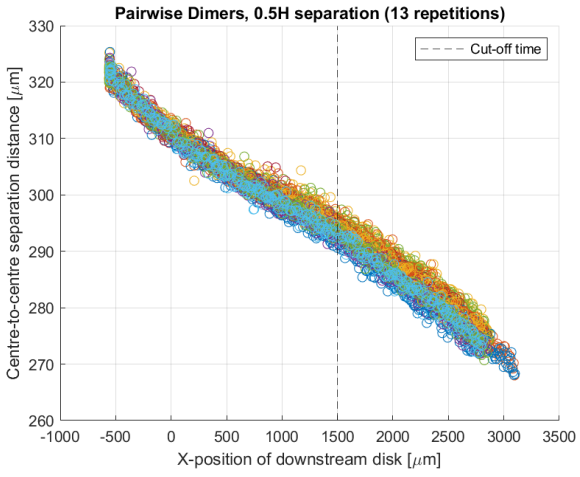

0.5H, Dimer, $\kappa = 2.00$

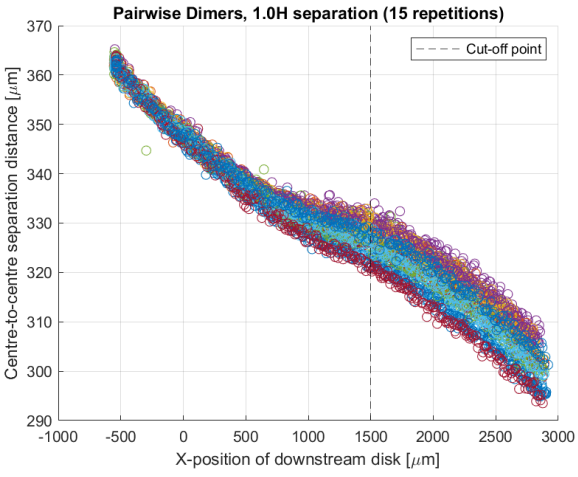

1.0H, Dimer, $\kappa = 2.00$

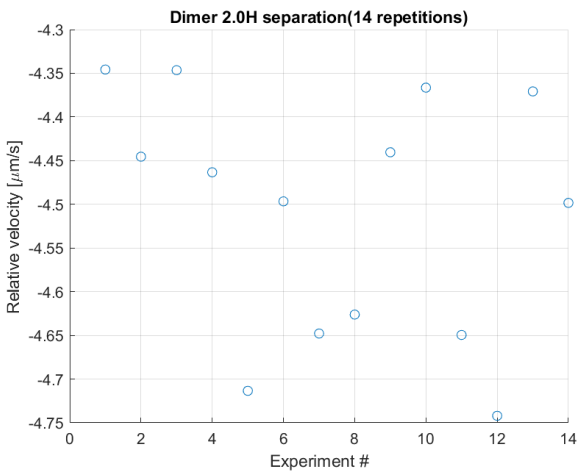

2.0H, Dimer, $\kappa = 2.00$

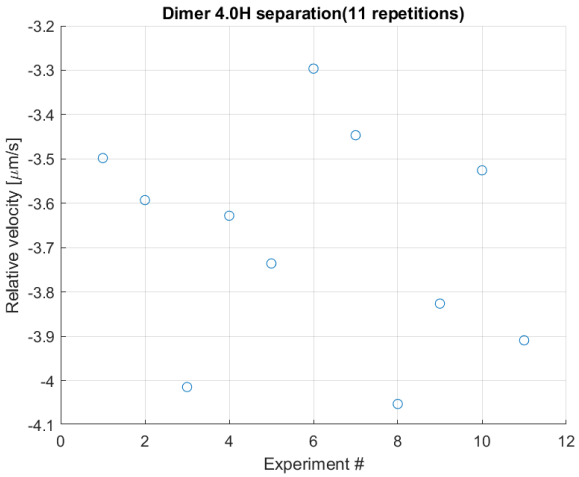

4.0H, Dimer, $\kappa = 2.00$

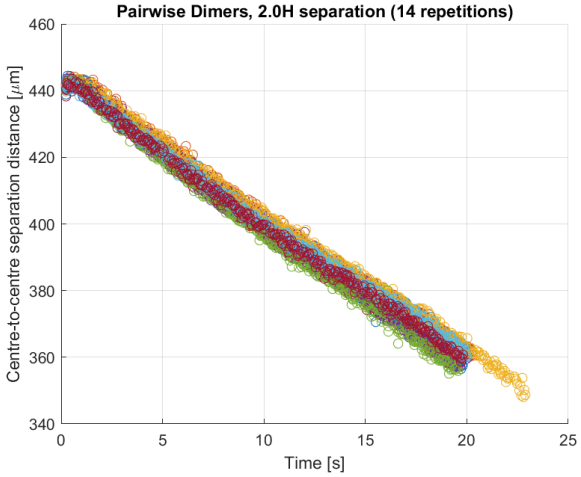

2.0H, Dimer, $\kappa = 2.00$

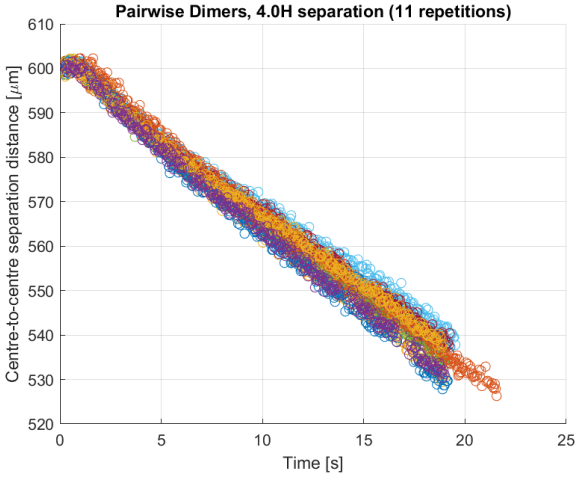

4.0H, Dimer, $\kappa = 2.00$

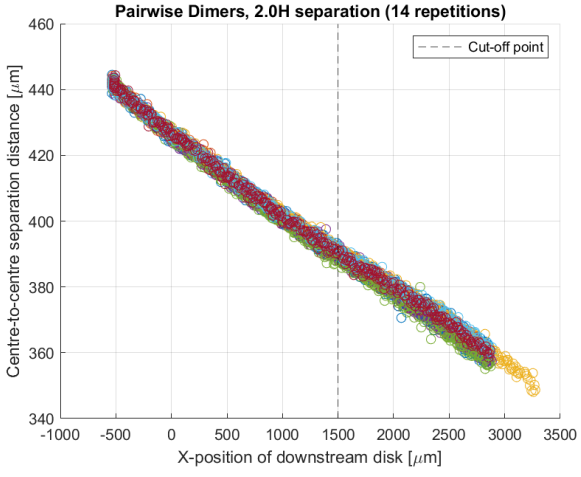

2.0H, Dimer, $\kappa = 2.00$

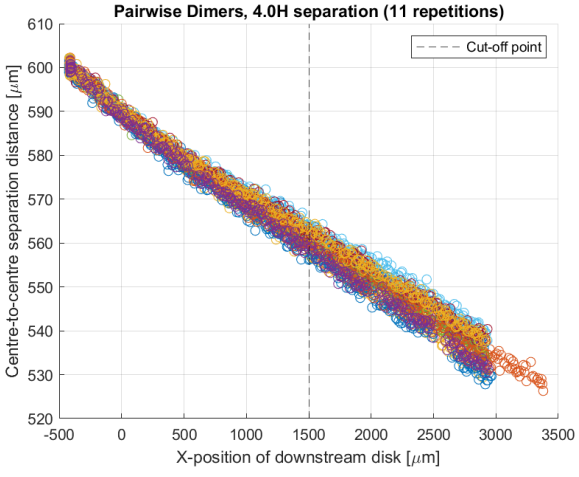

4.0H, Dimer, $\kappa = 2.00$

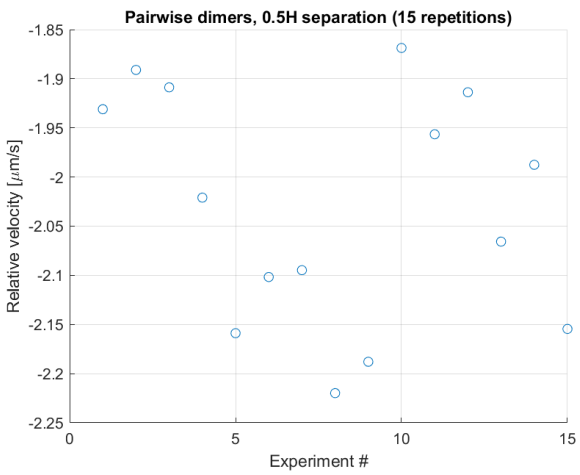

0.5H, Dimer, $\kappa = 2.50$

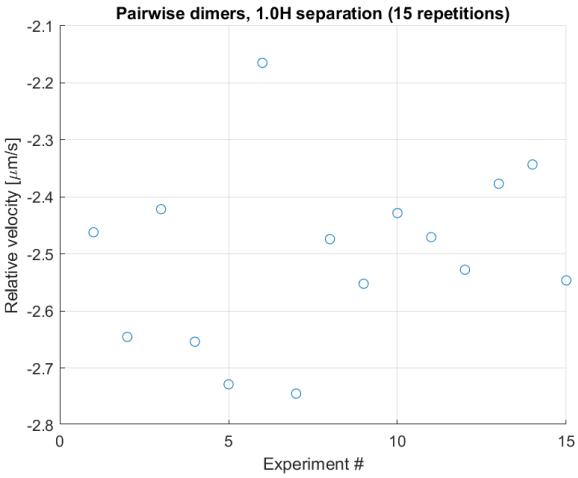

1.0H, Dimer, $\kappa = 2.50$

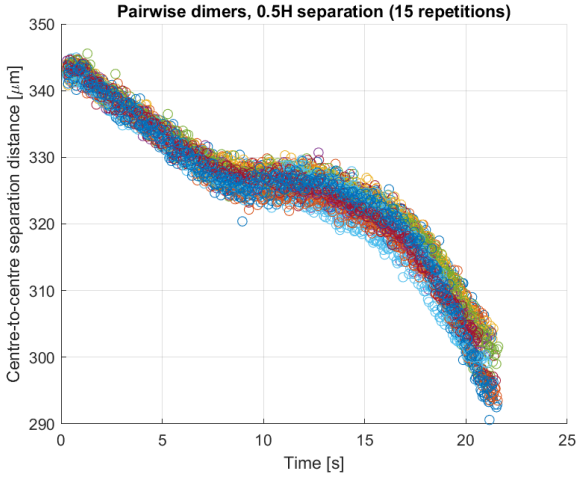

0.5H, Dimer, $\kappa = 2.50$

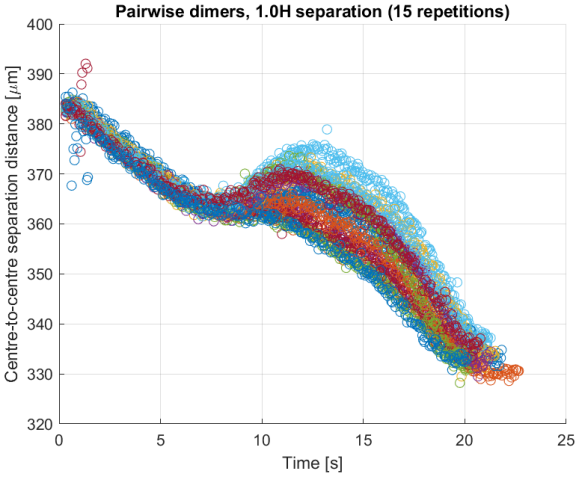

1.0H, Dimer, $\kappa = 2.50$

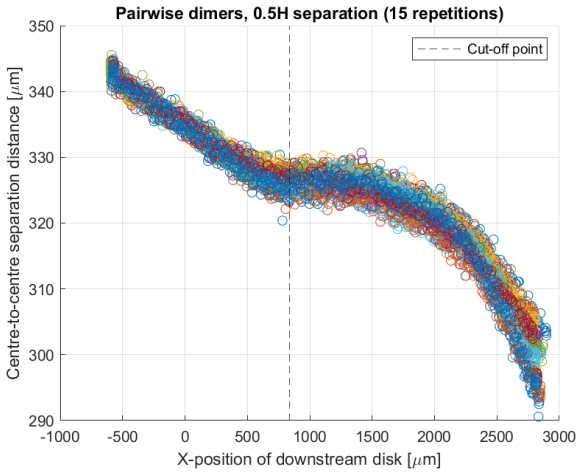

0.5H, Dimer, $\kappa = 2.50$

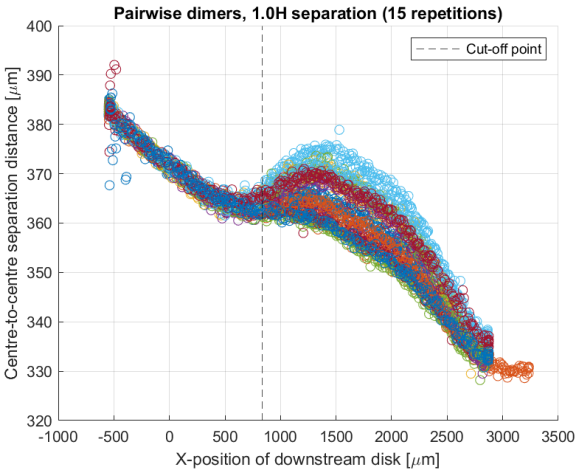

1.0H, Dimer, $\kappa = 2.50$

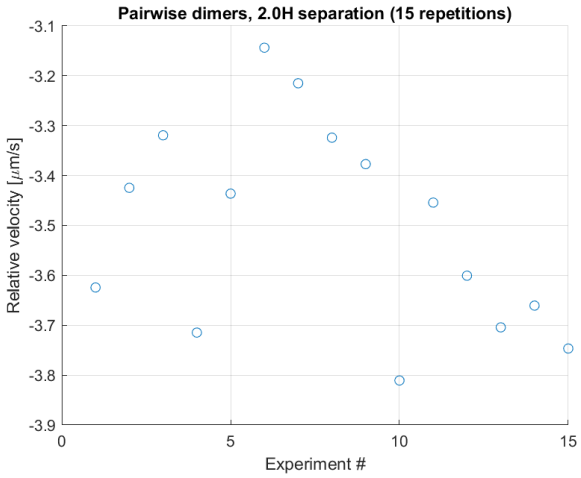

2.0H, Dimer, $\kappa = 2.50$

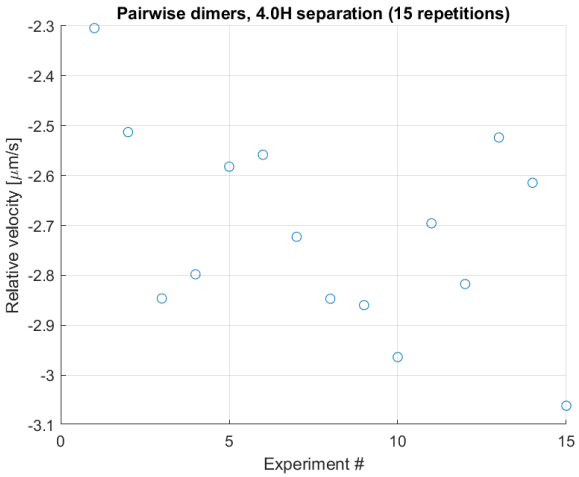

4.0H, Dimer, $\kappa = 2.50$

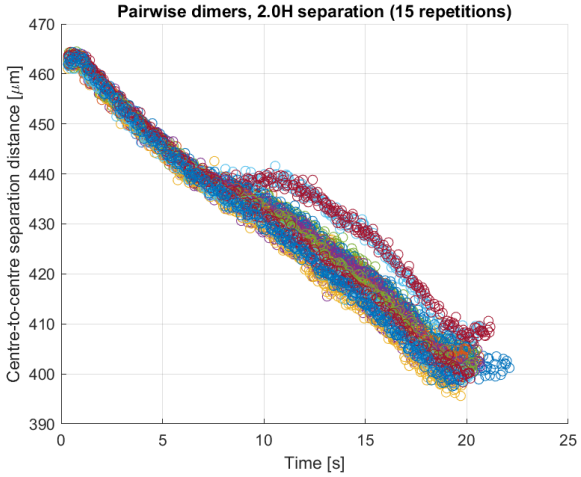

2.0H, Dimer, $\kappa = 2.50$

4.0H, Dimer, $\kappa = 2.50$

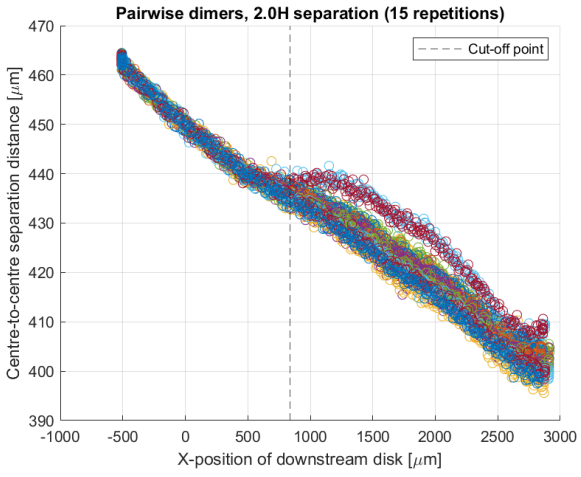

2.0H, Dimer, $\kappa = 2.50$

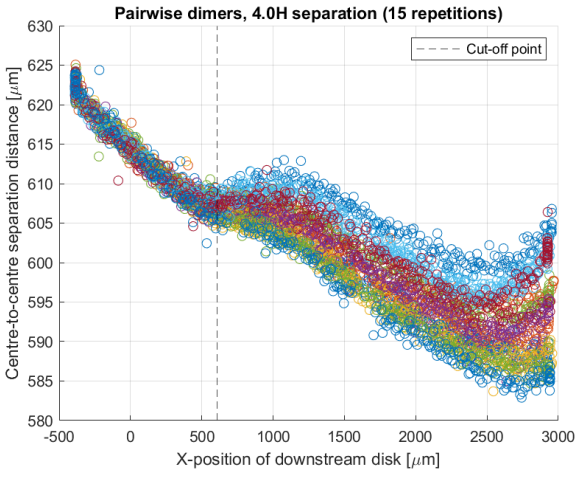

4.0H, Dimer, $\kappa = 2.50$

F

Raw data: tripod ratio series

This appendix lists all graphs with raw data for the trimer ratio series. Graphs start on the next page.

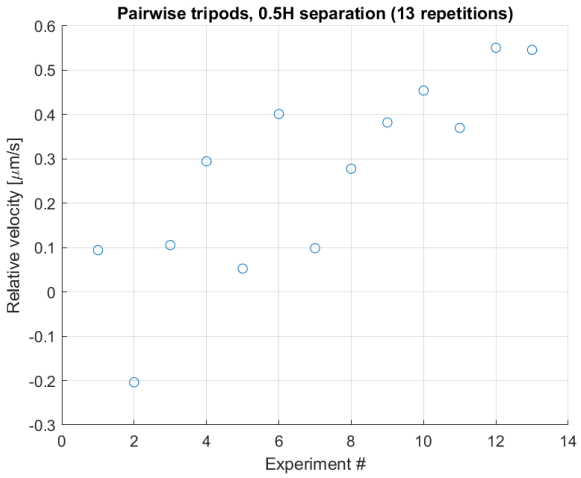

0.5H, Trimer, $\kappa = 1.25$

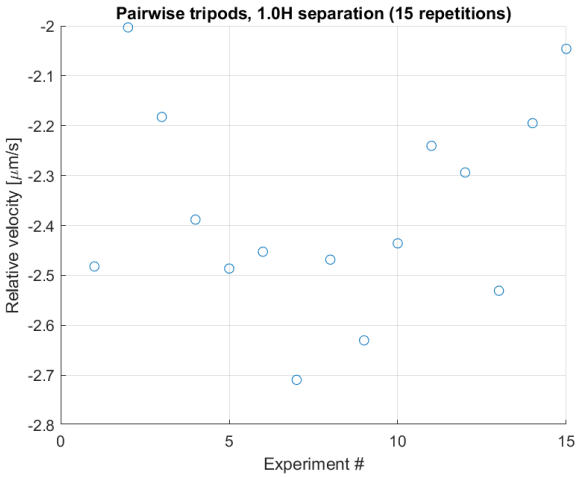

1.0H, Trimer, $\kappa = 1.25$

0.5H, Trimer, $\kappa = 1.25$

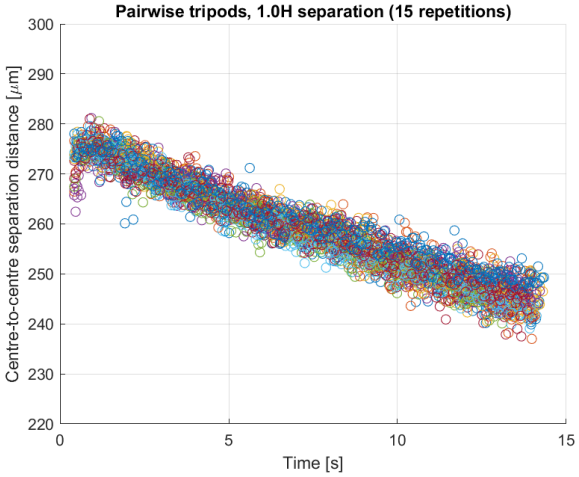

1.0H, Trimer, $\kappa = 1.25$

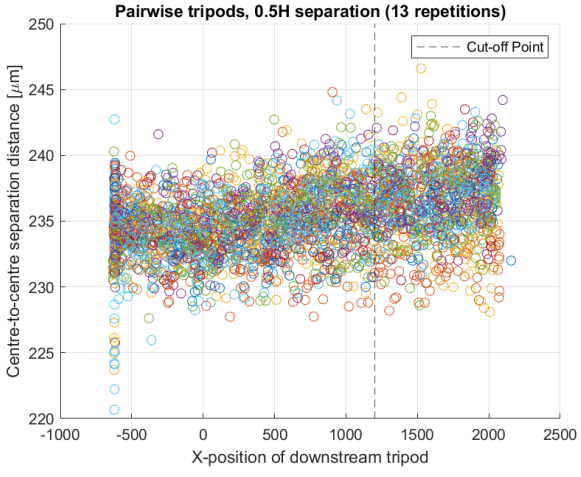

0.5H, Trimer, $\kappa = 1.25$

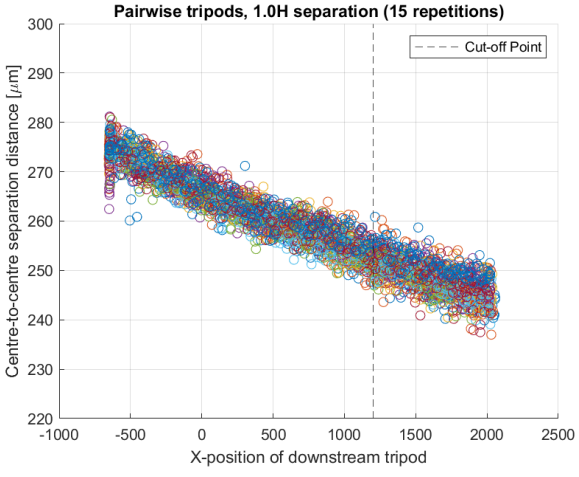

1.0H, Trimer, $\kappa = 1.25$

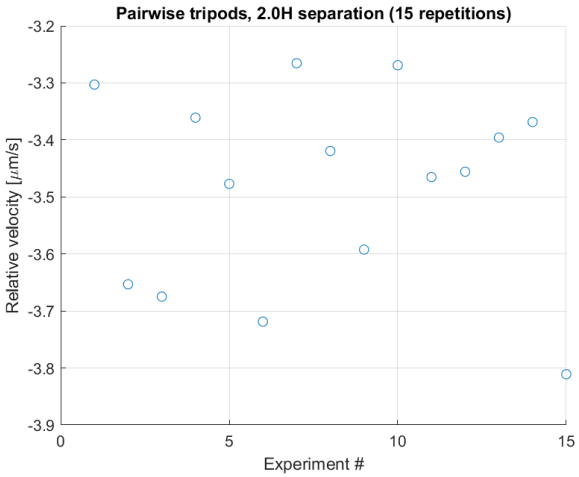

2.0H, Trimer, $\kappa = 1.25$

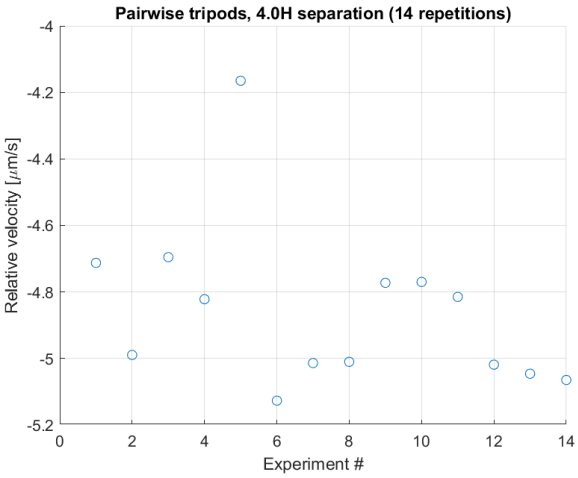

4.0H, Trimer, $\kappa = 1.25$

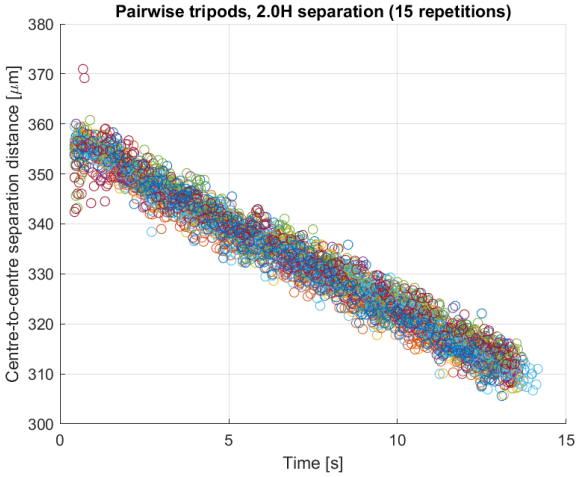

2.0H, Trimer, $\kappa = 1.25$

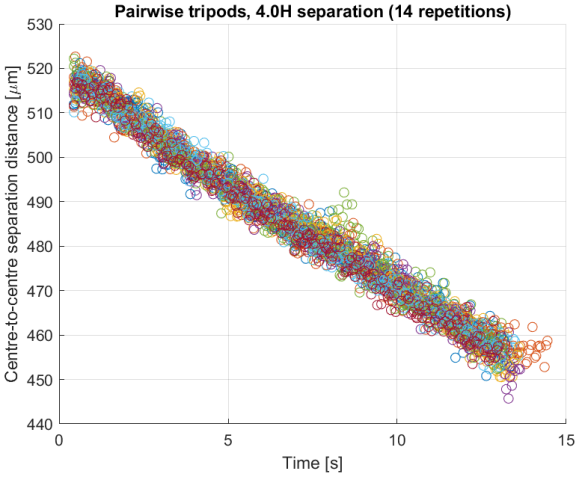

4.0H, Trimer, $\kappa = 1.25$

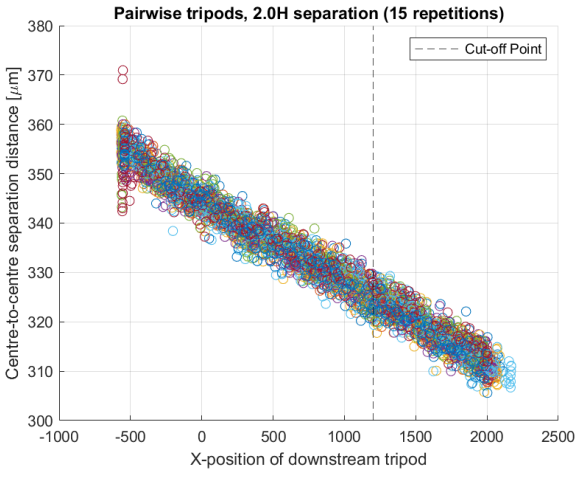

2.0H, Trimer, $\kappa = 1.25$

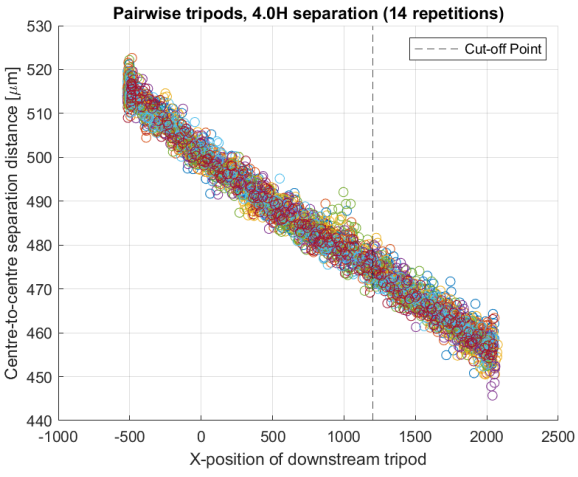

4.0H, Trimer, $\kappa = 1.25$

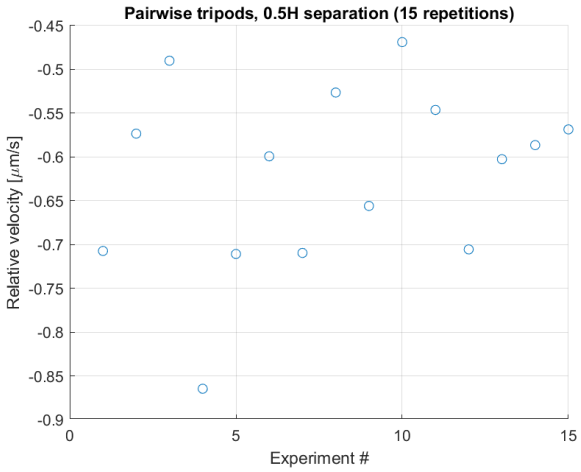

0.5H, Trimer, $\kappa = 1.50$

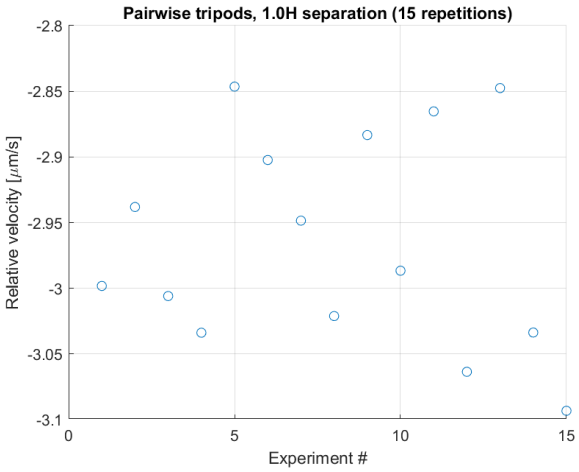

1.0H, Trimer, $\kappa = 1.50$

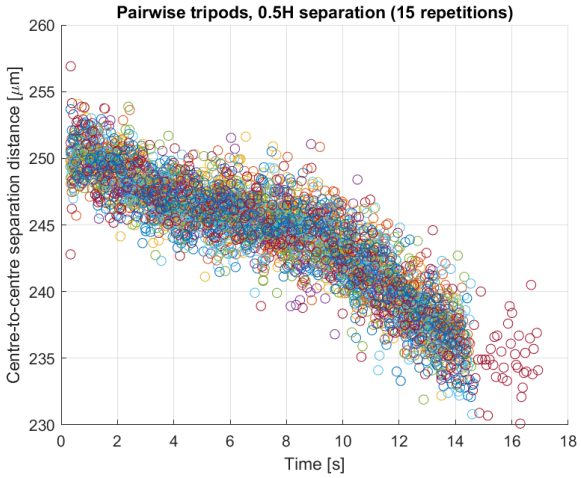

0.5H, Trimer, $\kappa = 1.50$

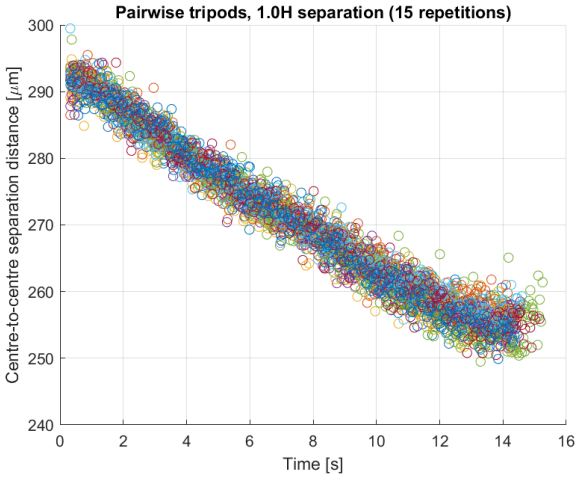

1.0H, Trimer, $\kappa = 1.50$

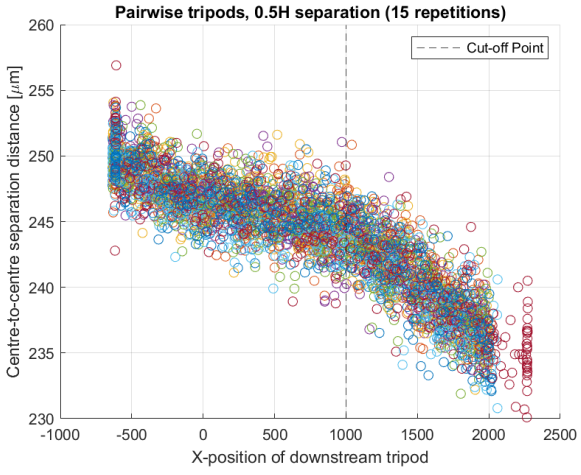

0.5H, Trimer, $\kappa = 1.50$

1.0H, Trimer, $\kappa = 1.50$

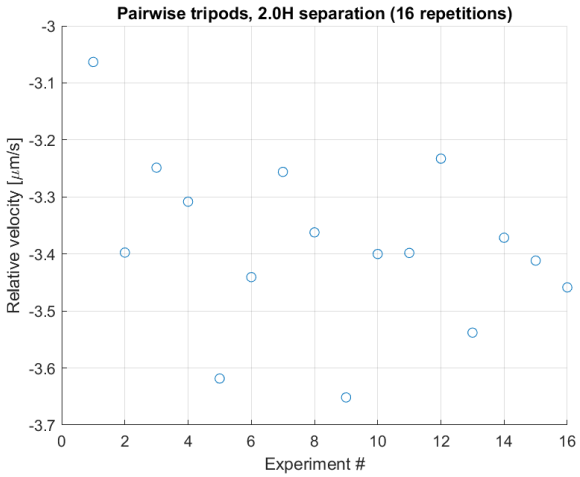

2.0H, Trimer, $\kappa = 1.50$

4.0H, Trimer, $\kappa = 1.50$

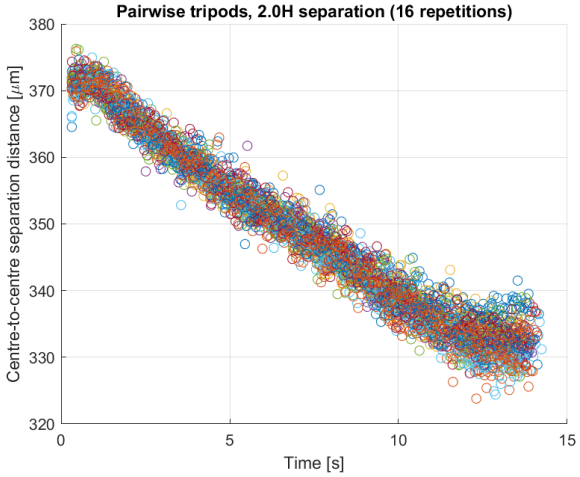

2.0H, Trimer, $\kappa = 1.50$

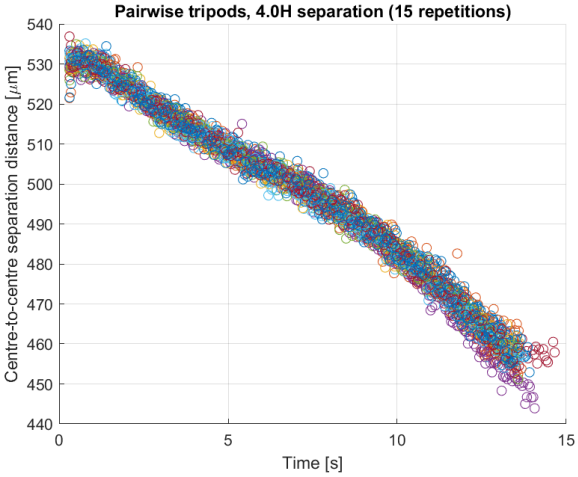

4.0H, Trimer, $\kappa = 1.50$

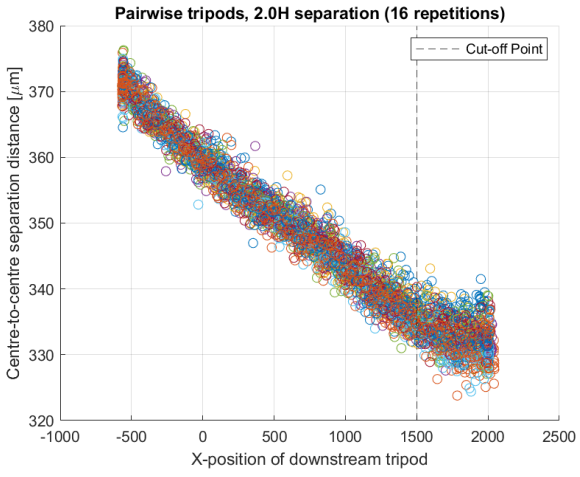

2.0H, Trimer, $\kappa = 1.50$

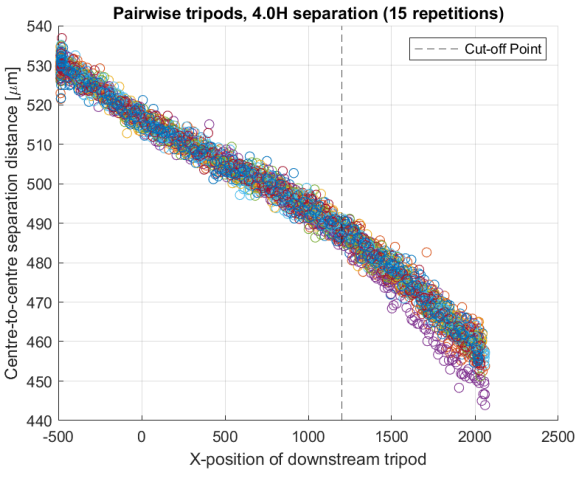

4.0H, Trimer, $\kappa = 1.50$

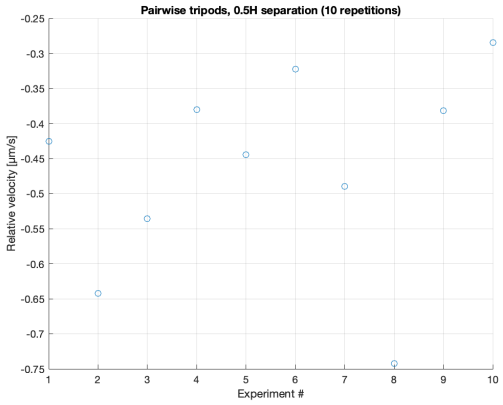

0.5H, Trimer, $\kappa = 2.00$

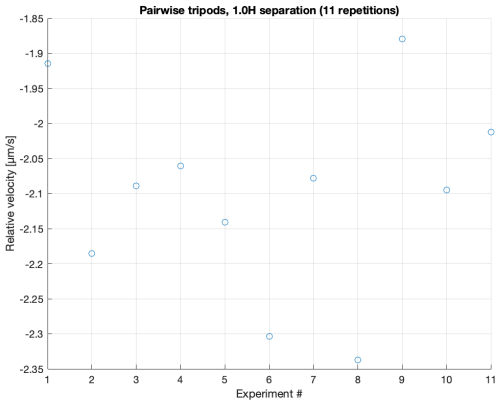

1.0H, Trimer, $\kappa = 2.00$

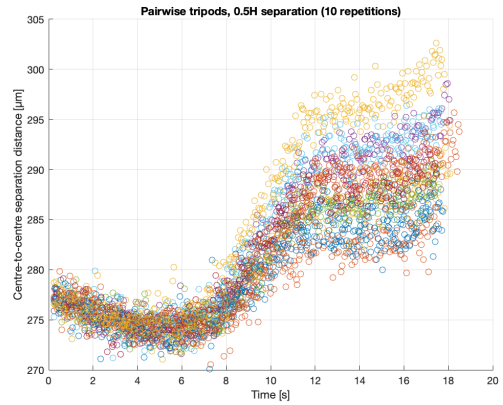

0.5H, Trimer, $\kappa = 2.00$

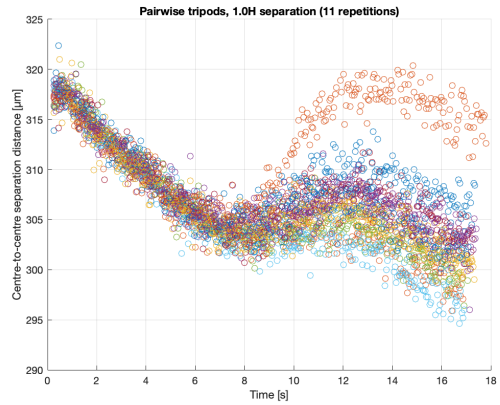

1.0H, Trimer, $\kappa = 2.00$

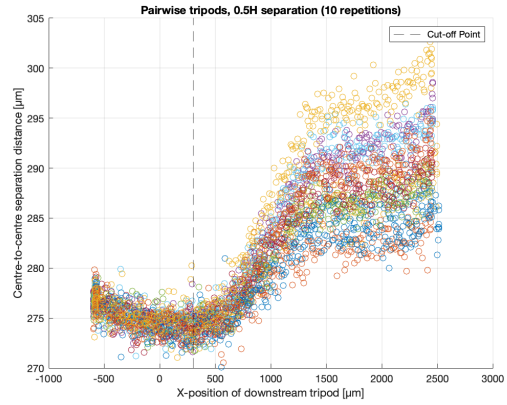

0.5H, Trimer, $\kappa = 2.00$

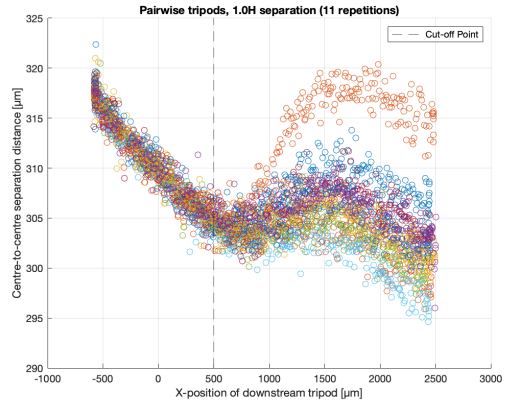

1.0H, Trimer, $\kappa = 2.00$

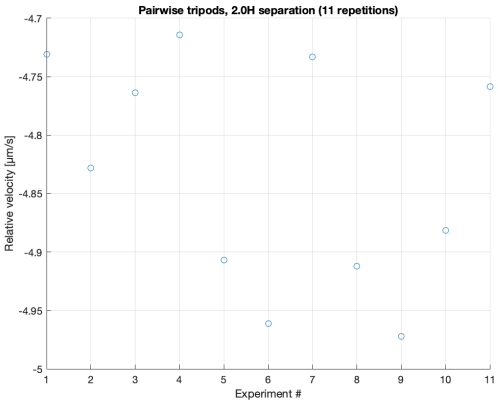

2.0H, Trimer, $\kappa = 2.00$

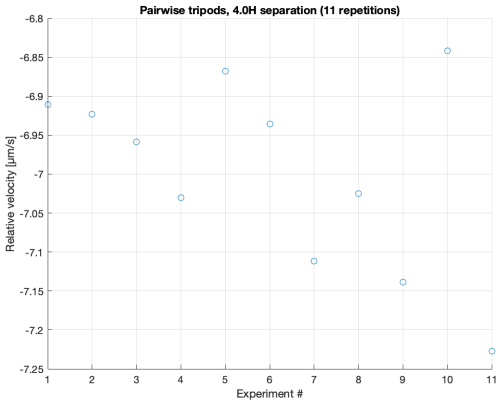

4.0H, Trimer, $\kappa = 2.00$

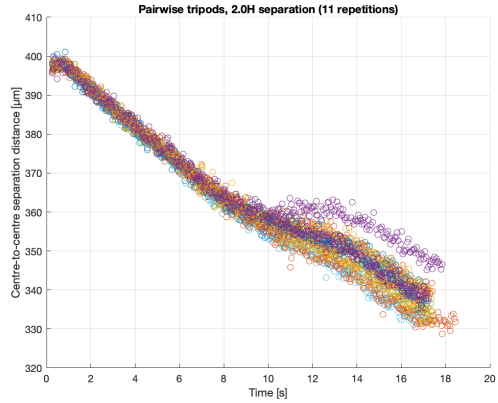

2.0H, Trimer, $\kappa = 2.00$

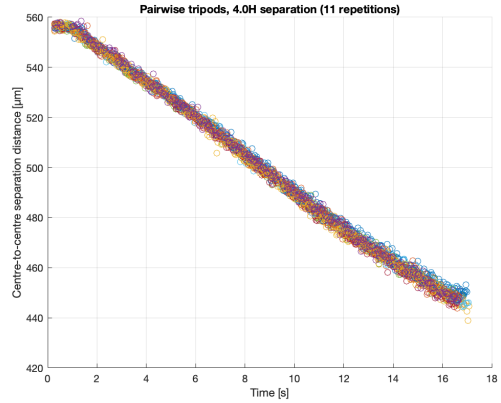

4.0H, Trimer, $\kappa = 2.00$

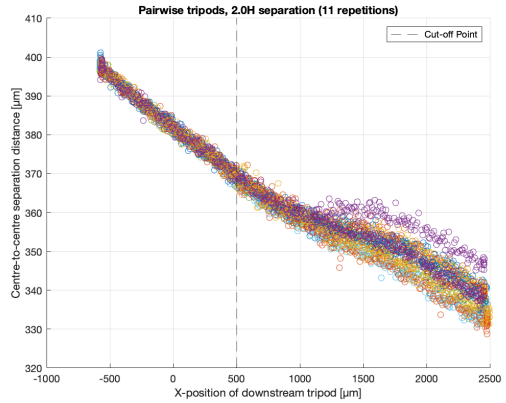

2.0H, Trimer, $\kappa = 2.00$

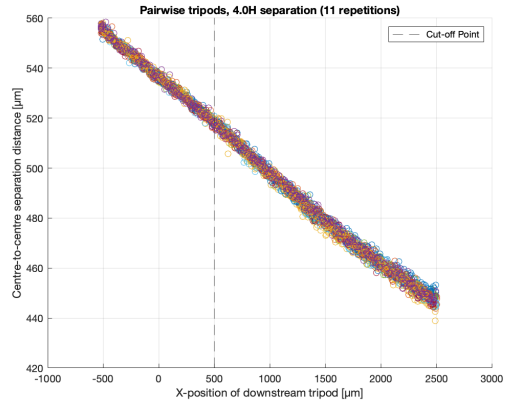

4.0H, Trimer, $\kappa = 2.00$

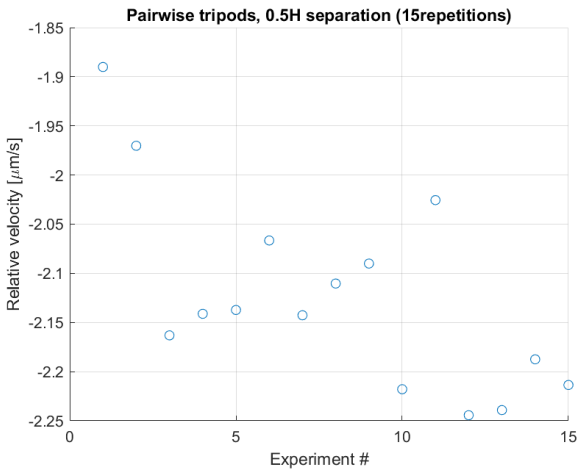

0.5H, Trimer, $\kappa = 2.50$

1.0H, Trimer, $\kappa = 2.50$

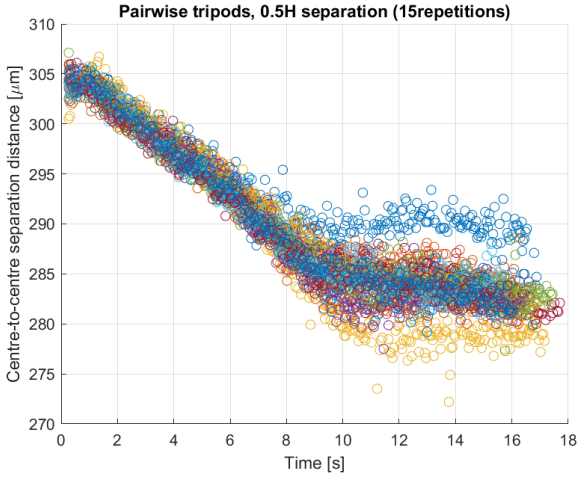

0.5H, Trimer, $\kappa = 2.50$

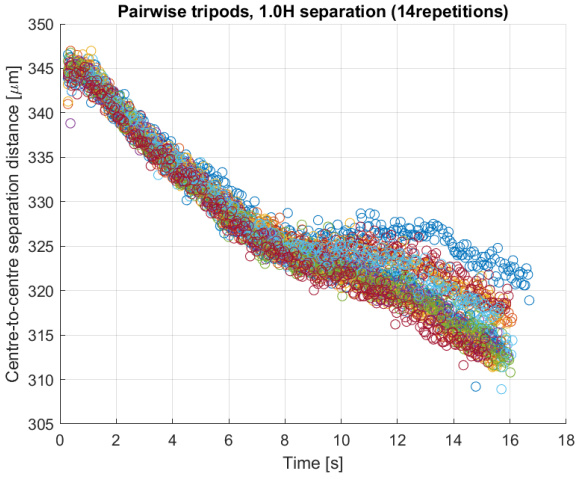

1.0H, Trimer, $\kappa = 2.50$

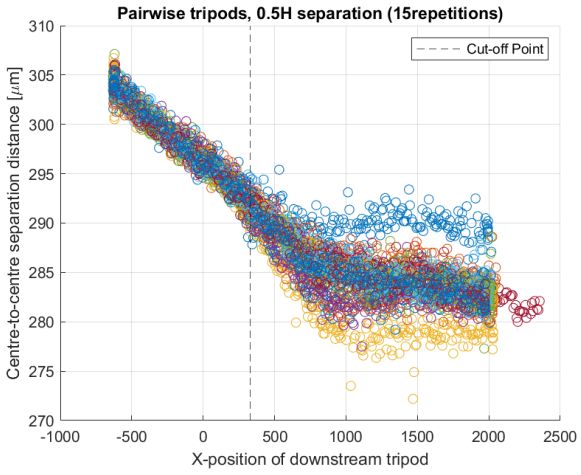

0.5H, Trimer, $\kappa = 2.50$

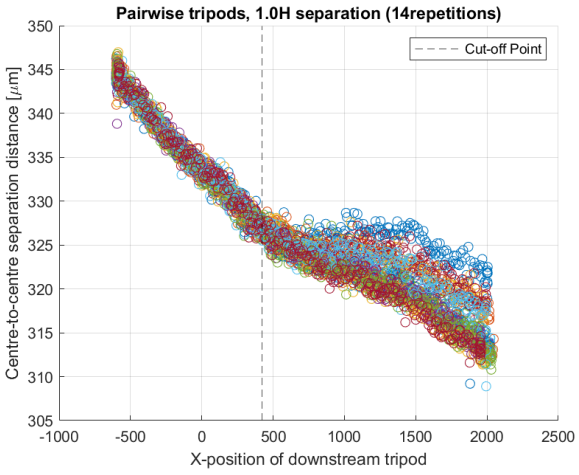

1.0H, Trimer, $\kappa = 2.50$

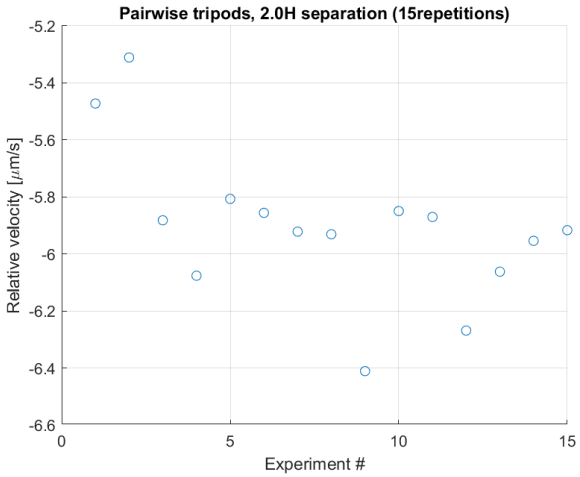

2.0H, Trimer, $\kappa = 2.50$

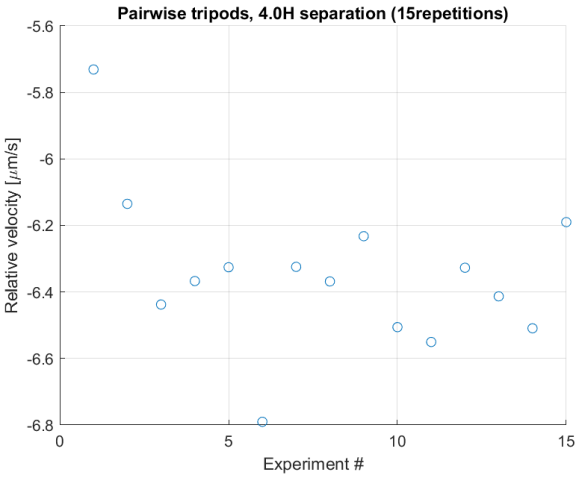

4.0H, Trimer, $\kappa = 2.50$

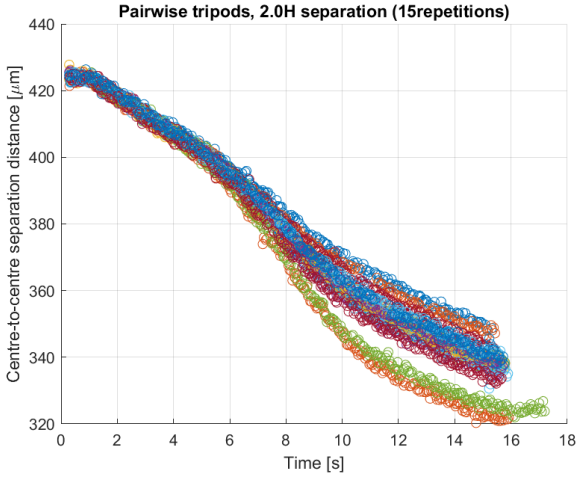

2.0H, Trimer, $\kappa = 2.50$

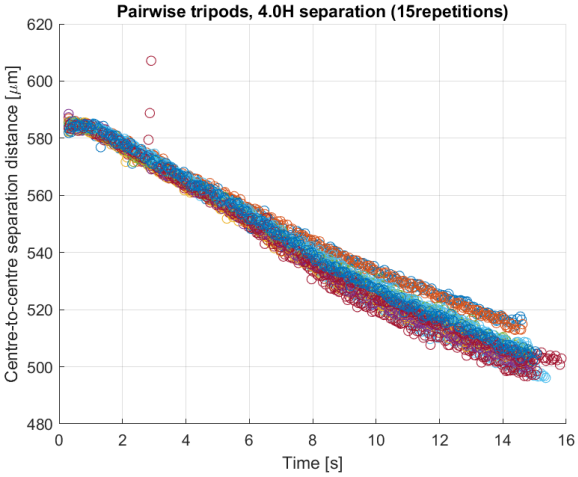

4.0H, Trimer, $\kappa = 2.50$

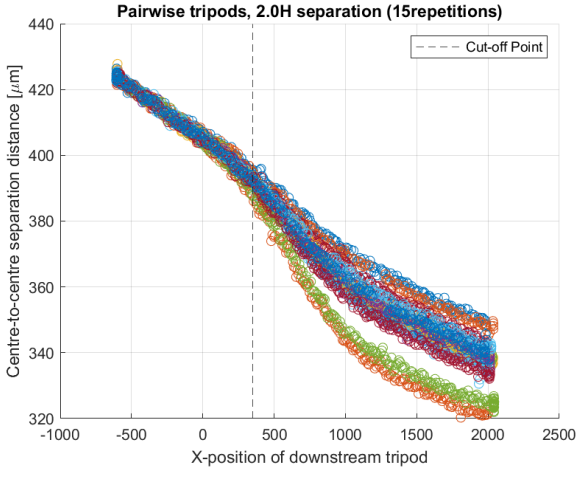

2.0H, Trimer, $\kappa = 2.50$

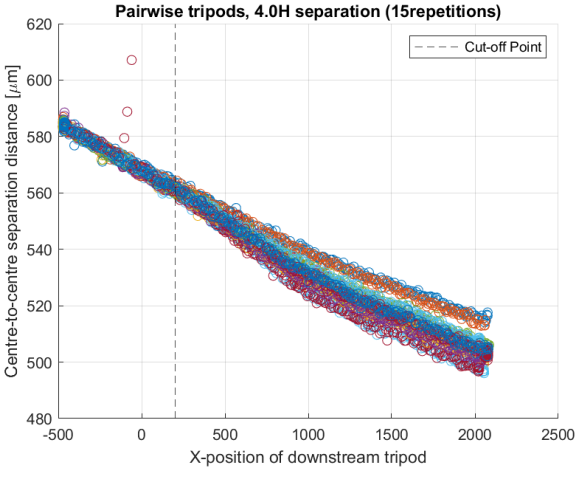

4.0H, Trimer, $\kappa = 2.50$

G

Raw data: tripod angle series

This appendix lists all graphs with raw data for the trimer angle series. Angle of 60° not included, as it is already present in the previous appendix. Graphs start on the next page.

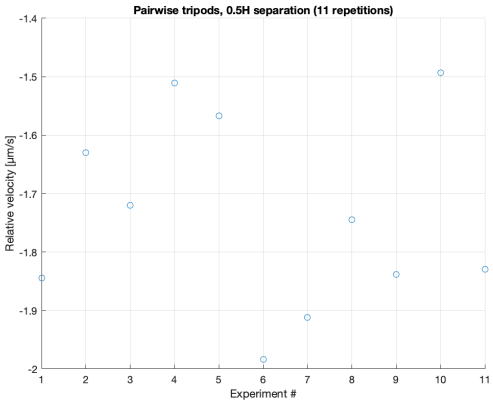

0.5H, Trimer, $\phi = 45°$

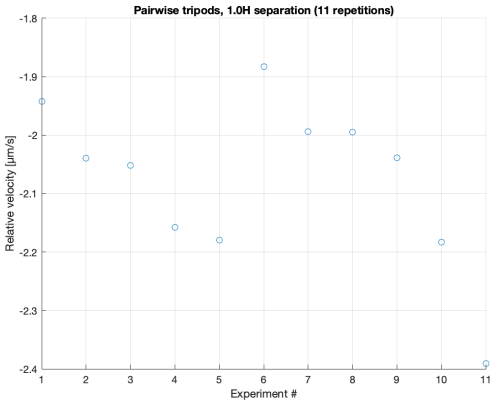

1.0H, Trimer, $\phi = 45°$

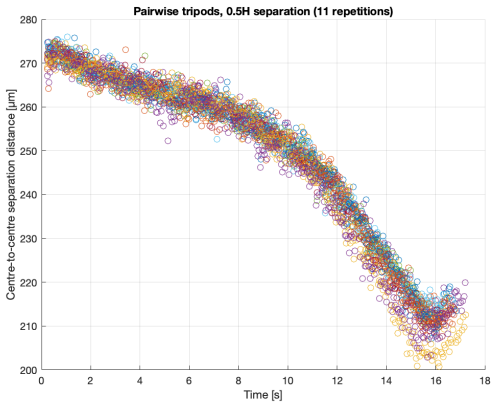

0.5H, Trimer, $\phi = 45°$

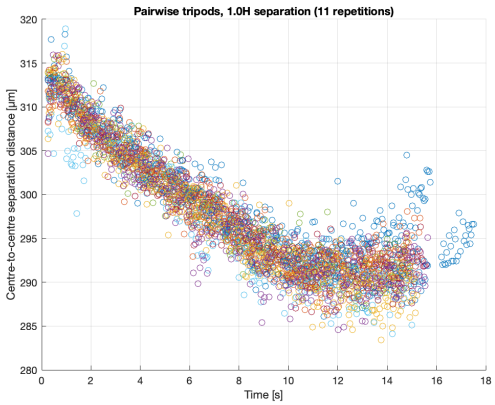

1.0H, Trimer, $\phi = 45°$

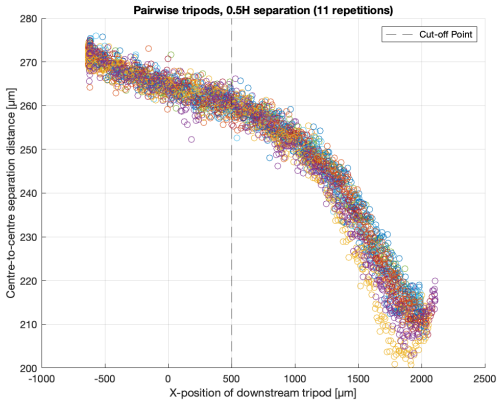

0.5H, Trimer, $\phi = 45°$

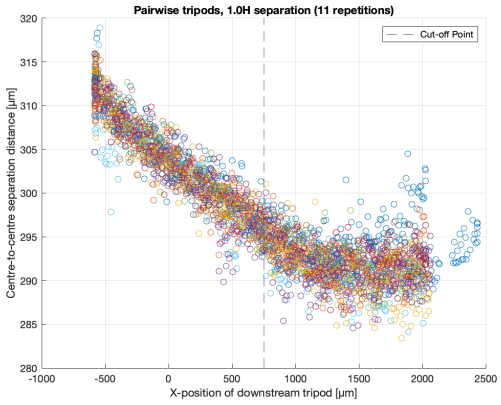

1.0H, Trimer, $\phi = 45°$

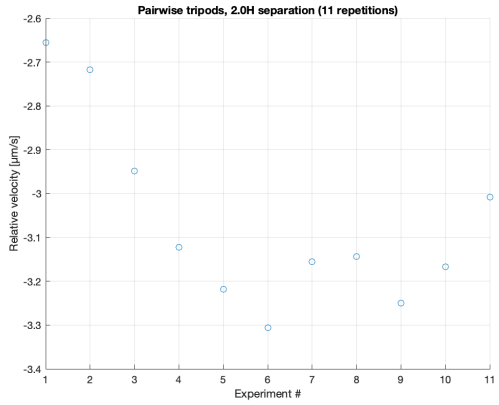

2.0H, Trimer, $\phi = 45°$

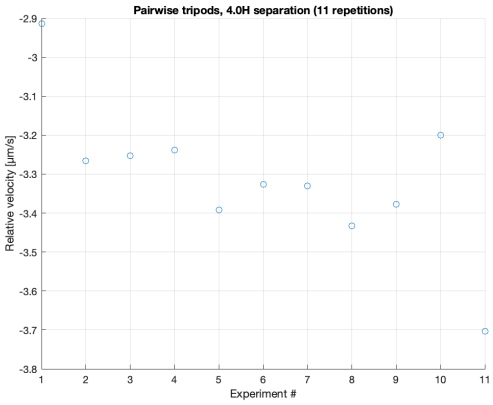

4.0H, Trimer, $\phi = 45°$

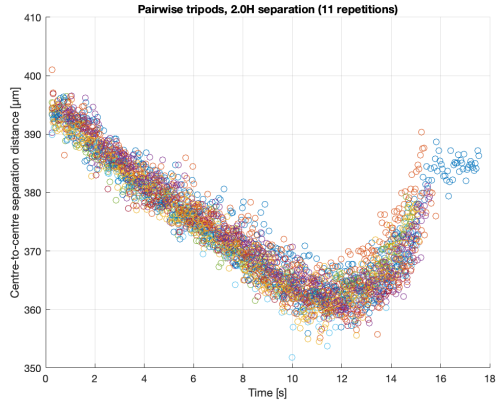

2.0H, Trimer, $\phi = 45°$

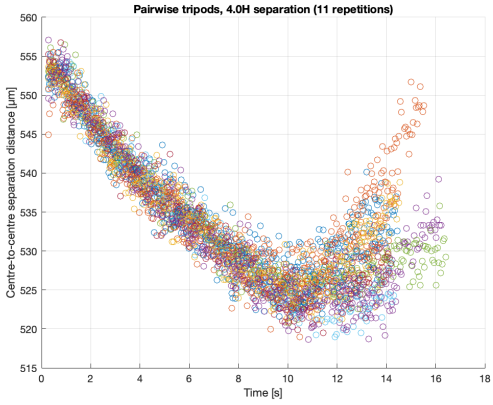

4.0H, Trimer, $\phi = 45°$

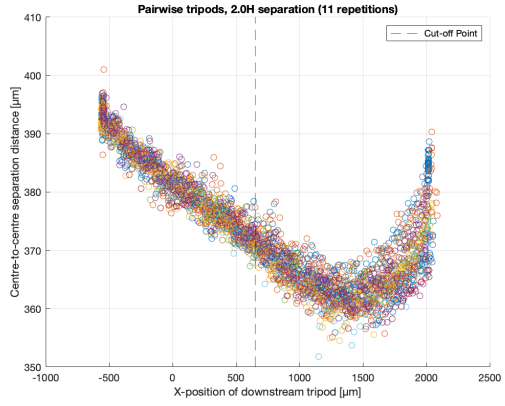

2.0H, Trimer, $\phi = 45°$

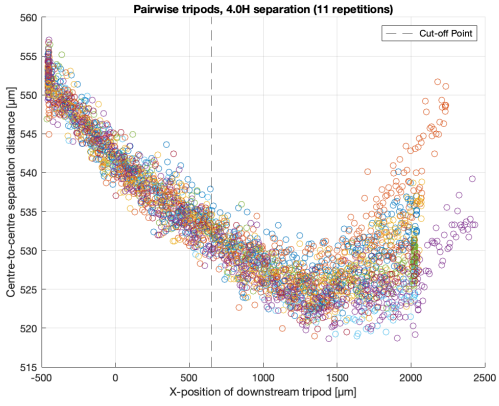

4.0H, Trimer, $\phi = 45°$

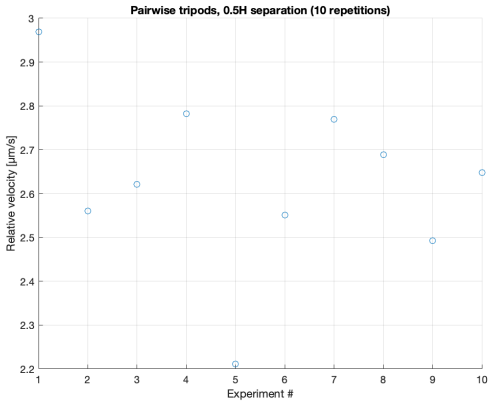

0.5H, Trimer, $\phi = 90°$

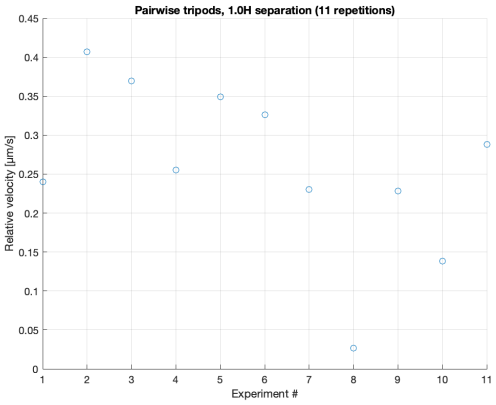

1.0H, Trimer, $\phi = 90°$

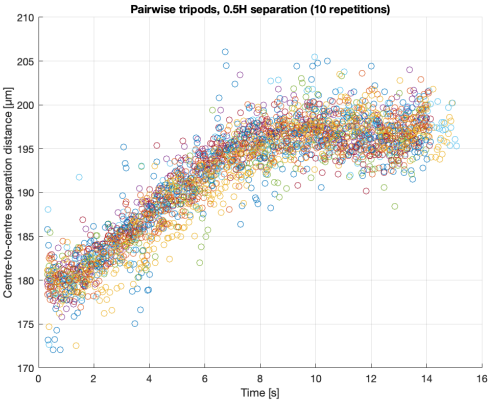

0.5H, Trimer, $\phi = 90°$

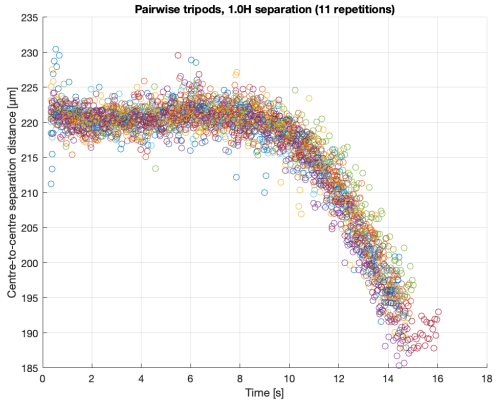

1.0H, Trimer, $\phi = 90°$

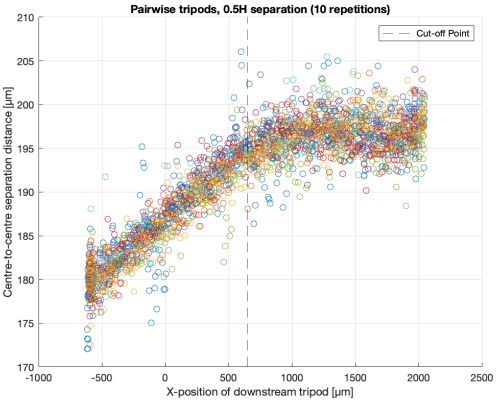

0.5H, Trimer, $\phi = 90°$

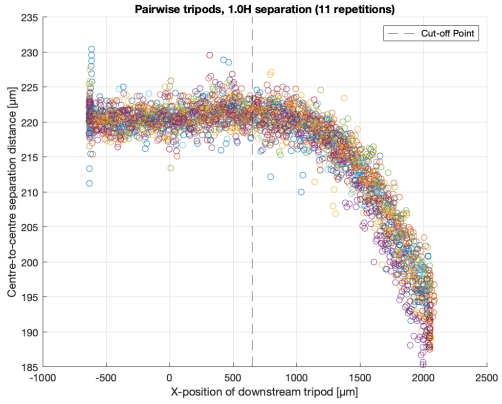

1.0H, Trimer, $\phi = 90°$

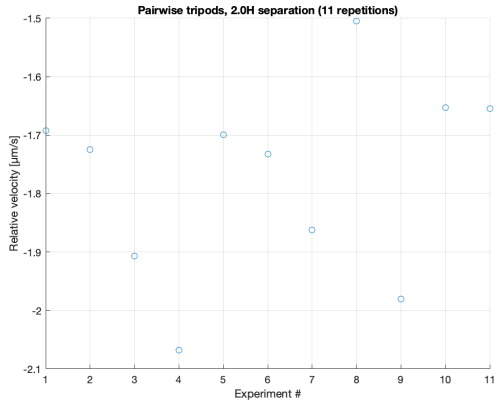

2.0H, Trimer, $\phi = 90°$

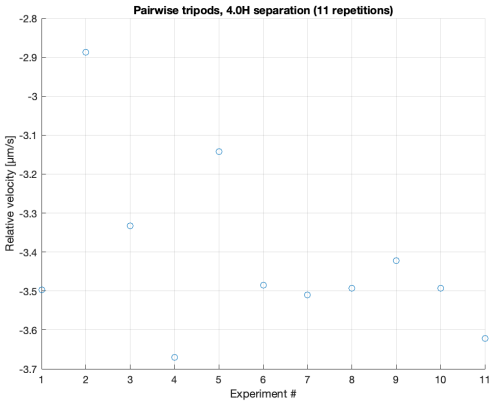

4.0H, Trimer, $\phi = 90°$

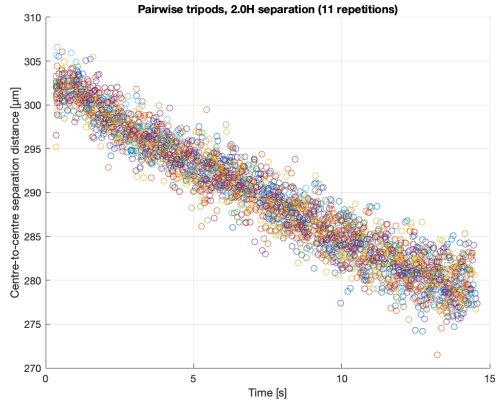

2.0H, Trimer, $\phi = 90°$

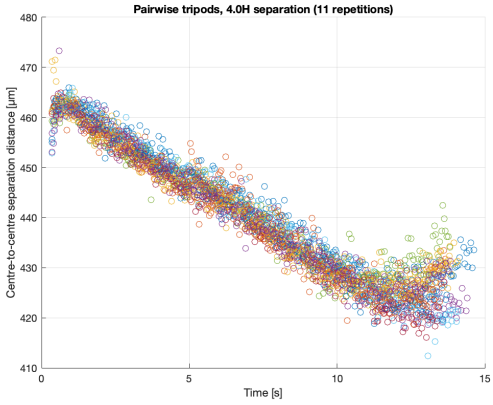

4.0H, Trimer, $\phi = 90°$

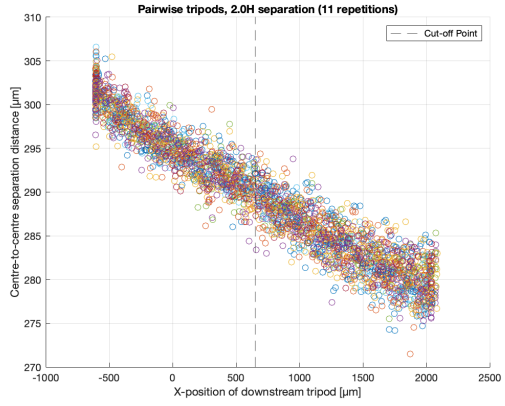

2.0H, Trimer, $\phi = 90°$

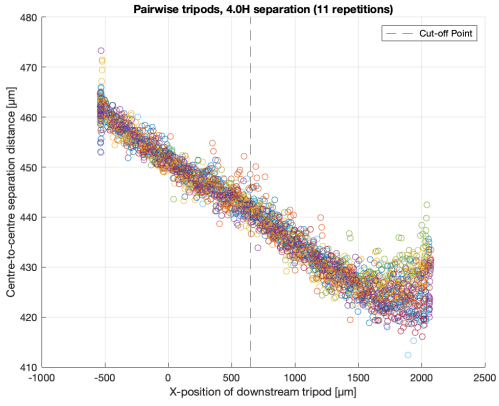

4.0H, Trimer, $\phi = 90°$

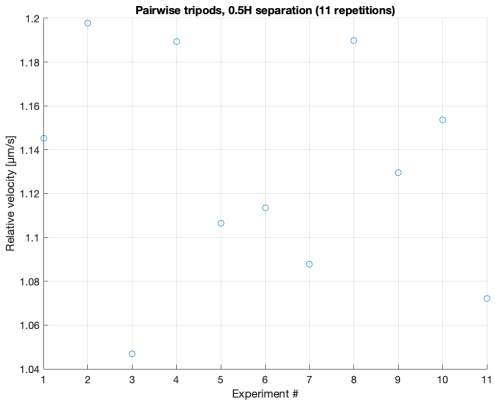

0.5H, Trimer, $\phi = 120°$

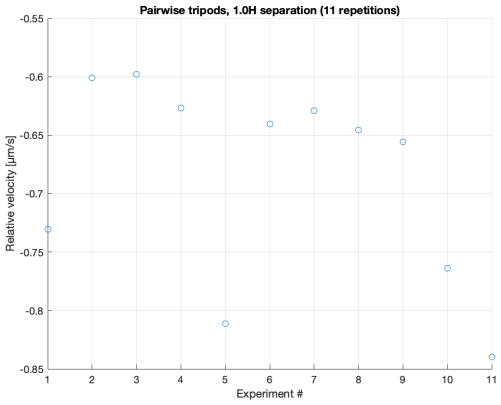

1.0H, Trimer, $\phi = 120°$

0.5H, Trimer, $\phi = 120°$

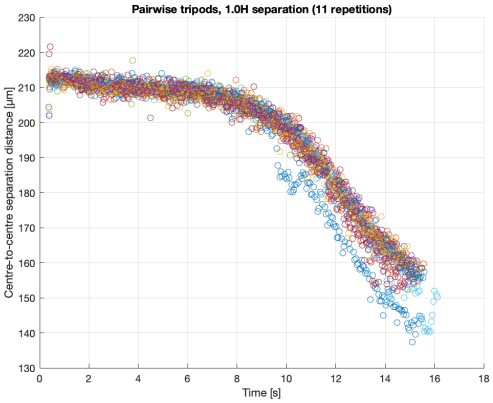

1.0H, Trimer, $\phi = 120°$

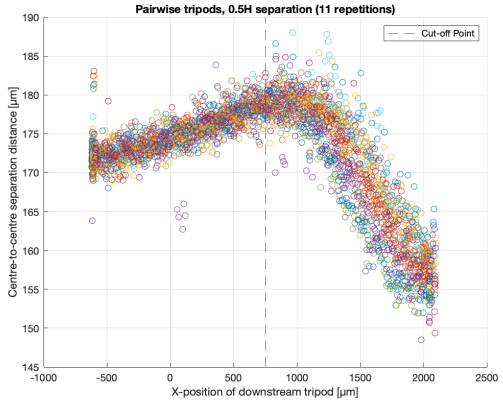

0.5H, Trimer, $\phi = 120°$

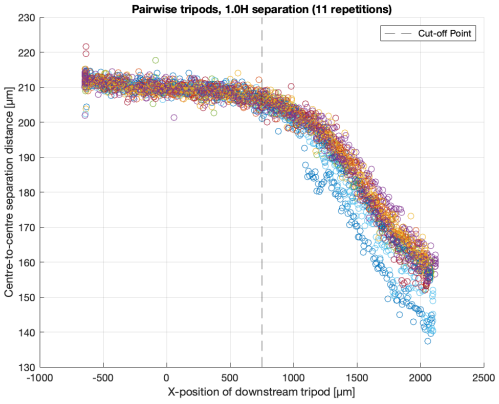

1.0H, Trimer, $\phi = 120°$

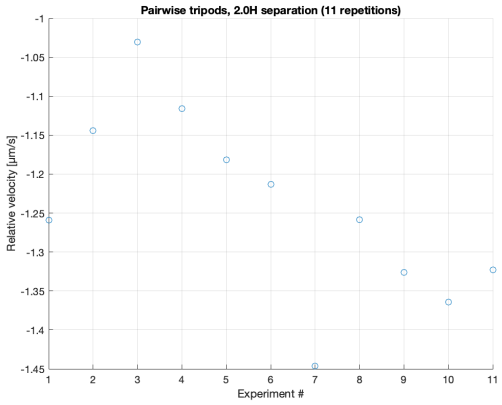

2.0H, Trimer, $\phi = 120°$

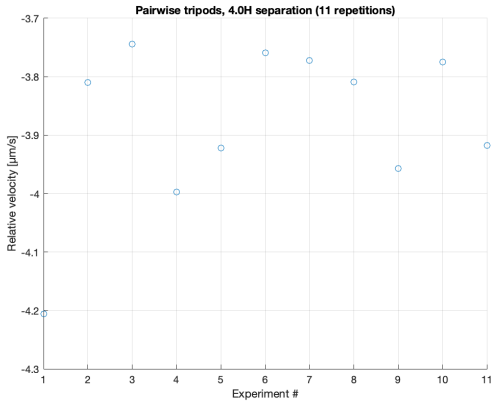

4.0H, Trimer, $\phi = 120°$

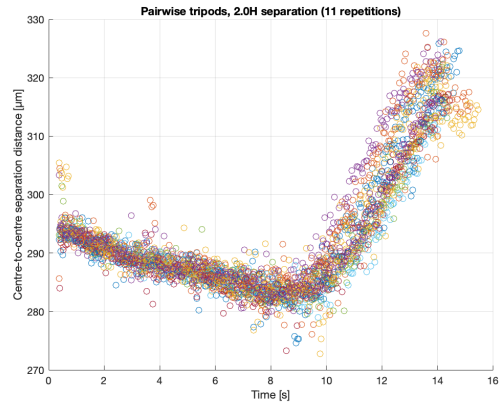

2.0H, Trimer, $\phi = 120°$

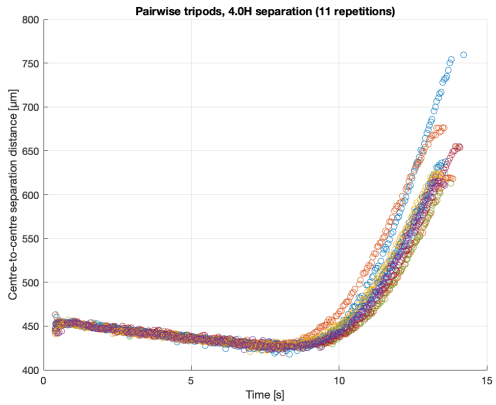

4.0H, Trimer, $\phi = 120°$

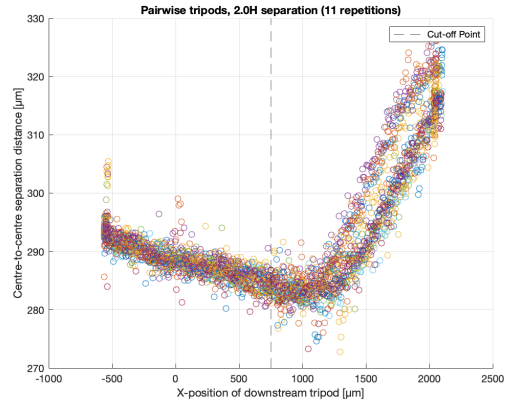

2.0H, Trimer, $\phi = 120°$

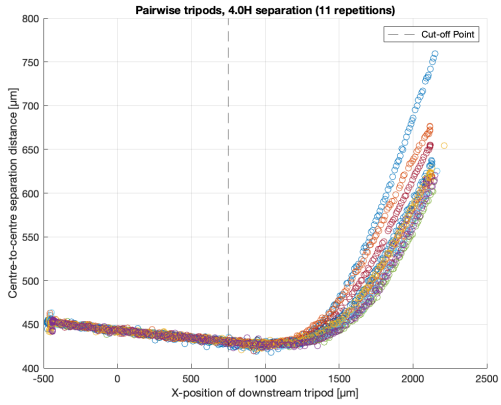

4.0H, Trimer, $\phi = 120°$

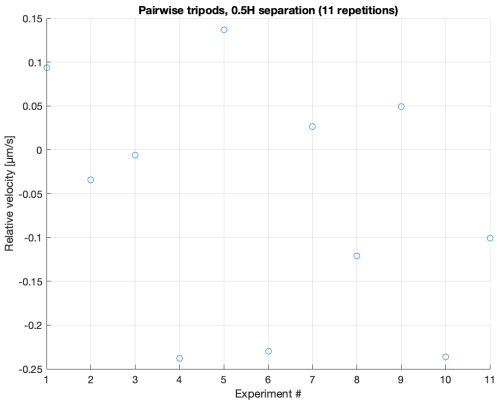

0.5H, Trimer, $\phi = 165°$

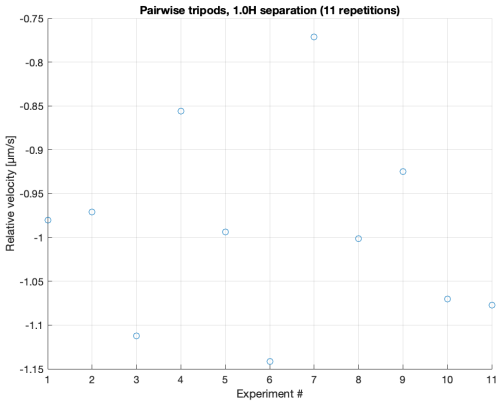

1.0H, Trimer, $\phi = 165°$

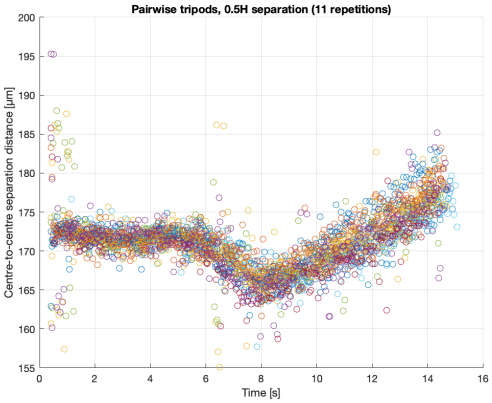

0.5H, Trimer, $\phi = 165°$

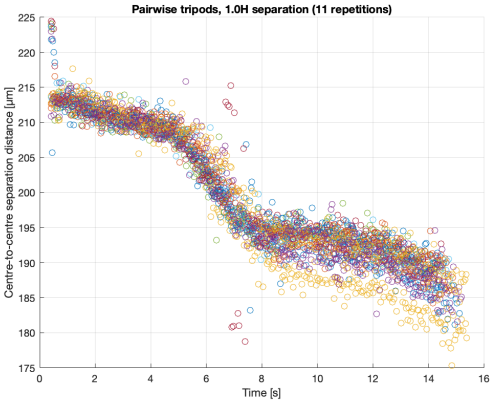

1.0H, Trimer, $\phi = 165°$

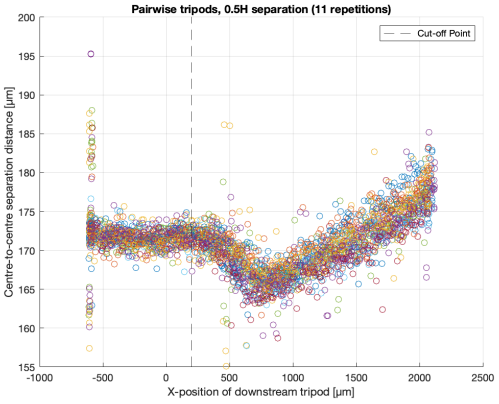

0.5H, Trimer, $\phi = 165°$

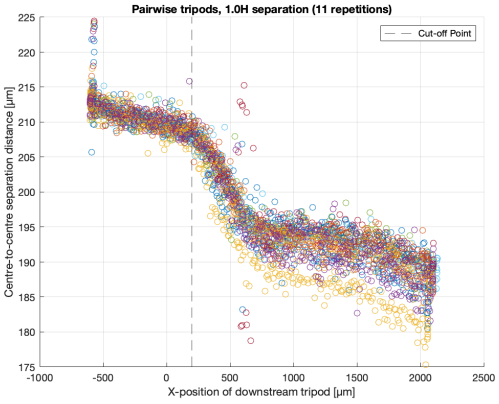

1.0H, Trimer, $\phi = 165°$

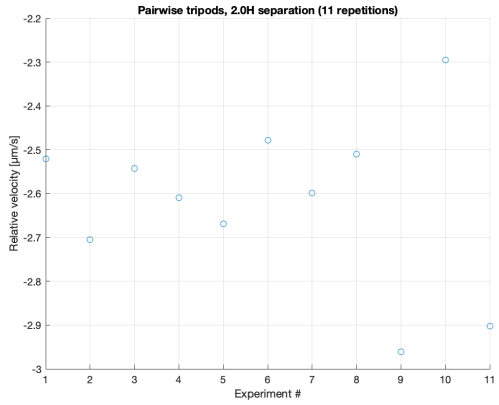

2.0H, Trimer, $\phi = 165°$

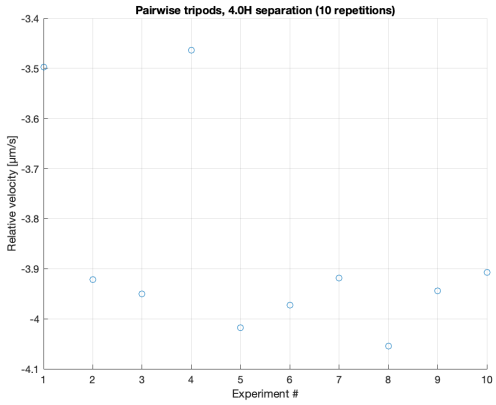

4.0H, Trimer, $\phi = 165°$

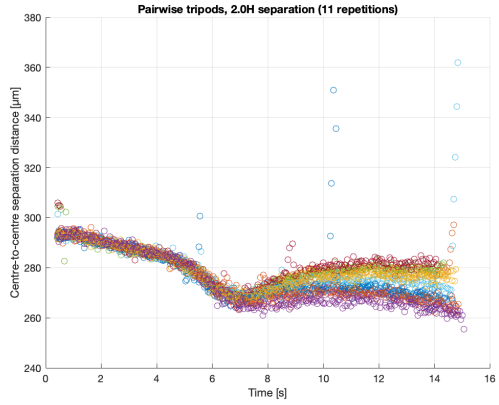

2.0H, Trimer, $\phi = 165°$

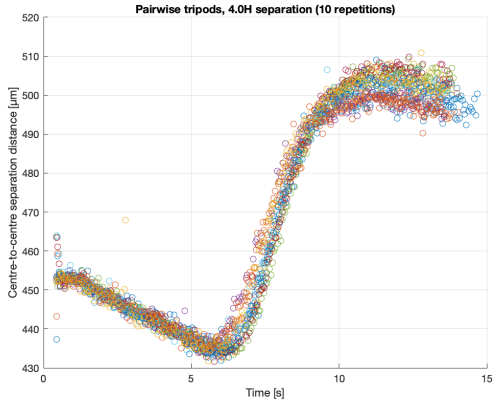

4.0H, Trimer, $\phi = 165°$

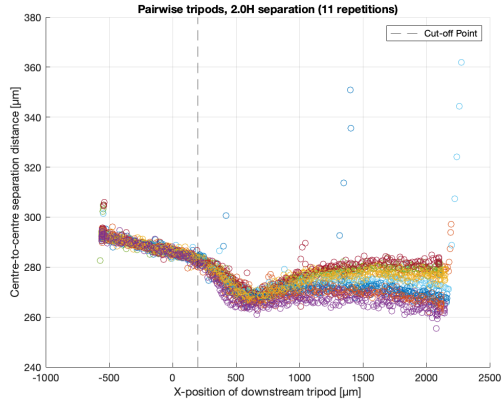

2.0H, Trimer, $\phi = 165°$

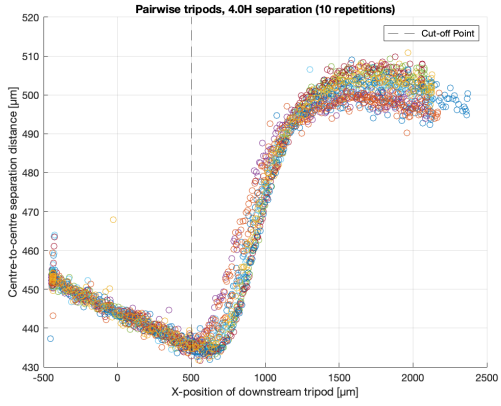

4.0H, Trimer, $\phi = 165°$

Bibliography

[1] R. Attia, D. C. Pregibon, P. S. Doyle, J. L. Viovy, and D. Bartolo. Soft microflow sensors. *Lab on a Chip*, 9:1213–1218, 2009. doi: 10.1039/b813860e.

[2] H. Brenner. The stokes resistance of an arbitrary particle. *Chemical Engineering Science*, 18: 1–25, 1963. doi: 10.1016/0009-2509(63)80001-9.

[3] H. Brenner. The stokes resistance of an arbitrary particle — ii. *Chemical Engineering Science*, 19:599–629, 1964. doi: 10.1016/0009-2509(64)85051-X.

[4] H. C. Brinkman. A calculation of the viscous force exerted by a flowing fluid on a dense swarm of particles. *Applied Science Research*, A1:27–34, 1947. doi: 10.1063/1.868577.

[5] William M. Deen. *Analysis of Transport Phenomena*. Oxford University Press, 198 Madison Avenue, New York, New York 10016, 2 edition, 2013. ISBN 978-0-19-974025-3.

[6] D. Dendukuri, S. S. Gu, D. C. Pregibon, T. A. Hatton, and P. S. Doyle. Stop-flow lithography in a microfluidic device. *Lab on a Chip*, 7:818–828, 2007. doi: 10.1039/b703457a.

[7] D. Dendukuri, P. Panda, R. Haghgooie, J. M. Kim, T. A. Hatton, and P. S. Doyle. Modeling of oxygen-inhibited free radical photopolymerization in a pdms microfluidice device. *Macromolecules*, 41:8547–8556, 2008. doi: 10.1021/ma801219w.

[8] C. Duprat, H. Berthet, J. S. Wexler, O. du Roure, and A. Lindner. Microfluidic in situ mechanical testing of photopolymerized gels. *Lab on a Chip*, 15:244–252, 2015. doi: 10.1039/c4lc01034e.

[9] R. N. Georgiev. Internal report on simulations for pairwise interactions within hele-shaw channels., 2020. This concerns a restricted, internal report that is not available to the public at the time of writing.

[10] R. N. Georgiev, S. O. Toscano, W. E. Uspal, B. Bet, S. Samin, R. van Roij, and H. B. Eral. Universal motion of mirror-symmetric microparticles in confined stokes flow. *Proceedings of the National Academy of Sciences*, 117:21865–21872, 2020. doi: 10.1073/pnas.2005068117.

[11] H. S. Hele-Shaw. The flow of water. *Nature*, 58:34–36, 1898. doi: 10.1038/058034a0.

[12] Polysciences Inc. Polyethylene glycol diacrylate (pegda 400), 2020. URL https://www.polysciences.com/default/catalog-products/peg400da. Accessed on: 23-09-2020.

[13] Merck KGaA. 2-hydroxy-2-methylpropiophenone 972020. URL https://www.sigmaaldrich.com/catalog/product/aldrich/405655. Accessed on: 23-09-2020.

[14] Merck KGaA. Poly(ethylene glycol) diacrylate average mn 250 | peg diacrylate | sigma-aldrich, 2020. URL https://www.sigmaaldrich.com/catalog/product/aldrich/475629. Accessed on: 23-09-2020.

[15] Merck KGaA. Poly(ethylene glycol) diacrylate average mn 575 | peg diacrylate | sigma-aldrich, 2020. URL https://www.sigmaaldrich.com/catalog/product/aldrich/437441. Accessed on: 23-09-2020.

[16] Merck KGaA. Poly(ethylene glycol) diacrylate average mn 700 | peg diacrylate | sigma-aldrich, 2020. URL https://www.sigmaaldrich.com/catalog/product/aldrich/455008. Accessed on: 23-09-2020.

[17] H. Lin and B. D. Freeman. Gas permeation and diffusion in cross-linked poly(ethylene glycol diacrylate). *Macromolecules*, 39:3568–3580, 2006. doi: 10.1021/ma051686o.

[18] J. C. McDonald, D. C. Duffy, J. R. Anderson, D. T. Chiu, H. Wu, O. J. A. Schueller, and G. M. Whitesides. Fabrication of microfluidic systems in poly(dimethylsiloxane). *Electrophoresis: An international journal*, 21:27–40, 2000. doi: 10.1002/(SICI)1522-2683(20000101)21:1<27::AID-ELPS27>3.0.CO;2-C.

[19] Nagaraj Nagalingam. Breaking symmetries. Master's thesis, Delft University of Technology, 2019.

[20] Yeabsira Sahlemariam. Swinging particles: Shape-dependent pair-wise hydrodynamic interactions in confined stokes flow. Master's thesis, Delft University of Technology, 2019.

[21] K. R. Spring and M. W. Davidson. Depth of field and depth of focus, 2020. URL https://www.microscopyu.com/microscopy-basics/depth-of-field-and-depth-of-focus. Accessed on: 07-12-2020.

[22] Sara O. Toscano. Flipping around. Master's thesis, Delft University of Technology, 2018.

[23] W. E. Uspal and P. S. Doyle. Self-organizing microfluidic crystals. *Soft Matter*, 10:5177–5191, 2014. doi: 10.1039/c4sm00664j.

[24] W. E. Uspal, H. B. Eral, and P. S. Doyle. Engineering particle trajectories in microfluidic flows using particle shape. *Nature Communications*, 4:1–9, 2013. doi: 10.1038/ncomms3666.

[25] J. S. Wexler, P. H. Trinh, H. Berthet, N. Quennouz, O. du Roure, H. E. Huppert, A. Lindner, and H. A. Stone. Bending of elastic fibres in viscous flows: the influence of confinement. *Journal of Fluid Mechanics*, 720:517–544, 2013. doi: 10.1017/jfm.2013.49.